Diss. ETH No.21031

Phase transitions and morphologies of mixed organics/ammonium sulfate aerosol particles

A dissertation submitted to
ETH ZURICH

for the degree of
Doctor of Sciences

presented by
MIJUNG SONG
Msc Korea Univ. in Earth and Environmental Sciences
born 03 January 1981
citizen of South Korea

accepted on the recommendation of
Prof. Dr. Thomas Peter, examiner
Dr. Claudia Marcolli, co-examiner
Dr. Thomas Mentel, co-examiner

2013

“Everything should be made as simple as possible but not simpler."
Albert Einstein

Contents

Abstract

Physical state and morphology of aerosol particles are topics in atmospheric research that carry large uncertainties, but attain growing interest because of their potential importance for aerosol radiative properties, gas-to-particle partitioning, and chemistry in and on aerosol particles. The physical state of an aerosol particle depends on its chemical composition, relative humidity (RH) and temperature. In the atmosphere, the inorganic aerosol fraction consists of a relatively small number of constituents while the organic components are a highly complex mixture with a large fraction of species still unidentified. Due to the compositional complexity of the organic fraction, organic aerosols are expected to be present in a liquid state or as amorphous solid state even at dry conditions. Field measurements have shown that the organic and inorganic compounds are internally mixed within single particles. Phase transitions such as liquid-liquid phase separation (LLPS), deliquescence and efflorescence may occur in internally mixed organic/inorganic/H_2O particles when exposed to varying RH in the atmosphere. These phase transitions in mixed aerosol particles may lead to different morphological configurations such as core-shell or partially engulfed structures. However, these properties of aerosol particles are still poorly understood.

Since the physical state and morphology of ambient aerosol particles are difficult to derive from field measurements, laboratory experiments are needed to gain insight into the possible phase transitions and morphologies of internally mixed organic/inorganic/H_2O aerosol particles of atmospheric relevance. Therefore, we have investigated different model systems with ammonium sulfate (AS) as the inorganic component and various organic compounds in order to determine the phases, phase transitions and morphologies for mixtures with different organic-to-inorganic dry mass ratios (OIR) during humidity cycles at 293 K. Micrometer-sized particles consisting of organics/AS/H_2O were deposited on a hydrophobically coated substrate, and the phases and morphologies of the single particles were evaluated using optical microscopy and micro-Raman spectroscopy.

First, we carried out humidity cycles with complex mixtures of dicarboxylic acids containing 5, 6, and 7 carbon atoms (termed C5, C6 and C7) having oxygen-to-carbon atomic ratios (O:C) of 0.80, 0.67, and 0.57, respectively, mixed with AS for various OIR. While the C5/AS/H_2O particles with OIR = 2:1, 1:1 and 1:4 showed no LLPS upon drying to 20 % RH, the C6/AS/H_2O and C7/AS/H_2O particles exhibited LLPS upon drying in RH 50 % - 85 % and ~90 %, respectively. Depending on the OIR, the phase transitions proceeded via spinodal decomposition, growth of a second phase from the particle surface or nucleation-and-growth mechanisms. This suggests that LLPS commonly occurs within the range of O:C < 0.7 in tropospheric organic/inorganic mixed aerosols. Most C6/AS/H_2O and C7/AS/H_2O particles showed a core-shell morphology consisting of an AS-rich core surrounded by an organic-rich phase. Partially engulfed morphology was observed in C6/AS/H_2O droplets with OIR = 1:1 and 1:2, and C7/AS/H_2O droplets with OIR = 2:1.

Second, we investigated how the properties of different functional groups and the compositional complexity of the organic aerosol fraction influence the occurrence of LLPS, exploring the dependence on the organic O:C ratio. Mixtures of up to 10 organic compounds, representing various types of organic functional groups were studied to determine the presence of LLPS in relation to the organic O:C ratios at three different OIR, namely OIR = 2:1, 1:2, and 1:6. A combined evaluation of all experimental results from this study and from the literature showed that LLPS in mixed organic/AS/H_2O aerosols always occurred for O:C < 0.56, never occurred for O:C > 0.80, and depended on the specific types and composition of organic functional groups in the intermediate regime 0.56 < O:C < 0.80. In the intermediate regime, mixtures with a high share of aliphatic compounds shift the limit of occurrence of LLPS to higher O:C ratios and those with a high share of aromatic compounds to lower O:C. The number of mixture components and the spread of the O:C range covered by the organic components did not notably influence the conditions for LLPS to occur. Since in ambient aerosols O:C and OIR range typically between 0.2 and 1.0, and between 4:1 and 1:5, respectively, LLPS is expected to be a common feature of tropospheric aerosols.

Finally, we have elucidated how the deliquescence and efflorescence of AS in mixed organic/AS/H_2O particles is influenced by LLPS and the resulting morphologies of the aerosol particles. Thirty three organic/AS/H_2O systems from this study and literature covering O:C ratios between 0.29 and 1.33 and consisting of different functionalities were investigated. Thirteen out of these 33 systems did not show LLPS for all studied OIR, sixteen showed core-shell morphology when present in a phase-separated state and four showed both core-shell and partially engulfed configurations depending on the OIR and RH. AS in mixed organic/AS/H_2O particles deliquesced between 70 and 84 % RH and effloresced below 58 % RH or remained in a one-liquid-phase state when all mixtures are considered. AS in droplets with LLPS always showed efflorescence with ERH between 30 and 50 % RH. Interestingly, these results clearly show that the presence or absence of LLPS influences AS efflorescence. Moreover, spreading coefficients of the organic-rich phase on the AS-rich phase for PEG-400/AS/H_2O and C6+C7/AS/H_2O and the high resolution elastic Mie resonance spectra of single levitated droplets consisting of PEG-400/AS/H_2O and C6/AS/H_2O proved to be in agreement with the optically observed morphologies of droplets on hydrophobic substrate. Therefore, we expect core-shell morphology as the prevalent configuration of tropospheric organic/AS/H_2O particles consisting of two liquid phases.

Zusammenfassung

Der physikalische Zustand und die Morphologie von Aerosolpartikeln sind offene Fragen der Atmosphärenforschung. Ihnen gilt zunehmendes Interesse aufgrund ihres grossen Einflusses sowohl auf die optischen Eigenschaften der Aerosole, die Gas/Partikel-Partitionierung wie auch auf chemische Prozesse in und auf Aerosolpartikeln. Der physikalische Zustand eines Aerosolpartikels hängt ab von seiner chemischen Zusammensetzung, der relativen Luftfeuchtigkeit (RH) und der Umgebungstemperatur. Die anorganische Fraktion der atmosphärischen Aerosole besteht aus einer relativ kleinen Anzahl Komponenten, wogegen die organischen aus hoch komplexen Mischungen bestehen können, wovon ein grosser Teil noch unbekannt ist. Aufgrund der komplexen Zusammensetzung organischer Aerosole ist zu erwarten, dass sich diese selbst unter trockenen Bedingungen im flüssigen oder einem amorph-festen Zustand befinden. Feldmessungen haben gezeigt, dass organische und anorganische Bestandteile intern gemischt in einzelnen Partikeln vorkommen. Phasenübergänge wie zum Beispiel flüssig/flüssig-Phasentrennung (LLPS), Deliqueszenz und Effloreszenz können in intern gemischten organisch/anorganisch/H_2O Partikeln auftreten, wenn diese in der Atmosphäre unterschiedlichen RH ausgesetzt sind. Diese Phasenübergänge in gemischten Aerosolpartikeln können zu verschiedenen Partikelkonfigurationen wie zum Beispiel einer Kern-Schale-Anordnung oder nur teilweise umhüllten Strukturen führen. Allerdings werden der physikalische Zustand und die Morphologie dieser Aerosolpartikel noch ungenügend verstanden.

Da es schwierig ist, den physikalische Zustand und die Morphologie von natürlichen Aerosolen in der Umgebungsluft aus Feldmessungen zu bestimmen, braucht es Laborexperimente, um Einblick in die möglichen Phasenübergänge und die Morphologie von atmosphärisch relevanten, intern gemischten organisch/anorganisch/H_2O Aerosolpartikeln zu gewinnen. Deshalb untersuchten wir verschiedene Modellsysteme, bestehend aus Ammoniumsulfat (AS) als anorganischem Bestandteil in Kombination mit

mancherlei organischen Verbindungen, um die Phasen, die Phasenübergänge und die Morphologien von Mischungen mit unterschiedlichen organisch-zu-anorganisch Massenverhältnissen (OIR) während Feuchtigkeitszyklen bei 293 K zu bestimmen. Mikrometer kleine organisch/AS/H_2O Partikel wurden auf ein hydrophob beschichtetes Substrat aufgebracht. Die Phasen und Morphologien der einzelnen Partikel wurden mittels optischer Mikroskopie und Mikro-Raman Spektroskopie analysiert.

Als Erstes führten wir Feuchtigkeitszyklen durch mit komplexen Mischungen aus Dicarbonsäuren, welche 5, 6 und 7 Kohlenstoffatome (C5, C6 und C7) enthielten und ein Sauerstoff-zu-Kohlenstoff (O:C) Verhältnis von 0.80, 0.67 und 0.57 aufwiesen, und AS in verschiedenen OIR. Während bei C5/AS/H_2O Partikeln keine LLPS bei OIR von 2:1, 1:1, 1:4 und 20% RH beobachtet wurde, zeigten dagegen 85% der C6/AS/H_2O und ~90% der C7/AS/H_2O Partikel LLPS bei 50% RH, via spinodiale Entmischung, Wachstum einer sekundären Phase von der Partikeloberfläche oder Nukleation-und-Wachstums Mechanismen je nach OIR. Dies lässt den Schluss zu, dass LLPS in troposphärischen, organisch/anorganisch gemischten Aerosolen häufig in solchen mit einem Verhältnis von O:C < 0.7 stattfindet. Die meisten C6/AS/H_2O und C7/AS/H_2O Partikel zeigten eine Kern-Schale Morphologie mit einem AS-reichen Kern, umgeben von einer organisch angereicherten Phase. Nur teilweise eingeschlossene Strukturen wurden bei C6/AS/H_2O Tröpfchen mit OIR = 1:1 oder 1:2 und bei C7/AS/H_2O Tröpfchen mit OIR = 2:1 beobachtet.

Als Zweites untersuchten wir, wie die Eigenschaften von verschiedenen funktionellen Gruppen und die Komplexität der Mischung der organischen Aerosolfraktion das Auftreten von LLPS beeinflussen und analysierten den Zusammenhang zum O:C Verhältnis. Mischungen aus bis zu 10 organischen Komponenten, bestimmte Typen von Modellmischungen repräsentierend, wurden verwendet um das Auftreten von LLPS in Relation zu den organischen O:C Verhältnissen bei drei verschiedenen OIR, nämlich OIR = 2:1, 1:2 und 1:6, zu untersuchen. Eine kombinierte Evaluation aller experimentellen Resultate dieser Studie und aus der Literatur zeigte, dass LLPS in gemischten organisch/AS/H_2O Aerosolen immer für O:C < 0.56

auftrat, nie bei O:C > 0.80 und abhängig von spezifischen Typen und Komposition der organischen funktionellen Gruppen im Zwischenbereich 0.56 < O:C < 0.80. Im Zwischenbereich verschieben Gemische mit einem hohen Anteil aliphatischer Komponenten das Limit, wo LLPS auftritt, in Richtung höherer O:C Verhältnisse, wogegen jene mit einem hohen Anteil aromatischer Komponenten das Limit in Richtung tieferer O:C Verhältnisse verschieben. Die Anzahl Komponenten in einer Mischung und die Verteilung des O:C Verhältnisses der einzelnen organischen Komponenten hatten keinen feststellbaren Einfluss auf die Bedingungen, unter welchen LLPS auftrat. Da für natürliche Aerosole in der Umgebungsluft O:C Verhältnis und OIR Bereich typischerweise zwischen 0.2 und 1.0 beziehungsweise 4:1 und 1:5 liegen, kann erwartet werden, dass LLPS eine gängige Eigenschaft troposphärischer Aerosole ist.

Als Letztes haben wir untersucht, wie LLPS die Deliqueszenz und Effloreszenz von AS in gemischten organisch/AS/H_2O Partikeln beeinflusst und welche Aerosol Partikel Morphologien daraus resultieren. 33 organisch/AS/H_2O Systeme dieser Studie und Literaturwerte im Bereich 0.29 < O:C < 1.33 und unterschiedlicher Funktionalitäten wurden untersucht. 13 aus diesen 33 Systemen zeigten keine LLPS für alle untersuchten OIR, 16 wiesen eine Kern-Schale Morphologie auf, wenn sie sich im zwei-flüssig-Phasen Zustand befanden, und vier zeigten sowohl Kern-Schale als auch partiell umschlossene Konfigurationen, abhängig von OIR und RH. AS in gemischt organisch/AS/H_2O Partikeln deliqueszierte zwischen 70 und 84% RH und effloreszierte bei unter 58% RH oder verblieb in einem ein-flüssig-Phase Zustand, wenn alle Mischungen berücksichtigt wurden. AS in Tropfen mit LLPS zeigte immer Effloreszenz zwischen 30 und 50% RH. Diese Resultate zeigen deutlich, dass ob LLPS stattfindet oder nicht, die Effloreszenz von AS beeinflusst wird. Zusätzlich ist der Ausbreitungsfaktor der organischen Phase über der AS-reichen Phase für PEG-400/AS/H_2O und C6+C7/AS/H_2O und das hochaufgelöste Spektrum der elastischen Mie-Resonanz von einzelnen schwebenden PEG-400/AS/H_2O und C6/AS/H_2O Tropfen in Übereinstimmung mit den optisch beobachteten Morphologien von Tropfen auf einem hydrophoben Substrat. Daher erwarten wir, dass die Kern-Schale Morphologie die häufigste Konfiguration von troposphärischen organisch/AS/H_2O Partikeln ist, welche aus zwei Flüssigphasen bestehen.

Chapter 1

Introduction

1.1 Earth's atmosphere and tropospheric aerosol

Earth's atmosphere is composed of gases and aerosols surrounding the planet and attracted by the gravitational field. The gaseous species contain nitrogen (N_2) (78 %), oxygen (O_2) (21 %), argon (Ar) (0.93 %) and trace gases (each less than 0.1 %) such as carbon dioxide (CO_2), neon (Ne), helium (He), methane (CH_4), krypton (Kr), hydrogen (H_2), nitrous oxide (N_2O), ozone (O_3), etc. in decreasing abundance. Amongst the gaseous species are also variable amounts of water vapor. Although their concentration is less than 1 % in volume mixing ratio, many of these trace gases are greenhouse gases, significantly influencing the Earth climate, or they are active in atmospheric photochemistry, which impacts air quality. An aerosol is defined as a suspension of fine solid or liquid particles in a gas. The aerosols in the atmosphere originate from natural sources such as sea spray or volcanic eruptions, and from anthropogenic sources such as fuel combustion. Primary aerosols are emitted directly into the atmosphere as particles while secondary aerosols are generated via gas-to-particle conversion processes (Seinfeld and Pandis, 2006). In terms of climate, aerosols are the antagonists of the long-lived greenhouse gases, by cooling the planet either directly by scattering sun light back to space, or indirectly via their interactions with clouds.

1.1.1 Size distribution

Tropospheric aerosols contain particles from a few nanometers to tens of micrometers in diameter. The size range of aerosol particles is generally divided into fine (< 2.5 μm) and coarse (> 2.5 μm). Figure 1.1 presents the distinct modes of size distribution of aerosols together with the different

formation mechanisms and removal processes. First, the nucleation mode and the Aitken modes span up to 10 nm and 10 – 100 nm in diameters, respectively. Because of their small size, the aerosols in these two modes are prevalent by number whereas they account only for a small fraction by total mass of atmospheric particles. Particles in the nucleation mode are generated by condensation of "hot vapors" (i.e. condensable gases), and the particles are typically removed by coagulation as they come in contact with larger particles. Second, the accumulation mode consists of particles with diameters between 0.1 and 2.5 μm and comprises a preponderance of surface area and a substantial part of the aerosol mass. The larger size of the particles in the accumulation mode results from their formation processes through the condensation of gases onto preexisting particles and through the coagulation of particles from the Aitken mode. Accumulation mode particles are removed by rainout and washout. Finally, the coarse mode refers to particles in the diameter range of > 2.5 μm, which are mostly generated by mechanical processes. These large particles are efficiently removed from the atmosphere due to their large sedimentation velocity (Seinfeld and Pandis, 2006).

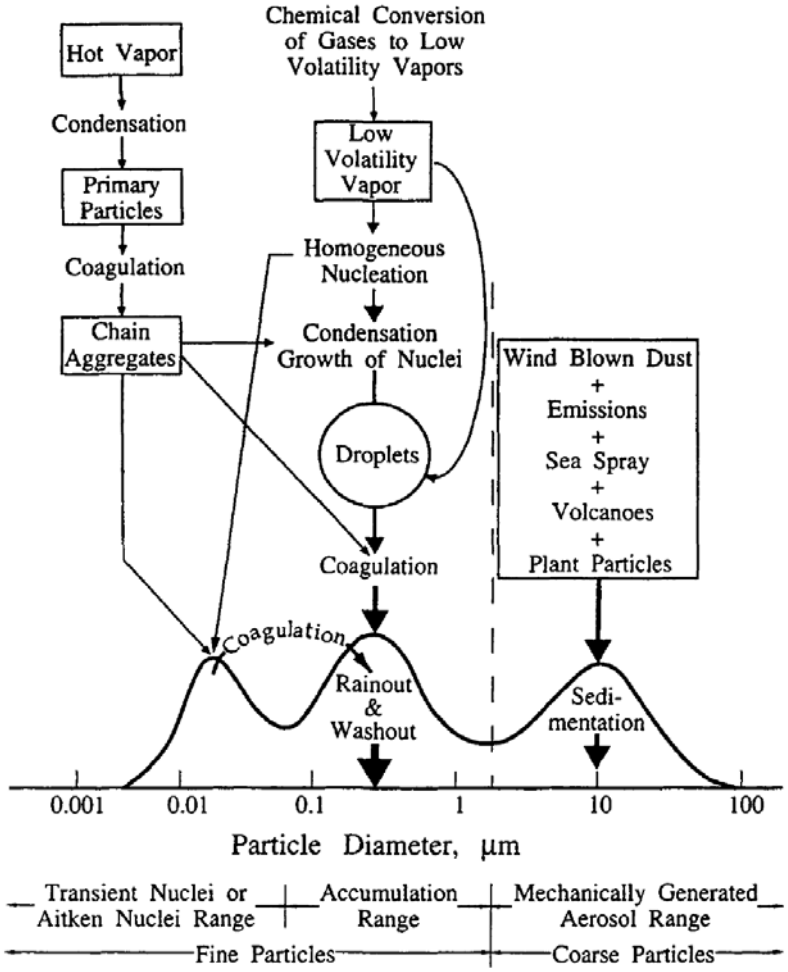

Figure 1.1 *Schematic of principal modes, sources and particle formation and removal mechanisms. The curved line depicts the distribution of particle surface area of a lower tropospheric aerosol. Source: Seinfeld and Pandis (2006).*

1.1.2 Chemical composition

The chemical composition and particle size of tropospheric aerosols depends on their origin and locations. The main chemical components of fine particles have been characterized as sulfate, ammonium, nitrate, organic carbon, and elemental carbon whereas the main chemical components of coarse particles have been identified as crustal elements such as silicon, calcium, magnesium, aluminum, and iron and biogenic organic particles including pollen, and spores (Seinfeld and Pandis, 2006). In general, the fine particles have more soluble constituents and are more hygroscopic than the coarse particles.

Different types of natural (e.g. soil, ocean, volcanic eruption, biological material) and anthropogenic (e.g. fossil fuel combustion) emissions contribute to the chemical composition of aerosol particles. Anthropogenic aerosols are usually in the submicrometer- to micrometer-size range, and they contain numerous organic and inorganic substances such as carbonaceous aerosol, sulfate, and dust or internally mixed with natural particles such as sea salt (Ramanathan et al., 2001). The organic aerosol fraction typically consists of thousands of different compounds and their characterization and quantification are a difficult task. Only 10 - 20 % or even less of the mass of total organic carbon (OC) in aerosols has been identified on the basis of individual compounds (Alves et al., 2002; Decesari et al., 2006; Hallquist et al., 2009). Organic molecules that are emitted directly into the atmosphere condense immediately after emission and contribute to primary organic aerosols (POA). Secondary organic aerosols (SOA) are formed by oxidation and subsequent condensation of gas-phase species (Robinson et al., 2007; Song et al., 2010), and they are typically comprised of molecules consisting of oxygenated organic functional groups including hydroxyl, carboxyl and carbonyl groups (Kawamura and Ikushima, 1993). Highly oxidized organic molecules are more polar and thus are well soluble in water. Monocarboxylic acids, dicarboxylic acids, aldehydes, sugars, and aliphatic alcohols have been identified as the major water-soluble organic compounds that account for 20 - 90 % of total carbon in aerosols (Fuzzi et al., 2001; Alves et al., 2002; Decesari et al., 2006). On the other hand, the water-insoluble fraction contains alkenes, long chain

alkanols, alkanoic acids and polycyclic aromatic hydrocarbons (Rogge et al., 1993).

Depending on the location, organic species represent a major fraction from 20 to 90 % of total fine aerosol mass in the troposphere (Kanakidou et al., 2005; Zhang et al., 2007; Hallquist et al., 2009). Figure 1.2 gives an overview of the fractions of organics (18 - 70 %), sulfate (10 - 67 %), ammonium (6.9 - 19 %) and nitrate (1.2 - 28 %) measured by aerosol mass spectrometry at various locations (Zhang et al., 2007). Oxygenated organic aerosol (OOA) accounts for 95 %, 83 % and 64 % of the total organic aerosols in rural/remote, urban downwind and urban areas, respectively. Moreover, in the Amazon Basin which has been considered as an ideal location to monitor near-natural conditions and intensive biosphere-atmosphere interaction, the submicron particles were dominated by sulfate and organics as measurements with a high-resolution time-of-flight aerosol mass spectrometer during the wet season of 2008 showed. There was significant production of biogenic SOA, whereas primary biological aerosol particles were insignificant in the organic fractions for the submicron Amazonian particles (Chen et al., 2009; Martin et al., 2010; Pöhlker et al., 2012). During the spring time campaign of the Atmospheric Brown Cloud-East Asia Regional Experiment 2005, the mass fractions of organic matter, soluble inorganic ions, EC and unidentified components in PM2.5 (i.e., particles smaller than 2.5 μm) accounted for 39.7 %, 31.3 %, 3.9 % and 25.1 %, respectively at Gosan superstation in Jeju Island, a good location to study the Asian outflows (Lee et al., 2007).

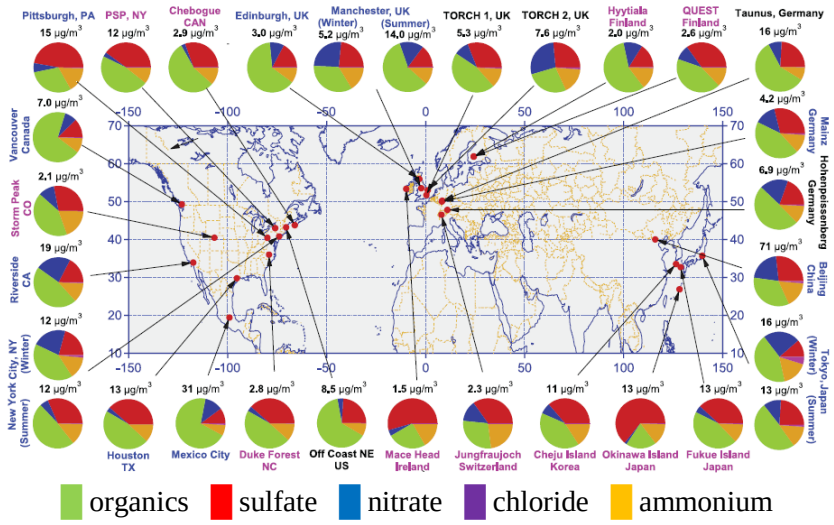

Figure 1.2 *Overview of Aerosol Mass Spectrometer (AMS) datasets of non-refractory PM1 from various regions. Font colors for the location names represent the type of sampling location: urban area (blue), < 100 miles downwind of major cites (black) and rural/remote areas > 100 miles downwind (pink). In the pie chart, colors indicate composition: organics (green), sulfate (red), nitrate (blue), ammonium (orange), and chloride (purple) in PM1. Source: Zhang et al. (2007).*

1.1.3 Direct and indirect aerosol effects

Atmospheric aerosol particles have important environmental effects. They affect the Earth's energy budget directly by scattering and/or absorbing solar and infrared radiation and indirectly by serving as cloud condensation and ice nuclei for cloud droplet activation, which modifies the microphysical and the radiative properties, amount and lifetime of clouds (Yu et al., 2006; IPCC, 2007).

Figure 1.3 shows the net radiative forcing as reported in IPCC AR4 (2007) due to changes in long-lived greenhouse gases, short-lived gases, aerosols, land use and solar irradiance. The radiative forcing due to all greenhouse

gases that absorb outgoing infrared radiation in the atmosphere is positive, and especially CO2 among the gases has the highest forcing. On the other hand, aerosol particles can exert both positive and negative forcing. For example, increases in black carbon contribute to warming while increases in sulfate, organic carbon and mineral dust contribute to cooling because they scatter the incoming radiation. However, the level of scientific understanding is still judged as low to medium, due to uncertainties in the number concentration, size distribution, chemical composition, and physical properties of aerosols in the atmosphere.

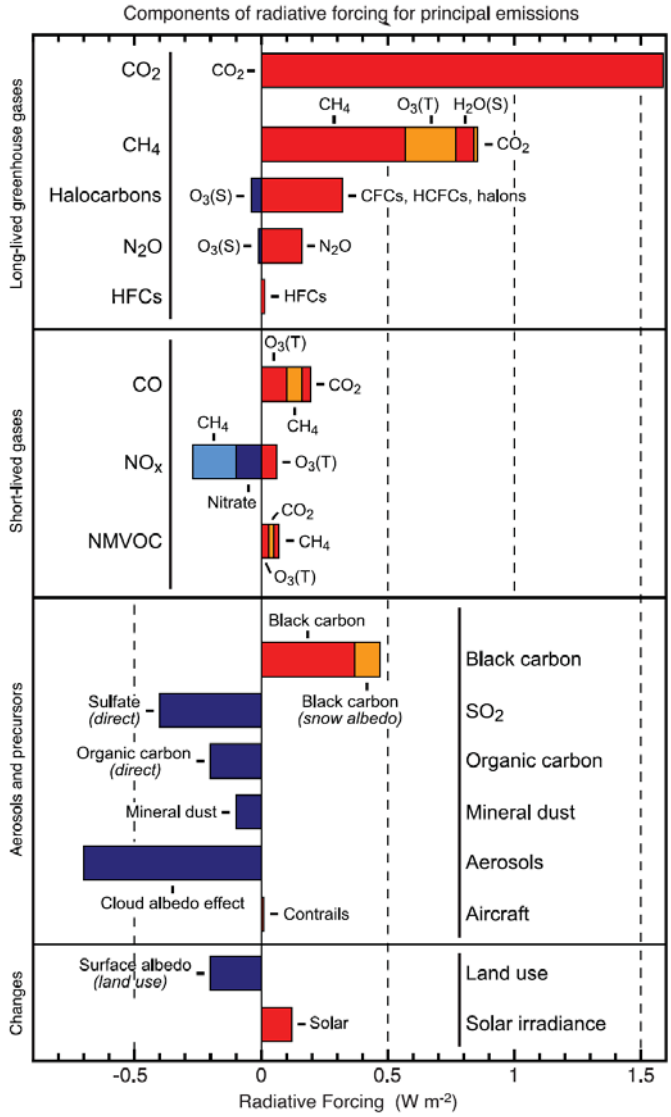

Figure 1.3 *Summary of the radiative forcing from long-lived greenhouse gases, short-lived gases, and aerosols in 2005 due to concentration changes since 1750. (S) and (T) indicate stratospheric and tropospheric changes, respectively. Source: IPCC (2007).*

The indirect effect is determined by the ability of an aerosol particle to act as cloud condensation nucleus, which is a function of the size, chemical composition, mixing state and ambient environment. It is classified into first indirect effect (cloud albedo effect), second indirect effect (cloud lifetime effect) and semi-direct effect (Fig. 1.4). The first indirect effect (cloud albedo effect) is that for fixed liquid water content an increase in aerosols number density may cause an increase in cloud droplet number density and a concomitant decrease in droplet size. As a consequence, a larger number of smaller droplets results in an increase in cloud albedo (negative radiative forcing). The second indirect effect (cloud lifetime effect) is that the reduction in cloud droplet size decreases the precipitation efficiency leading to an increase of the liquid water content, cloud height and cloud lifetime. Hence, a decrease in precipitation and increase of cloud lifetime induces negative radiative forcing. Finally, the semi-direct effect is the mechanism by which aerosol absorption may reduce cloud cover by heating the air and decreasing relative humidity (RH) and thus, it may lead to positive radiative forcing (IPCC, 2007).

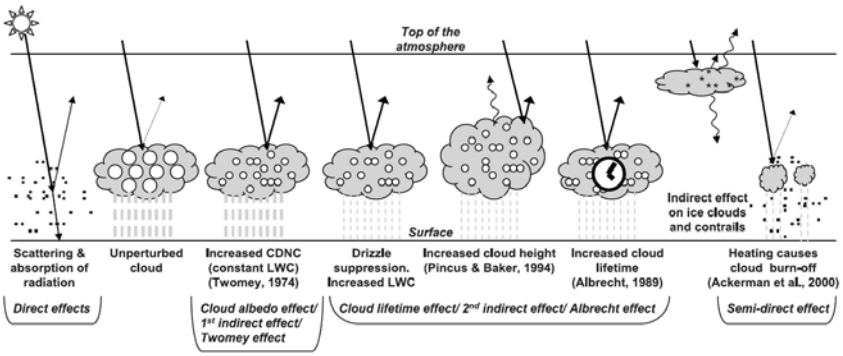

Figure 1.4 *Schematic diagrams of direct and indirect aerosol effects in the atmosphere. Black dots: aerosol particles, open circles: cloud droplets, straight lines: incident and reflected solar radiation, wave lines: terrestrial radiation, gray dashed-lines: rainfall, LWC: liquid water content. Source: IPCC (2007).*

1.2 Aerosol processes

Tropospheric aerosol particles containing organic substances and inorganic salts undergo phase transitions such as deliquescence, efflorescence, and liquid-liquid phase separation (LLPS) as a consequence of changes in ambient RH (Martin, 2000; Marcolli and Krieger, 2006; Martin et al., 2008). Consequently, these phase transitions in the mixed organic/inorganic aerosol particles may lead to different particle configurations (Kwamena et al., 2010; Reid et al., 2011). The chemical composition, the physical state, different phases and the morphologies of the aerosol particles may influence the aerosol direct and indirect effects.

1.2.1 Hygroscopicity

The hygroscopic behavior of inorganic salts such as ammonium sulfate (AS), sodium chloride and ammonium nitrate has been well characterized (Tang and Munkelwitz, 1984, 1994; Cziczo et al., 1997; Martin, 2000). At very low RH, a pure inorganic salt is in a solid state. When a solid salt is exposed to increasing RH, it abruptly absorbs water from the gas phase and becomes a saturated aqueous solution droplet at a specific RH known as deliquescence RH (DRH). Further increase of RH in the subsaturated region leads to the dilution of the solution to maintain thermodynamic equilibrium between the gas and the condensed phase. In turn, when RH is decreased, at RH < DRH the solution droplet may start to supersaturate with respect to solid AS and may reach high degree of supersaturation. Eventually it will abruptly lose its water to the gas phase when it crystallizes at the efflorescence RH (ERH) (see Chapter 2.1). An example of deliquescence, efflorescence and the hysteresis phenomenon is illustrated in Fig. 1.5 (a). During hydration, the pure AS crystal remains in the solid state without mass change up to RH = DRH ~ 80 % when it shows a sudden mass increase due to water absorption. During subsequent dehydration, the AS droplet loses gradually water and crystallizes at RH = ERH ~ 35 %.

While the inorganic salts are relatively small in number and thermodynamically often well characterized, the chemical composition of

the organic matter is highly complex with a large still unidentified fraction (Decesari et al., 2006; Goldstein and Galbally, 2007). Previous studies showed that transition properties of pure organic particles depend significantly on the chemical composition (Braban et al., 2003; Marcolli et al., 2004a; Parsons et al., 2004; Zardini et al., 2008; Yeung et al., 2009). Parsons et al. (2004) measured the DRH of pure dicaroboxylic acid particles such as succinic ($C_4H_6O_4$) and adipic ($C_6H_{10}O_4$) acids to be close to 100 % whereas malonic ($C_3H_4O_4$) and glutaric ($C_5H_8O_4$) acids deliquesce at a much lower RH. In addition, Yeung et al. (2009) measured the ERH of pure glutaric acid at ~30 % and adipic acid at ~95 %. As another example, Fig. 1.5 (e) shows hygroscopicity measurements of pure citric acid ($C_6H_8O_7$) (Zardini et al., 2008). Pure citric acid takes up and releases water gradually without phase transitions. Considering the large multitude of organic components present in the natural and anthropogenic aerosol particles, the organics are expected to be in a liquid state or an amorphous solid state even at low RH in the atmosphere (Marcolli et al., 2004a). Organic and inorganic components have been found to coexist internally mixed in aerosol particles (Lee et al., 2002; Murphy et al., 2006). Depending on the mixing ratios of the components, interactions between organic and inorganic substances within an aerosol particle can influence DRH and ERH of the inorganic salts or even totally suppress crystallization as shown in Fig. 1.5 (b), (c) and (d) (Zardini et al., 2008).

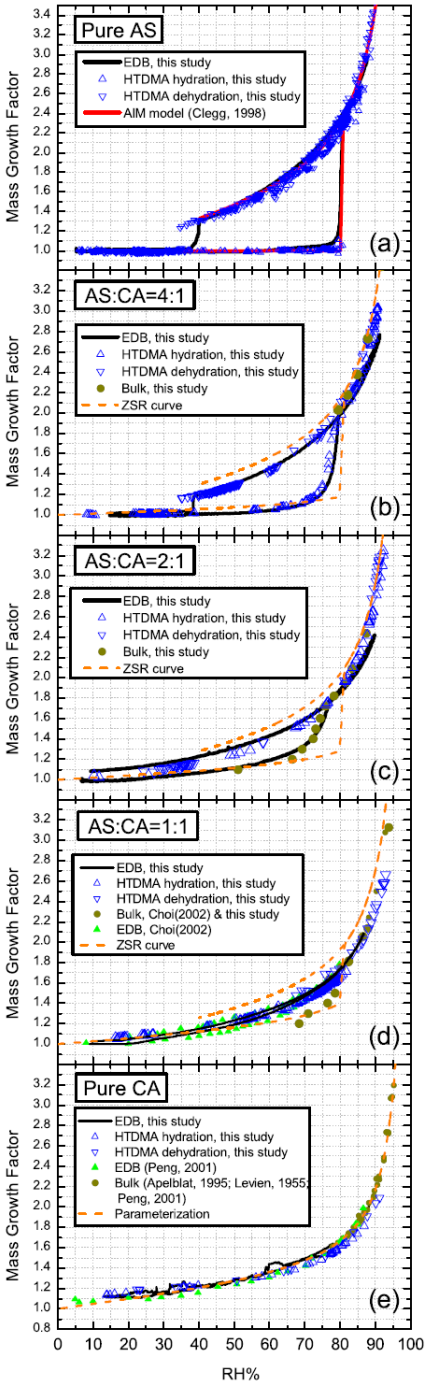

Figure 1.5 *Hygroscopicity cycles of (a) pure ammonium sulfate (AS), (b) mixture of AS and citric acid (CA) for a molar ratio of 4:1, (c) mixture of AS and CA for 2:1, (d) mixture of AS and CA for 1:1, and (e) pure CA particles. Measurements are from particles in an electrodynamic balance (EDB) and from a hygroscopicity tandem differential mobility analyzer (HTDMA). Source: Zardini et al. (2008).*

1.2.2 Liquid-liquid phase separation

The non-ideality of the mixing of dissolved inorganic ions, organic compounds and water may lead to miscibility gaps, which minimize the free energy of the system. A miscibility gap arises from liquid-liquid phase separation (LLPS) into a mainly polar inorganic and a less polar organic-rich phase, which can be understood as a result of salting-out effects: the presence of some salts can reduce the solubility of organic components in water, which are then driven out of the water rich phase (Marcolli and Krieger, 2006; Ciobanu et al., 2009; Zuend et al., 2010; Bertram et al., 2011; Zuend and Seinfeld, 2012). The mechanisms of LLPS are described from a theoretical point of view in Sect. 2.2.

Organic compounds have different affinities to water and the polarity of organic compounds is a key factor in determining the occurrence of LLPS in internally mixed organic/inorganic aerosol particles. The ratio of oxygen to carbon atoms of the organic aerosol fraction, the “O:C ratio”, is, thus, expected to be a good predictor for the presence of LLPS in tropospheric aerosol particles because it reflects the polarity of organic compounds and their miscibility with water and electrolytes. O:C of ambient and laboratory aerosol particles has been derived from analysis of high resolution mass spectral data (Aiken et al., 2007; 2008; Jimenez et al., 2009; Heald et al., 2010; Ng et al., 2011). Heald et al. (2010) reported that the O:C range of total organic aerosols obtained from various field measurements and laboratory studies typically remains below 0.6. The degree of oxidation of chamber organic aerosol strongly depends on the volatile organic precursor molecules. For example, SOA produced by oxidation of α-pinene, isoprene, m-xylene and toluene mostly exhibits O:C < 0.7 while acrolein and glyoxal SOA cover O:C > 0.7 (Chhabra et al., 2011). Biogenic SOA from Holm Oak dominated by monoterpenes (Kiendler-Scharr et al., 2009; Lang-Yona et al, 2010) showed O:C ratios between 0.47 and 0.60 (Lang-Yona et al, 2010). Analysis of ambient organic aerosol measured by aerosol mass spectrometer (AMS) indicated the O:C range of 0.2 - 0.6 during the AMAZE-08 campaign in the Central Amazon Basin (Chen et al., 2009) and 0.4 – 0.8 during the MILAGRO C-130 aircraft campaign over Mexico City (Aiken et al., 2008). Moreover, the O:C of semivolatile oxygenated organic aerosols

(SV-OOA) and low volatility OOAs (LV-OOA) in ambient aerosols showed up to 0.6 and from 0.5 to 1.1, respectively (Ng et al., 2011)..

At the present time, there is no direct measurement technique available that could observe LLPS in ambient aerosols. Recently, ambient aerosols have been collected on a filter and investigated in the laboratory to determine the physical states of ambient aerosol particles. Aerosol samples collected in July and August 2010 in Atlanta, which is highly influenced by both anthropogenic and biogenic emissions showed that LLPS occurred in the particles and is likely to have occurred when the particles were still airborne, provided O:C is roughly $\leq$ 0.5 (You et al., 2012). Moreover, LLPS in Amazonian aerosol samples, which contained a high share of aliphatic carboxylic acids and hydroxyl functional groups in the presence of inorganic microgranular material, was observed in the range of O:C of 0.5 - 0.7 (Pöhlker et al., 2012).

1.2.3 Aerosol morphology

The investigation of aerosol morphology is important for determining the nature of the gas-particle interface, which may affect the rates of heterogeneous chemical reactions and the rate of water uptake (Cai et al., 1996; Fuzzi et al., 2006; Kwamena et al., 2010; Reid et al., 2011). Examining the links between the microphysical state and the morphology of ambient aerosol particles is challenging since there are no in situ measurement tools to monitor the ambient aerosols. Therefore, laboratory experiments are essential to characterize the morphologies of aerosol particles depending on their chemical compositions and physical states.

While inorganic aerosols may be in a crystalline state or dissolved in an aqueous solution, organic aerosols due to the organic compositional complexity are expected stay liquid, or to undergo glass formation under dry conditions, i.e. become amorphous and highly viscous solids (Marcolli et al., 2004a). Figure 1.6 presents the possible morphologies of atmospheric aerosol particles considering the possible phases, the surface and the interfacial forces present in the mixed organic/inorganic particles (see

Krieger et al., 2012; or Chapter 6 of this thesis). Under very dry conditions mixed organic/inorganic particles may first undergo LLPS and then efflorescence, which may lead to a crystalline inorganic phase surrounded by a liquid or amorphous organic phase (image 1) or a crystalline phase containing the liquid phase in pores, veins or cavities (image 2). A third possibility is that the high viscosity of the organic fraction may severely limit water diffusivity, resulting in a homogeneous particle (maybe with some concentration gradients) due a suppression of the crystallization of the inorganic substances (image 3). In contrast, at high RH the conceivable morphologies of a two-liquid-phases state are core-shell and partially engulfed configurations as shown in images 4 and 5, respectively. One liquid phase is presented when organic and inorganic components are miscible (image 6), e.g. under wet conditions.

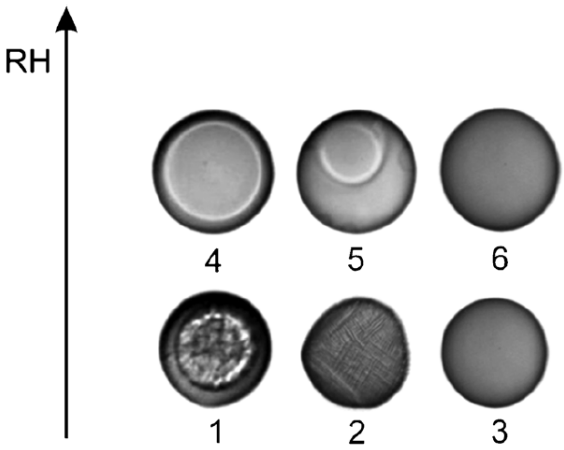

Figure 1.6 *Possible morphologies of atmospheric aerosol particles. Optical microscopic images of micrometer-sized particles sitting on a hydrophobic substrate as a function of relative humidity: 1, crystalline core phase coated by a liquid or amorphous phase; 2, crystalline phase containing liquid phase in pores, veins or cavities; 3, mixed liquid or glassy phase; 4, two liquid phases with core-shell structure; 5, two liquid phases having partially engulfed configuration, and 6, mixed one liquid phase. Source: Krieger et al. (2012).*

1.3 Motivation, objectives and importance of the present research

Physical state and morphology of aerosol particles are an open topic of research that attains growing interest because of its importance for aerosol radiative properties for cloud formation and for multiphase and heterogeneous chemistry in and on aerosol particles. The incomplete knowledge of the aerosol physical state makes it difficult to determine the aerosol morphologies. Moreover, the phase transition behaviors such as LLPS, deliquescence and efflorescence of aerosol particles depend in yet not well-identified way on the chemical composition and on the properties of the organic components. The O:C ratio of aerosol particles may be a key factor to predict the occurrence of LLPS. Recent laboratory studies and calculations have shown that these mixed organic/inorganic aerosols have different morphologies such as core-shell and partially engulfed configurations, which can influence heterogeneous chemistry and gas-to-particle partitioning. To obtain better knowledge of the phase transition behaviors and of the concomitant morphologies of internally mixed aerosol particles during humidity changes, laboratory experiments for investigating the properties of various aerosols are necessary.

The goals of this PhD study are both to establish for which aerosol compositions LLPS occurs and to examine the configurations of liquid-liquid-phase-separated aerosol particles. Such investigations of micrometer sized droplets allow determining liquid-liquid phase boundaries and state diagrams that are not accessible by bulk measurements. The associated objectives are as follows:

To explore the behavior of phase transitions (LLPS and deliquescence/efflorescence) of internally mixed dicarboxylic acids/AS/H_2O particles during humidity cycles (Chapter 4).

To determine how the functional groups and the complexity of the aerosol influence the O:C ratios for which LLPS occurs (Chapter 5).

To characterize droplet morphology and also establish how deliquescence and efflorescence of AS is influenced by LLPS (Chapter 6).

In order to perform the work, laboratory experiments are carried out using optical microscopy and Raman spectroscopy with various aerosol-relevant mixtures, which contain AS and organic substances with different types of functional groups. The findings obtained from these laboratory experiments promote the scientific knowledge on mixed organic/inorganic aerosol particles, which presently belong to the weakest aspects in our understanding of both, climate and air quality. This work differs from the previous studies in that the laboratory measurements have been devised, which cover the full range of conditions and chemical compositions in the real atmosphere, in particular the O:C ratios established from field measurements. Moreover, the aerosol morphologies resulting from LLPS and efflorescence are investigated in this study. Such information is needed to improve the performance of chemistry and climate models, from regional to global scales.

Chapter 2

Phase transitions: theoretical aspects

Phase transitions such as deliquescence, efflorescence and LLPS depend on chemical composition and temperature. In Sect. 2.1 deliquescent and efflorescent behaviors of inorganic salts are discussed. In Sect. 2.2 mechanisms of LLPS such as spinodal decomposition, and nucleation and growth are described.

2.1 Deliquescence and efflorescence

DRH and ERH of electrolyte solutions at 298 K are given in Table 2.1 (Tang and Munkelwitz 1993; Martin 2000). Note that not all inorganic species exhibit deliquescent and efflorescent behaviors. For example, H_2SO_4 has continuous water uptake and release as RH increases and decreases. On the other hand H_2SO_4 but may form number of crystalline hydrates, $H_2SO_4 \cdot nH_2O$.

The deliquescence transition can be explained by the increasing Gibbs free energy of an aqueous solution and the constant Gibbs free energy of a solid with increasing RH. At low RH, the Gibbs free energy of the solid salt is lower than the energy of the corresponding aqueous droplet, and hence the salt remains in solid state (Fig. 2.1). As RH increases, the energy of the aqueous solution decreases, and eventually it equals the energy of the solid at DRH producing a saturated solution. Such a deliquescence transition is accompanied by a sudden increase in the mass of the particle when it takes up water. At RH above DRH, an aqueous solution is the thermodynamically stable state. Upon drying, the energy of the solid and liquid states is once more equal at DRH. However, the aqueous droplet does not crystallize at DRH upon drying but may remain in a metastable liquid state becoming a supersaturated solution. Since an energy barrier has to be overcome to form critical nuclei (crystallization), ERH is lower than DRH. Such a hysteresis

phenomenon is a characteristic of most salts (Seinfeld and Pandis, 2006). Some electrolytes like $NaNO_3$, NH_4NO_3 and NH_4HSO_4 do not readily crystallize even down to 0 %RH (Table 2.1). While DRH can be calculated by thermodynamic models, ERH depends on the nucleation barrier height and typically has to be determined experimentally.
From the water activity (a_w) of the saturated solution (Eq. 2.1), DRH can be obtained.

$$a_w = \frac{p_{sw}}{p_w} = \frac{\mathrm{DRH}}{100} \tag{2.1}$$

where
p_{sw}: water vapor pressure of the saturated aqueous solution
p_w: vapor pressure of pure water at the same temperature

Table 2.1 *Deliquescence relative humidity (DRH) and mean efflorescence relative humidity (ERH) at 298 K of atmospherically relevant salts. "Not observed" means that no crystallization occurs in the particle down to 0 %RH. Compiled from Tang and Munkelwitz (1993) and Martin (2000).*

Electrolytes	DRH (%)	ERH (%)
KCl	84.2	59
Na_2SO_4	84.2	56
NH_4Cl	80.0	45
$(NH_4)_2SO_4$	80.0	35
NaCl	75.3	43
$NaNO_3$	74.3	Not observed
NH_4NO_3	61.8	Not observed
NH_4HSO_4	40.0	Not observed

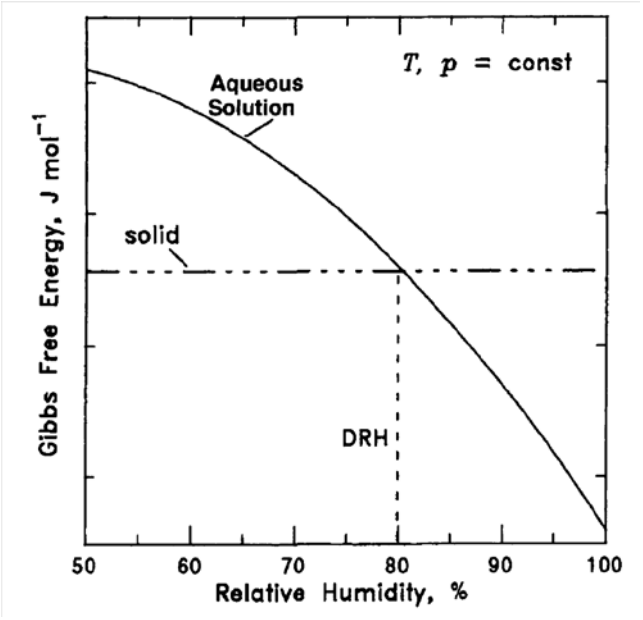

Figure 2.1 *Gibbs free energy as a function of relative humidity of a solid salt and its aqueous solution at constant temperature and pressure. The Gibbs free energy of the solid salt equals the energy of the aqueous solution at the deliquescence relative humidity (DRH). Source: Seinfeld and Pandis (2006).*

The DRH for an inorganic salt depends on temperature. The vapor-liquid equilibrium of a salt S can be expressed by the following reactions. Here, the energy released in the reaction (R2.1) is the heat of condensation of water vapor, and the heat absorbed in the reaction (R2.2) is the enthalpy of solution of the salt:

$$H_2O(g) \leftrightarrow H_2O(aq) \quad \text{(R2.1)}$$
$$H_2O(aq) + nS(s) \leftrightarrow nS(aq) \quad \text{(R2.2)}$$

Therefore, the overall enthalpy change ΔH for the reaction is

$$\Delta H = n\Delta H_s - \Delta H_v \tag{2.2}$$

where

S: a salt
n: solubility of S in water in moles of solute per mole of water
ΔH: enthalpy change
ΔH_s: enthalpy of solution of S
ΔH_v: enthalpy of vaporization

The change of water vapor pressure with temperature is given by the Clausius-Clapeyron equation (e.g. Seinfeld and Pandis, 2006):

$$\frac{d \ln p_{sw}}{dT} = -\frac{\Delta H}{RT^2} \tag{2.3}$$

where
T: temperature in Kelvin
R: universal gas constant

Applying the Clausius-Clapeyron equation (Eq. 2.3) to pure water at a specific temperature T and considering the enthalpy change ΔH, of a single solute system, we obtain

$$\frac{d \ln p_{sw}}{dT} = \frac{\Delta H_v}{RT^2} - \frac{n\Delta H_s}{RT^2} \tag{2.4}$$

Combining Eq. 2.4 with the Clausius-Clapeyron equation for pure water,

$$\frac{d \ln (p_{sw}/p_w)}{dT} = -\frac{n\Delta H_s}{RT^2} \tag{2.5}$$

and substituting the definition of DRH (Eq. 2.1) into Eq. 2.5 we obtain

$$\frac{d \ln (\mathrm{DRH})}{dT} = -n\frac{\Delta H_s}{RT^2} \tag{2.6}$$

The solubility *n* can be approximated by a polynomial in *T*, and Eq. 2.6 can then be integrated from T_0 = 298 K to *T*:

$$ln\frac{DRH(T)}{DRH(T_0)} = \frac{\Delta H_s}{R}\left[A\left(\frac{1}{T} - \frac{1}{T_0}\right) - Bln\frac{T}{T_0} - C(T - T_0)\right] \qquad (2.7)$$

Finally, we obtain DRH as a function of temperature (*T*) given in Eq. 2.8 (Seinfeld and Pandis, 2006):

$$\mathrm{DRH}(T) = \mathrm{DRH}(298\mathrm{K})\exp\left\{\frac{\Delta H_s}{R}\left[A\left(\frac{1}{T} - \frac{1}{298\mathrm{K}}\right) - B\ln\frac{T}{298\mathrm{K}} - C(T - 298\mathrm{K})\right]\right\} \qquad (2.8)$$

2.2 Mechanisms of liquid-liquid phase separation

Different mechanisms such as “spinodal decomposition” and “nucleation and growth” can lead to LLPS. These mechanisms can be distinguished by the time evolution of fluctuations in a mixed system.

2.2.1 Spinodal decomposition

A one-liquid-phase system can separate into a two-liquid-phases system via spinodal decomposition with rapid growth of ubiquitously dispersed clusters and subsequent cluster aggregation (coalescence). This occurs when the system reaches the unstable region below the spinodal curve (Fig. 2.2, dashed line). Just below the spinodal curve, concentration fluctuations of arbitrarily small amplitude develop continuously in time until equilibrium compositions are attained (Fig. 2.3 (b)). Small patches develop in the earliest stage during the spinodal decomposition process, which are highly interconnected and coalesce into small separated regions. These regions contain separated phases with different index of refraction and, thus, can cause “Schlieren”, which can be diagnosed by Schlieren photography or – as in this work – by microscopy. Since spinodal decomposition occurs without

energy barrier, LLPS via spinodal decomposition appears in the whole solution volume as a concerted process (Shelby, 1995; Papon et al., 1999).

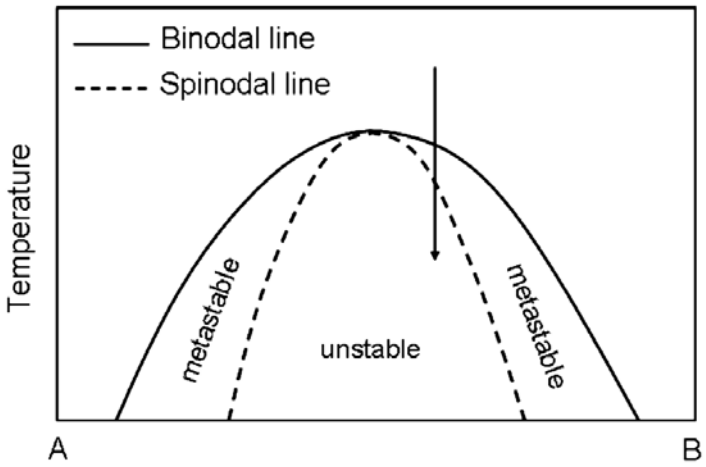

Figure 2.2 *Phase diagram of two partially miscible components (A and B). The solid line and dashed line represent boundaries of binodal and spinodal regions, respectively. Source: Papon et al. (1999).*

2.2.2 Nucleation and growth

Alternatively, LLPS may occur by nucleation and growth, when a system has reached the metastable region (Fig. 2.2). Nucleation and growth may occur, when a transition energy barrier exists, which makes a spinodal transition impossible. However, when concentration fluctuations reach a critical amplitude and size, a critical nucleus can form and overcome this nucleation barrier. From a classical point of view, the critical nucleus is just large enough, so that the energy gain from converting the volume of the critical nucleus from the thermodynamically metastable into the stable phase suffices to balance the energy required for the interface between both phases. For the nucleation and growth mechanism, the concentration of the second

phase reaches the critical amplitude (C_2), and then it grows in time by diffusion as shown by α_2 of Fig. 2.3 (a). Nuclei of the second phase appear randomly in the volume of the sample. Spherical shapes minimize the surface for a fixed volume when both phases are liquids. Therefore it is expected that these regions exist as spherical inclusions that may coalesce with each other when they come in contact by diffusion. Compared to the spinodal decomposition, the nucleation and growth mechanism differs by slower evolution in time. Nucleation and growth is prevalent, when the system separates into a major (larger volume) and a minor phase. This is also evident from Fig. 2.2, where the spinodal curve touches the phase separating curve, i.e. the binodal, when concentrations of both components are comparable, whereas nucleation and growth is required for differing initial concentrations (vertical downward arrow). The different initial concentration (C_B) of the mixed system for nucleation and growth and spinodal decomposition mechanism is illustrated in Fig. 2.3 (a) and (b), respectively (Papon et al., 1999).

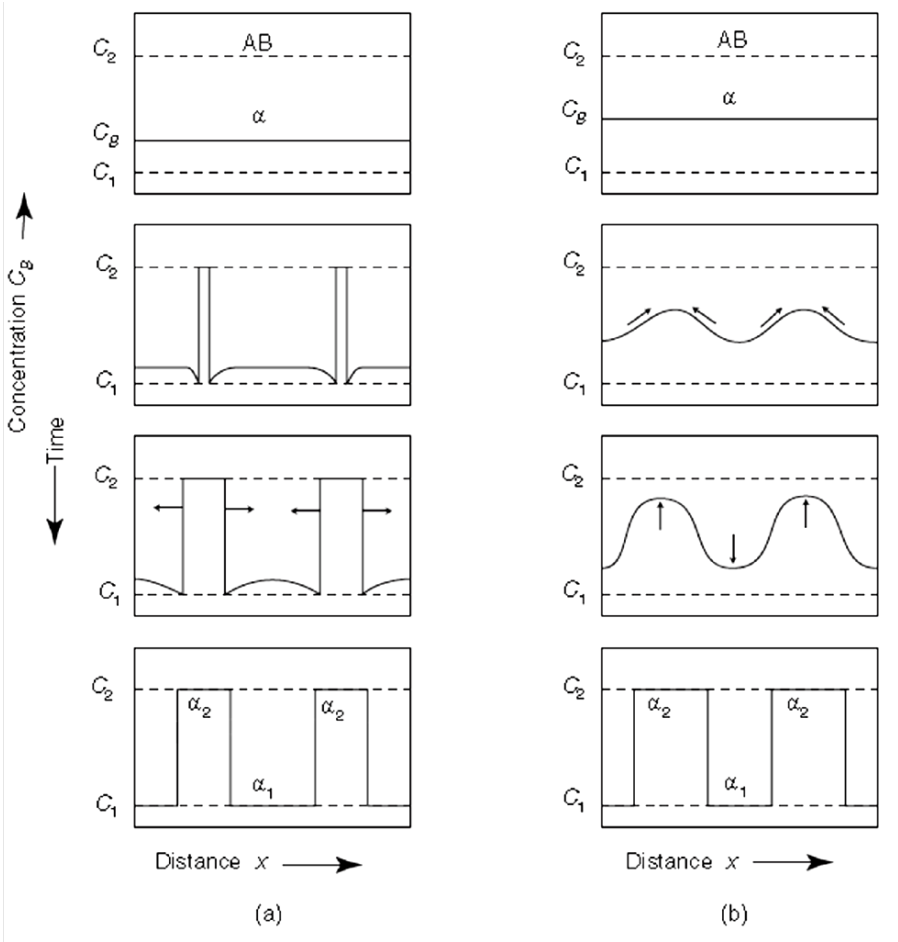

Figure 2.3 *Different phase separation mechanisms (a) nucleation and growth, and (b) spinodal decomposition for a binary mixture AB. Two phases α_1 and α_2 form from the initial mixed phase α of composition C_B. The final concentrations of α_1 and α_2 phases are C_1 and C_2, respectively. Source: Papon et al. (1999).*

Chapter 3

Experimental

In this laboratory study, phase transitions and morphological changes of mixed organic/AS/H2O particles are investigated during humidity cycles at 293 K using optical microscopy and Raman spectroscopy. As organic model components, atmospheric relevant organic species covering wide ranges of O:C and different functional groups have been chosen (Decesari et al., 2006; Gilardoni et al., 2009; Hawkins et al., 2010), and AS is used as an inorganic model substance because it is a main inorganic component of the troposphere and has well-characterized thermodynamic and spectroscopic properties (Braban and Abbatt, 2004; Ling and Chan, 2008; Yeung et al., 2009). Various solutions of organic components mixed with AS in purified water (resistivity $\geq$ 18.0 MΩ cm) were prepared for different organic-to-inorganic mixing ratios (OIR).

3.1 Hydrophobic coating procedure

Aqueous droplets were deposited on a hydrophobically coated glass slide to avoid the spreading of the aqueous solutions and heterogeneous nucleation owing to surface contact. In order to coat the substrate a silanization procedure is used that leads to the coverage of a surface through self-assembly via a gas-phase reaction. First, the glass slide is purified by immersing in a Piranha solution consisting of a mixture of H_2SO_4:H_2O_2 = 2:1 for about twelve hours. Second, the glass slide is cleaned in purified water, and then it is dried by pure N_2 gas. Third, the glass slide and few drops of a silanization solution (Sigma-Aldrich) containing 5 % dimethyldichlorosilane in heptane are kept together in a closed container for two days. Lastly, the hydrophobically coated glass slide is flushed with pure water and dried by pure N_2 gas.

3.2 Principle of droplet generator

The micrometer-sized aqueous droplets are generated using a droplet generator modified ink-jet cartridge (Hewlett Packard, Model HP 51604) (Knopf, 2003). Figure 3.1 illustrates the working principle of the droplet generator. Few μL of an aqueous solution is introduced into the ink channel. The solution is then heated by a resistor wire to form a gas bubble in the solution, which pushes a tiny amount of the liquid out through the nozzle as shown in Fig. 3.1. Single pulse mode was used to produce single droplets.

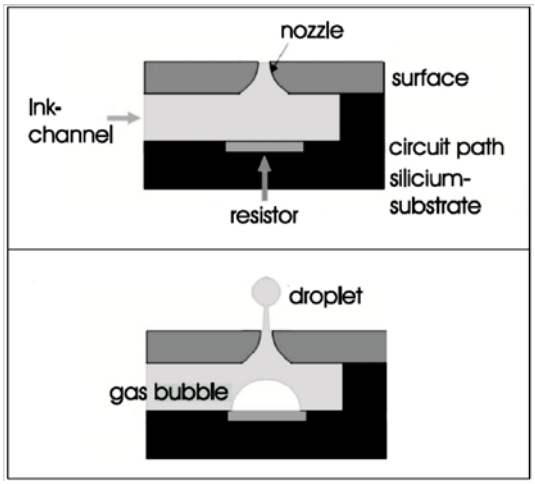

Figure 3.1 *A schematic representation of the droplet generator. Upper panel: the internal structure of the modified inkjet cartridge. Lower panel: the droplet formation process. Adapted from Knopf (2003).*

3.3 Experimental setup

Figure 3.2 shows the experimental setup used in this PhD work. It consists of an optical microscope (Olympus BX-40) and Raman spectroscope (Jobin Yvon, model: Labram) equipped with a custom-made temperature- and humidity-controlled flow cell (Fig. 3.3). This cell is a new design developed for this PhD work and optimized to the needs of the intended experiments. Specifically, it is very compact with inner dimensions of 20 mm in diameter and 0.1 – 0.2 mm in height to minimize the surfaces and has a well-controlled N_2/H_2O flow pattern.

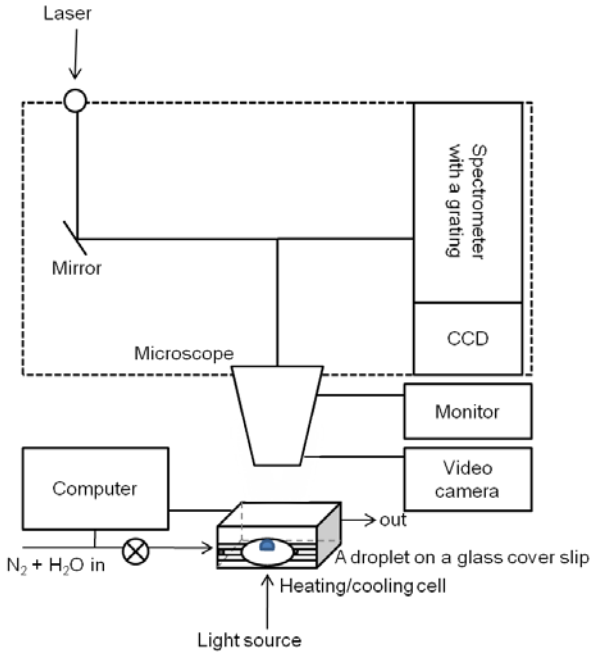

Figure 3.2 *Schematic diagram of the experimental setup. A single particle shown as blue half sphere is deposited on a hydrophobically coated glass slide. A detailed sketch of the heating/cooling cell is given in Fig. 3.3.*

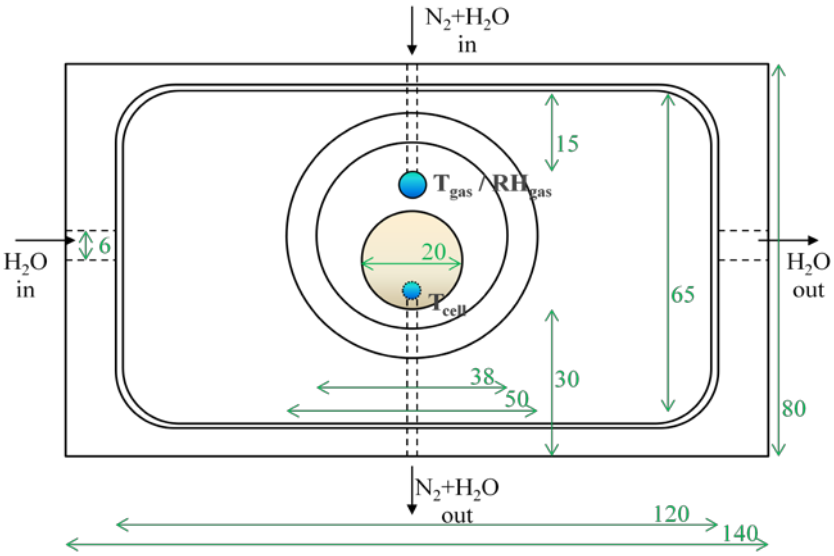

Figure 3.3 *Sketch of the custom-made temperature- and humidity-controlled flow cell. Droplets are deposited on a substrate (gray circle). Temperature and RH of gaseous N_2 + H_2O flow (T_{gas}/RH_{gas}) and temperature of the cell (T_{cell}) are measured by sensors (blue circles). Unit: mm.*

Droplets are deposited on a hydrophobically coated cover slip with dimensions of ~15 mm that is mounted in the cell. The cell is kept at constant temperature by water heating/cooling of the cell housing. RH is regulated by a N_2 + H_2O flow that is brought to cell temperature before entering the cell. A micrometer-sized single droplet on the hydrophobic glass slide is chosen and monitored with video microscopy during a humidity cycle. To change RH inside the flow cell, the water vapor mixing ratio of a constant total N_2 + H_2O flow (~180 sccm) is varied by mixing dry and water saturated N_2 flows using automatic mass flow controllers. Temperature and RH of the gas flow inside the cell are measured by a G-TUCN.34 sensor (U.P.S.I., France; capacity probe for RH , NTC for T) which is positioned about 15 mm downstream from the gas entrance.

The substrate temperature is also measured directly under the substrate by a Pt100 temperature sensor (Minco, USA). Adjustment of the flows through the mass flow controllers, readout of temperature and RH and the synchronization with the video signal was controlled by a PC using a custom-made VEE program (Agilent, USA). Morphological changes of the particle are monitored optically by the microscope equipped with a long working distance objective (magnification 50, aperture 0.7). A black and white CCIR video camera with an acquisition frequency of 25 frames s-1 and a PCO high-speed camera (set to 1420 frames s-1) were used to acquire images and movies of the droplet morphology. During typical experiments, the gas flow and the substrate temperatures are maintained at 293.2 ± 0.2 K. At the beginning of an experiment, the droplet was equilibrated at a RH of < ~ 100 % during 15 minutes. The RH was decreased continuously from ~100 % down to 25 % if (partial) efflorescence was observed and to ~ 0 % in case of no efflorescence. Subsequently, RH was continuously increased to ~ 100 % at a rate of 0.1 – 0.4 % min-1.

To identify the composition of the droplet phases, Raman spectra were acquired at constant RH and temperature conditions with the Raman system coupled to the optical microscope. In this study, the Raman system includes an external Nd:YAG laser (532 nm wavelength) as excitation source which is operated at 75 – 100 mW power for illumination. The laser beam is fed into the microscope. The backscattered light from the droplet is analyzed with an 1800 grooves mm-1 grating and a CCD camera. The Raman spectra are obtained in a range from 150 – 4000 cm-1 with a spectral resolution of about 2 – 4 cm-1 and a typical integration time of 200 s.

3.4 Calibration methods of RH and temperature sensors

The specified accuracy of the G-TUCN.34 RH sensor by the manufacturer is ± 2 % in the RH range from 2 – 98 %. However, we observed that this type of sensor might show offsets compared to the calibration curve provided by the company. We thus recalibrated the sensor by determining the RH of onset of deliquescence of pure inorganic salt crystals of KNO_3 (literature DRH at 293 K: 93.5 %), $(NH_4)_2SO_4$ (80.0 %), NH_4NO_3 (65.5 %), NaI

(38.0 %) and $MgCl_2 \cdot 6H_2O$ (33.0 %) (Winston and Donald, 1960), which cover a wide range of RH values. To do this, the RH in the cell was continuously increased at a rate of about 0.01 – 0.05 % RH min-1. Each DRH value was determined using at least two individual particles in the diameter range of 10 – 40 μm. With this calibration, the sensor proved to work accurately with deviations of about ± 1.5 %RH. In order to detect sudden offsets of RH, the calibration was checked by a DRH experiment with a pure AS crystal every two weeks when experiments have been performed. Figure 3.4 shows the calibration curve for a G-TUCN.34 RH sensor.

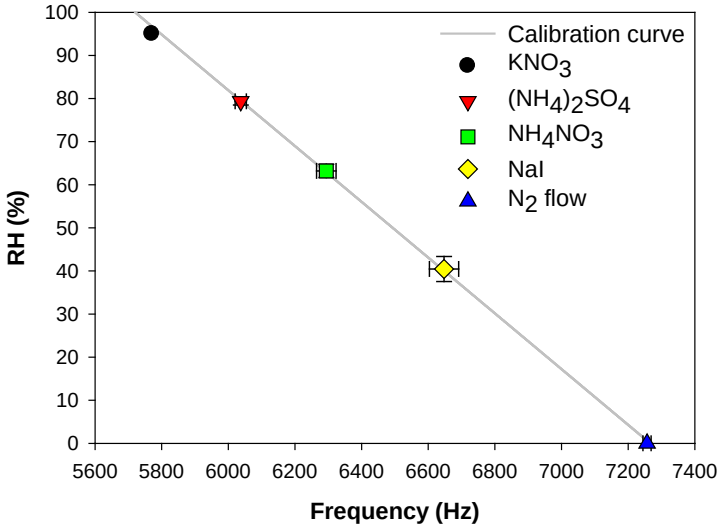

Figure 3.4 *Calibration curve for a G-TUCN. 34 RH sensor. Onset RH of deliquescence of the pure inorganic salts KNO_3 (black circle), $(NH_4)_2SO_2$ (red triangle), NH_4NO_3 (green square) and NaI (yellow diamond). Only N_2 flow: blue triangle. Error bars: standard deviation of experiments with different particles.*

We also calibrated the temperature sensors by observing the melting point of ice particles in a diameter range of 15 – 60 μm. Water droplets froze at about -35 °C in the cell and subsequently the temperature in the cell was continuously increased at a rate of about 0.03 °C min-1. We obtained an accuracy of the temperature sensor with deviations from the melting temperature of about ± 0.1 °C.

Chapter 4

Liquid-liquid phase separation and morphology of internally mixed dicarboxylic acids/ammonium sulfate/water particles

This chapter is a reproduction of the article published in the *Atmospheric Chemistry and Physics*:

Song, M., Marcolli, C., Krieger, U. K., Zuend, A., and Peter, T.: Liquid-liquid phase separation and morphology of internally mixed dicarboxylic acids/ammonium sulfate/water particles, Atmos. Chem. Phys., 12, 2691-2712, doi:10.5194/acp-12-2691-2012, 2012.

The layout of the article including the tables and figures has been revised to match with this thesis structure.

4.1 Abstract

Knowledge of the physical state and morphology of internally mixed organic/inorganic aerosol particles is still largely uncertain. To obtain more detailed information on liquid-liquid phase separation (LLPS) and morphology of the particles, we investigated complex mixtures of atmospherically relevant dicarboxylic acids containing 5, 6, and 7 carbon atoms (C5, C6 and C7) having oxygen-to-carbon atomic ratios (O:C) of 0.80, 0.67, and 0.57, respectively, mixed with ammonium sulfate (AS). With micrometer-sized particles of C5/AS/H_2O, C6/AS/H_2O and C7/AS/H_2O as model systems deposited on a hydrophobically coated substrate, laboratory experiments were conducted for various organic-to-inorganic dry mass ratios (OIR) using optical microscopy and Raman spectroscopy. When exposed to cycles of relative humidity (RH), each system showed significantly different phase transitions. While the C5/AS/H_2O particles showed no LLPS with OIR = 2:1, 1:1 and 1:4 down to 20 % RH, the C6/AS/H_2O and C7/AS/H_2O particles exhibit LLPS upon drying at RH 50 % to 85 % and ~90 %, respectively, via spinodal decomposition, growth of a second phase from the particle surface or nucleation-and-growth mechanisms depending on the OIR. This suggests that LLPS commonly occurs within the range of O:C < 0.7 in tropospheric organic/inorganic aerosols. To support the comparison and interpretation of the experimentally observed phase transitions, thermodynamic equilibrium calculations were performed with the AIOMFAC model. For the C7/AS/H_2O and C6/AS/H_2O systems, the calculated phase diagrams agree well with the observations while for the C5/AS/H_2O system LLPS is predicted by the model at RH below 60 % and higher AS concentration, but was not observed in the experiments. Both core-shell structures and partially engulfed structures were observed for the investigated particles, suggesting that such morphologies might also exist in tropospheric aerosols.

4.2 Introduction

Aerosol particles affect the Earth's energy budget directly by scattering and/or absorbing solar radiation and indirectly by acting as cloud

condensation and ice nuclei modifying cloud properties (Yu et al., 2006; IPCC, 2007). These effects are influenced by the aerosol size, physical state, chemical composition and morphology, which also affect the particle hygroscopicity (Hanel, 1976; Martin, 2000). Therefore, the interrelation between chemical composition and aerosol phase might be critical to attain a correct description of aerosol effects on climate.

The hygroscopic behavior of inorganic salts such as ammonium sulfate (AS), sodium chloride and ammonium nitrate have been well characterized (Tang and Munkelwitz, 1984; Tang and Munkelwitz, 1994; Cziczo et al., 1997; Martin, 2000). When crystalline particles of these inorganic salts are exposed to increasing relative humidity (RH), they take up water from the gas phase and become solution droplets at their deliquescence relative humidity (DRH). In turn, when the RH is decreased, the smaller solution droplets may reach high supersaturation before they crystallize and lose their water to the gas phase at the efflorescence relative humidity (ERH). While the inorganic aerosol constituents are relatively small in number and well known, the chemical composition of the organic matter is highly complex with a large fraction still unidentified (Decesari et al., 2006; Goldstein and Galbally, 2007). Field measurements showed that organic aerosol accounts for 30 % to 80 % of the total fine aerosol mass in various regions (Murphy et al., 2006; Zhang et al., 2007; Hallquist et al., 2009). Considering the high multitude of organic components present in the particle phase, the organics are expected to be in the liquid state or an amorphous solid state even at low RH in the atmosphere (Marcolli et al., 2004a). Owing to their larger size, deliquesced particles scatter the solar radiation more effectively than their effloresced analogs (Martin, 2000). Furthermore, liquid organic particles become increasingly viscous with decreasing temperatures and may attain a glassy state instead of efflorescing. Therefore, ice nucleation and ice crystal growth can be significantly impeded in organic-rich aerosol particles in the upper troposphere (Murray, 2008; Zobrist et al., 2008). Organic aerosol compositions span a large range from highly oxidized secondary matter to hydrophobic primary organic

matter, and are expected to separate into a more polar and a less polar phase (Pankow, 2003; Chang and Pankow, 2006; Zuend et al., 2010). Modeling particulate matter formation by forcing a single condensed phase when in reality two liquid phases are the preferred state leads to errors in the partitioning of water and semivolatile compounds, and thus to errors in the predicted composition and amount of particulate matter (PM), which may lead to an underprediction of organic PM by as much as 50 % (Erdakos and Pankow, 2004; Chang and Pankow, 2006; Zuend et al., 2010).

Organic and inorganic substances have been found to coexist internally mixed within aerosol particles (Lee et al., 2002; Murphy et al., 2006). Interactions between organic and inorganic components within an aerosol particle can influence DRH and ERH of inorganic salts or even totally suppress crystallization (Marcolli et al., 2004a; Parsons et al., 2006). Furthermore, liquid-liquid phase separation (LLPS) into a mainly polar inorganic and a less polar organic-rich phase during humidity cycles may occur (Marcolli and Krieger, 2006). To date direct experimental evidence of the physical state and morphology of submicron aerosols is scarce. Continuous water uptake observed in H-TDMA measurements indicates partially or totally liquid particles (e.g. Weingartner et al., 2002; Swietlicki et al., 2008). Martin et al. (2008), on the other hand, have observed deliquescence/efflorescence behavior of ambient particles in Oklahoma. Particle bouncing in an aerosol impactor and electron microscopy of biogenic secondary organic aerosol particles has been interpreted as evidence for solid amorphous, i.e. glassy particles at RH < 20 % (Virtanen et al., 2010). However, there is no measurement technique available at present that could observe LLPS in ambient aerosols directly. Therefore, laboratory experiments and model calculations are needed to infer the physical state for a given chemical aerosol composition. Zuend et al. (2010) recently presented a liquid-liquid equilibrium and gas/particle partitioning model that allows the reliable computation of LLPS of multicomponent systems. They use as a basis the group-contribution model called Aerosol Inorganic-Organic Mixtures Functional groups Activity Coefficients (AIOMFAC) (Zuend et al., 2008). Calculations that they performed for ternary and multicomponent alcohol/polyol-water-salt mixtures suggest that liquid-liquid equilibria are indeed a prevalent feature of organic-inorganic

aerosol systems. LLPS in smog chamber experiments is supported by a recent study of phase transitions and growth factors of mixed particles consisting of AS and secondary organic material prepared from α-pinene ozonolysis that are consistent with a model of phase separation into an aqueous electrolyte phase and an organic-rich phase in individual particles (Smith et al., 2011).

Particles consisting of two liquid phases can adopt different morphologies, e.g. fully engulfed core-shell structures or asymmetric partial engulfed structures. Knowledge of the aerosol morphology is important for determining the nature of the gas-particle interface, and thus the rate of heterogeneous chemical reactions, and the rate of water uptake (Cai et al., 1996; Fuzzi et al., 2006; Kwamena et al., 2010, Reid et al. 2011). Formation of organic coatings by condensation of monoterpene oxidation products onto aqueous sulfate particles is suspected to significantly reduce the heterogeneous hydrolysis rates of N_2O_5 (Folkers et al., 2003; Anttila et al., 2006; Anttila et al., 2007). Model simulations for Europe suggest that this process could decrease particulate nitrate concentrations by up to 90 % (Riemer et al., 2009). Strong reduction of N_2O_5 hydrolysis rates have also been observed for sulfuric acid and seasalt aerosols that were coated with organic surfactants (Thornton and Abbatt, 2005; McNeill et al., 2006; Cosman and Bertram, 2008; Cosman et al., 2008).

Ciobanu et al. (2009) used optical microscopy and micro-Raman spectroscopy to investigate LLPS of micrometer-sized droplets consisting of poly(ethylene glycol)-400 (PEG-400)/AS/water. The resulting morphology was an aqueous AS inner phase surrounded by a mainly PEG-400 containing outer phase. Core-shell morphologies have also been observed by Bertram et al. (2011) for mixed organic/AS particles deposited on a hydrophobically coated substrate. However, Kwamena et al. (2010) and Reid et al. (2011) have shown in model calculations and experiments that the adoption of a partially engulfed structure should predominate with the organic component forming a surface lens when the solubility of the organic component and the salting-out of the organic component to the surface by the presence of concentrated inorganic solutes in the aqueous phase are considered.

Previous studies on phase transitions of single aerosol particles have mostly been performed with one organic substance in the presence of AS (Parsons et al., 2006; Ling and Chan, 2008; Ciobanu et al., 2009; Yeung et al., 2009; Bertram et al., 2011). Studies on more complex organic mixtures are needed to obtain insight into the phase transitions of organic/inorganic aerosols considering atmospheric aerosol composition. In this study, we investigate single particles containing different dicarboxylic acids and AS during humidity cycles. Dicarboxylic acids are one of the most abundant organic compound classes in the troposphere (Decesari et al., 2006; Gilardoni et al., 2009; Hawkins et al., 2010). For our model systems, we mix together three isomeric acids to better mimic the complexity of real aerosol compositions. Three mixtures with C5, C6, and C7 dicarboxylic acids with oxygen-to-carbon ratios (O:C) of 0.80, 0.67, and 0.57, respectively were investigated. AS has been chosen as the model inorganic salt due to its abundance in the atmosphere and its well-characterized thermodynamic and spectroscopic properties (Braban and Abbatt, 2004; Ling and Chan, 2008; Yeung et al., 2009). To explore the phase diagram, we mixed the components in different organic-to-inorganic dry mass ratios (OIR). We use optical microscopy and micro-Raman spectroscopy to elucidate the phase transitions of these model systems when exposed to RH cycles. A main goal is to investigate the RH conditions and mixture compositions for which the model systems exhibit LLPS. The study of single particles allows for the investigations of miscibility gaps in solutions that are supersaturated with respect to a crystalline species and, hence, not directly accessible to bulk measurements. It also allows studying particle morphologies. Laboratory experiments of single aerosol particles are thus essential to improve our understanding of aerosol processes.

4.3 Experimental and modeling methods

4.3.1 Materials

Aqueous solutions containing different OIR of the three model systems were prepared by dissolving the pure substances in purified water (resistivity ≥

18.0 MΩcm). The mixture "C5" consists of three C5-dicarboxylic acids (glutaric, methylsuccinic, and dimethylmalonic acid), "C6" of three C6-dicarboxylic acids (2-methylglutaric, 3-methylglutaric, and 2,2-dimethylsuccinic acid), and "C7" of three C7-dicarboxylic acids (3-methyladipic acid, 3,3-dimethylglutaric acid and diethylmalonic acid), mixed together in equal mass (and molar) ratios. All components were purchased from Sigma-Aldrich with purities ≥ 98 % and were used without further purification.

4.3.2 Raman microscopy of single droplets

Figure 4.1 shows schematically the experimental setup. Single droplets in a new custom-made cell are investigated with a Raman microscope (Jobin Yvon, model: Labram). Using a droplet generator (Knopf, 2003), micrometer-sized aqueous droplets were deposited on a glass cover slip (≈ 15 mm diameter) that was hydrophobically coated by a silanization solution (Sigma-Aldrich) containing 5% dimethyldichlorosilane in heptane to avoid heterogeneous nucleation due to surface contact. The coating procedure is described in detail in Knopf (2003). The cover slip was mounted in the cell with inner dimension of 20 mm in diameter and 0.1 - 0.2 mm in height. The cell is kept at constant temperature (20 °C) by water cooling/heating of the cell housing. RH is regulated by a N_2/H_2O flow that is brought to cell temperature before entering the cell. A single droplet on the cover slip was chosen and monitored with video microscopy during a humidity cycle. To change RH, the water vapor mixing ratio of a constant total N_2/H_2O flow (180 sccm) was varied by mixing dry and water-saturated N_2 flows using automatic mass flow controllers. Temperature and RH of the gas flow inside the cell were measured by a G-TUCN.34 sensor (U.P.S.I., France; capacity probe for RH, NTC for T) which is positioned about 15 mm downstream from the gas entrance. During the experiments, the gas flow temperature was maintained at 20 ± 0.2 °C. The cell temperature was also measured directly on the substrate by a Pt100 temperature sensor (Minco, USA). The deviation between the two sensors was less than 0.3 °C. Adjustment of the flows through the mass flow controllers, readout of the temperature and humidity and the synchronization with the video signal was controlled by a

PC using custom software implemented in VEE (Agilent, USA). During humidity cycles, morphological changes of the droplet are monitored optically with the microscope equipped with a long working distance objective (Olympus BX-40, magnification 50, aperture 0.7). A black and white CCIR video camera with an acquisition frequency of 25 frames s-1 was used to acquire images and movies of the droplet morphology. At the beginning of the experiment, the droplet was equilibrated at high RH (~ 95 %). Humidity cycles comprise a RH reduction from 95 % to 20 % and subsequent increase from 20 % to 95 % at a rate of 0.1 - 0.3 % RH min-1.

To identify the composition of the droplet phases, Raman spectra were acquired at constant RH and temperature conditions with the Raman system coupled to the optical microscope. A Nd:YAG (532 nm wavelength) laser operated at 75 - 100 mW power was used as the excitation source. An 1800 grooves mm-1 grating and a CCD camera were used to analyze the backscattered light from the sample. We obtained Raman spectra at different positions on the particles in the range of 150 - 4000 cm-1 with a spectral resolution of about 2 - 4 cm-1 and an integration time of 200 s.

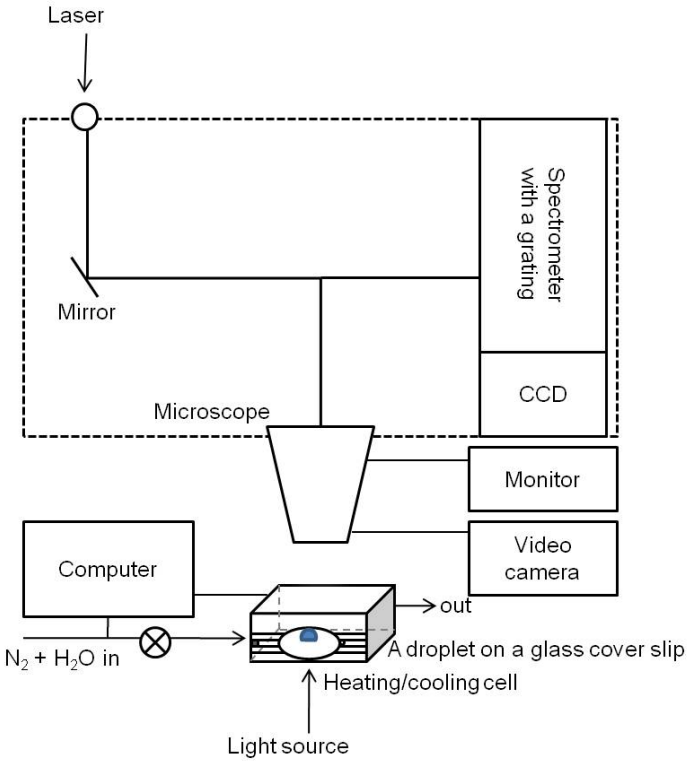

Figure 4.1 *Schematic representation of the experimental setup. A single particle (shown as blue half sphere) is deposited on a hydrophobically coated slide glass.*

4.3.3 RH and temperature sensor calibrations

The specified accuracy of the G-TUCN.34 RH sensor by the manufacturer is ± 2 % in the RH range from 2 – 98 %. However, we observed that this type of sensor might show offsets compared to the calibration curve provided by the company. Therefore, by measuring the DRH of various pure inorganic salts at room temperature, such as KNO_3 (93.5 %), $(NH_4)_2SO_4$ (80.0 %), NaCl (75.0 %), NH_4NO_3 (65.5 %), NaI (38.0 %) and $MgCl_2 \cdot 6H_2O$ (33.0 %), which cover a wide range of RH values, we recalibrated the G-TUCN.34

RH sensor. To do this, the RH in the cell was continuously increased at a rate of about 0.05 % RH min-1 and the RH value at which onset of deliquescence was observed was registered as the DRH and compared with literature values. Each DRH value was determined using at least two independent particles in the diameter range of 10 – 35 µm. With this calibration, we obtained an accuracy of the humidity sensor of ± 1.5 % RH. In order to detect sudden offsets of RH, the calibration was checked by a DRH experiment with a pure AS crystal every two weeks when experiments have been performed. We calibrated the temperature sensors by determining the melting point of ice particles using the same procedure as described in Knopf and Lopez (2009). Water droplets of 15 – 60 µm in diameter froze at about – 35 °C in the cell. Subsequently, the ice melting point was determined using a heating ramp of 0.03 °C min-1. The temperature sensors proved to work accurately with deviations from the melting temperature of about ± 0.1°C.

4.3.4 Saturation solubility and water activity measurements

To determine the physical properties of the dicarboxylic acids and AS, we measured their individual solubility in water and the water activity (aw) of the saturated solutions. By stepwise adding small portions of water until the solute was completely dissolved, saturated aqueous solutions were prepared. The solutions were allowed to equilibrate in a thermostated water bath at 25.0 ± 0.1°C in between the additions. The estimated uncertainty of this procedure is less than 1.0 wt %. The a_w of the saturated aqueous solutions were measured at 25 °C, using a water activity meter (AquaLab Model 3TE, Decagon Devices, USA). In order to correct for instrument offset and drift, the performance of the sample block was frequently controlled and readjusted with reference samples (Marcolli and Krieger, 2006). The experimental errors for the measurements with standard samples such as KNO_3 (aw = 0.925) and NaCl (aw = 0.753) were ± 0.002 aw and ± 0.009 a_w, respectively.

4.3.5 Thermodynamic modeling

We use the method developed by Zuend et al. (2010) for the computation of LLPS in mixed organic/inorganic systems. This method is based on the global minimization of the Gibbs energy of a system to find the number of phases and corresponding compositions at thermodynamic equilibrium. In order to calculate the Gibbs energy at a given composition, activity coefficients of all components are required to account for non-ideal mixing. Following Zuend et al. (2010), we use the group-contribution model AIOMFAC developed by Zuend et al. (2008) with the new and extended set of organic/inorganic interaction parameters determined by Zuend et al. (2011). This recent implementation of the new AIOMFAC model parameters to describe interactions between various important organic functional groups and inorganic ions enables the computation of activity coefficients in multicomponent mixtures such as those investigated in this study.

Phase separation computations were performed at 298 K for the three 5-component systems C5/AS/H_2O, C6/AS/H_2O, and C7/AS/H_2O with the components as given in Table 4.1. In addition, phase diagrams for three corresponding 3-component systems were computed, each containing only one of the dicarboxylic acids (one of the C5, C6, or C7 diacids used in the 5-component systems), AS, and water. In contrast to a laboratory experiment, in a model calculation the potential crystallization of a single dicarboxylic acid in a mixture can be suppressed. Hence, the ternary systems allow a direct comparison with the results for the corresponding 5-component systems at the same dry (water-free) mass fractions of AS (mf_d(AS)), mf_d(AS) = mass(AS) / mass(organics + AS)). Such comparisons of the 5-component with 3-component systems allow an evaluation of the influence of using a mixture of three structural isomers for the organic fraction versus only one corresponding organic compound in AIOMFAC group-contribution model calculations. Furthermore, the ternary systems are of use as they allow a mathematically simpler computation of metastable and unstable regions of the phase diagram employing the algorithm of Zuend et al. (2010), as detailed in Sect. 4.4.5. In the calculations of the miscibility gap, the formation of crystalline AS at concentrations above its solubility limit was ignored, instead all AS is kept in the liquid mixture, leading to

supersaturated solutions at lower water contents, corresponding to the drying branch of the humidity cycles in the experiments, down to the efflorescence of AS.

4.4 Results and discussion

4.4.1 Physical properties of the investigated mixtures

Table 4.1 presents solubility and aw of saturated solutions of the dicarboxylic acids at 25°C. Despite their quite high solubility in water, aw of the saturated solutions are high compared with values obtained for inorganic solutions of similar mass concentrations. This is due to the comparably high molecular weights of the dicarboxylic acids, their negligible degree of dissociation in solution together with only moderate hydrophilicity. The increasing hydrophobic nature with increasing carbon number is reflected by the oxygen-to-carbon atomic ratios (O:C), also given in Table 4.1, which decreases from the C5 to the C7 dicarboxylic acids from 0.80 to 0.57. Instead of using one dicarboxylic acid, three acids of equal carbon number are mixed together in mixtures C5 – C7 to better mimic the effect of a complex mixture of compounds in the organic fraction of real aerosols, in which crystallization of organic components during humidity cycles is effectively suppressed due to the many components, as discussed in Marcolli et al. (2004b). In this context, the straight chain C6 and C7 dicarboxylic acids (adipic and pimelic acid) were excluded from the mixtures because of their low aqueous solubility and related limited crystallization suppression of these dicarboxylic acids when the organic fraction is only represented by three compounds.

For the following experiments, a C5 mixture consisting of the three C5 components, a C6 and a C7 mixture were prepared. In a first step, single droplets of these purely organic mixtures were injected into the cell and investigated in the microscope. They remained as one liquid phase droplets down to dry RH conditions and did neither show LLPS nor efflorescence. In a second step, these three-component organic mixtures were mixed together with AS and water in different OIR and investigated as single droplets. The following section shows examples of time sequences for OIR = 1:1. In Sect.

4.4.3 the chemical compositions of the observed phases are discussed. In Sects. 4.4.4 and 4.4.5, experimental and calculated phase diagrams are presented and discussed. Considerations of particle morphologies are given in Sect 4.4.6.

Table 4.1 *Molecular weights (MW), aqueous solubility in weight percent at 25°C, water activities (a_w) of saturated solutions at 25°C, oxygen-to-carbon atomic ratios (O:C) and hydrogen-to-carbon atomic ratios (H:C) of investigated dicarboxylic acids and AS.*

System components	MW (g/mol)	Solubility (wt %)	a_w of saturated solution	O:C	H:C
C5					
Glutaric acid	132.12	58.8	0.883		
Methylsuccinic acid	132.12	32.0	0.943	0.80	1.60
Dimethylmalonic acid	132.12	10.5	0.979		
C6					
2-methylglutaric acid	146.14	52.7	0.929		
3-methylglutaric acid	146.14	45.3	0.935	0.67	1.67
2,2-dimethylsuccinic acid	146.14	8.3	0.982		
C7					
3-methyladipic acid	160.17	17.1	0.979		
3,3-dimethylglutaric acid	160.17	14.2	0.982	0.57	1.71
Diethylmalonic acid	160.17	19.5	0.979		
AS	132.14	43.2	0.802		

4.4.2 LLPS features of C5/AS/H_2O, C6/AS/H_2O and C7/AS/H_2O droplets

Humidity cycles were performed with 4 droplets of C5/AS/H_2O, 9 droplets of C6/AS/H_2O, and 5 droplets of C7/AS/H_2O all with OIR = 1:1 and dry diameters in the range of 20 - 60 µm. Figure 4.2 exemplifies the phase and morphological changes that were observed optically. At the beginning of the humidity cycles at high RH (set to time t = 0), the droplets displayed only one liquid phase as shown in the first frames of Figs. 4.2a, 4.2b and 4.2c, taken at RH of 87 %, 78 % and 90 %, respectively.

The C5/AS/H_2O droplet effloresced at 39.2 % RH (t = 138 min, Fig. 4.2a) upon drying without showing any evidence of precedent LLPS. This value is within the range of ERH of pure AS particles (e.g. Ciobanu et al., 2010). This together with the finding that pure C5/H_2O (AS-free) droplets did not effloresce during humidity cycles down to 20 % RH indicates that nucleation of AS initiated the efflorescence process. Upon subsequent moistening, the effloresced particle gradually absorbed water, followed by sudden dissolution of most solid material at ≈ 77.5 % RH (t = 251 min). Some crystals remained up to ≈ 85.2 % RH, when discernible dissolution again set in (t = 275 min). This high DRH cannot be ascribed to the deliquescence of AS and shows that at least a part of the C5 dicarboxylic acids crystallized, probably by heterogeneous nucleation on AS crystals. To ascertain the dissolution order of the substances, we also conducted a bulk measurement at 20 °C by adding water stepwise to the crystalline C5/AS mixture until a clear solution was obtained. We observed by eyes that the AS crystals were completely dissolved at aw = 0.79 ± 0.004 with the glutaric and methylsuccinic acids. Therefore, it indicates that AS in C5/AS/H_2O deliquesced at between 77.5 % and 79.0 % RH.

LLPS was observed for the C6/AS/H_2O droplet by the abrupt appearance of schlieren at 73.4 % RH (t = 30 min, Fig. 4.2b) upon water evaporation. Such schlieren (Kostorz, 2001), which appear as small separated regions all over a droplet are involved in spinodal decomposition. The schlieren developed into small droplets that coalesced to form an inner phase within the particle. Ciobanu et al. (2009) have also observed spinodal decomposition for LLPS of PEG-400/AS/H_2O particles. At 71.9 % RH, inner and outer phases

together with satellite inclusions can be clearly discriminated in the liquid droplet. Interestingly, after LLPS had occurred, the inner phase that was confirmed to consist of aqueous AS by Raman spectroscopy (see Sect. 4.4.3) tended to move from the core toward the edge of the particle as more water was released. This partially engulfed configuration can be seen at 67.2 % RH in Fig. 4.2b. Such particle morphology has recently been postulated by Kwamena et al. (2010) and Reid et al. (2011). A further decrease in RH leads to efflorescence and crystal growth in both phases of the particle at 46.3 % (t = 238 min). This value is above the typical range observed for ERH of pure AS droplets (e.g. Ciobanu et al., 2010) and will be discussed in more detail in Sect. 4.4.4. For subsequently increasing RH, the crystals in the outer phase deliquesced first, followed by fast dissolution of the solid material in the inner phase at 79.1 % RH. When AS had deliquesced at 79.6 % RH, a remnant of crystallized organic material, most likely 2,2-dimethylsuccinic acid (considering results of bulk measurement using the same method as for the C5/AS) remains (marked by an arrow on Fig. 4.2b, t = 782 min). The particle fully deliquesced as one liquid phase at 87.4 % RH.

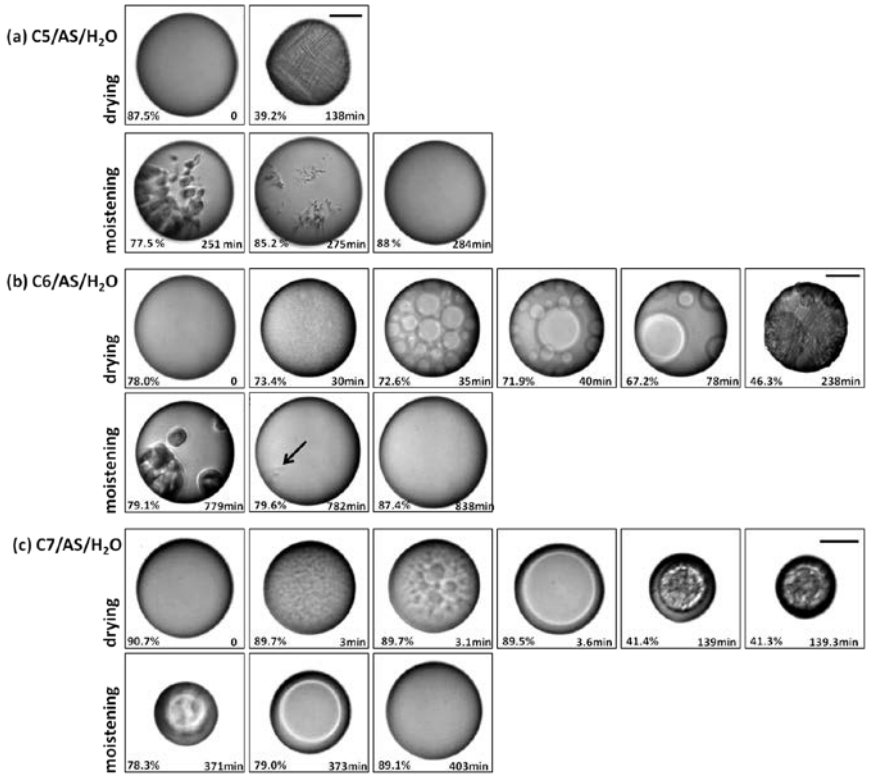

Figure 4.2 *Humidity cycles of (a) C5/AS/H_2O particle (top rows, dRH/dt = ± 0.33 %/min), (b) C6/AS/H_2O particle (center rows, dRH/dt = ± 0.14 %/min), and (c) C7/AS/H_2O particle (bottom rows, dRH/dt = ± 0.34 %/min) all with OIR = 1:1. At time t = 0, all particles are present as droplets with a single liquid phase. Size bar: 20 µm.*

In the C7/AS/H_2O droplet shown in Fig. 4.2c, LLPS was induced by spinodal decomposition at RH as high as 90 % (t = 3 min) when the humidity was decreased. Schlieren formation and coalescence can be seen at almost the same RH (t = 3 min and 3.1 min in Fig. 4.2c) leading to a core-shell morphology without satellite inclusions in the outer phase at t = 3.6 min. It is interesting to note that the core-shell or completely engulfed morphology is the main configuration in the C7/AS/H_2O particle for OIR =

1:1 while for C6/AS/H_2O droplets the partially engulfed morphology prevailed. A gradual loss of water resulted in a shrinkage of the particle until the inner phase effloresced at 41.4 % RH. The outer phase that was confirmed to consist mainly of organics (see Sect. 4.4.3) did not seem to crystallize, probably because the very low AS concentration or a high viscosity in this phase derates crystal growth. Rather, it was sucked into cavities of the crystalline inner phase within a few seconds (t = 139.3 min) most probably because of capillary forces (Sjogren et al., 2007). Undergoing water uptake, the particle deliquesced and returned into a two-liquid-phases state at 79 % RH. In contrast to the C6/AS/H_2O particle (Fig. 4.2b, t = 782 min), the C7/AS/H_2O particle shows no remaining solid above the DRH of AS. The two liquid phases merged into one liquid phase at 89.1 % RH.

4.4.3 Chemical compositions of the different phases

To identify the chemical composition of the different phases present in C6/AS/H_2O and C7/AS/H_2O particles which have shown LLPS, we collected Raman spectra at constant RH on particles with OIR = 1:1. Figure 4.3 depicts representative Raman spectra collected at different positions as indicated in the optical images of the particles. Spectra of an AS crystal (Fig. 4.3 (c1)) and a liquid droplet of purely organic 3-components C6 and C7 mixtures at RH = 0 % are also included as references (Fig. 4.3 (c2)). The most prominent feature in the reference spectrum of crystalline AS is the symmetric stretching vibration of SO_4^{2-} at ~ 975 cm^{-1} (Zhang and Chan, 2002; Ling and Chan, 2008; Ciobanu et al., 2009). The band of the stretching vibration of NH_4^+ at around 3130 cm^{-1} (Ciobanu et al., 2009; Yeung et al., 2009) is also distinguished. The C6 and C7 references reveal C-H stretching vibrations at 2880 - 2984 and 2875 - 2990 cm^{-1}, respectively, and several peaks between 700 and 1670 cm^{-1}. The C=O stretching vibrations appear as relatively sharp peaks at ~1656 cm^{-1} for the C6 and at ~1658 cm^{-1} for C7 mixtures.

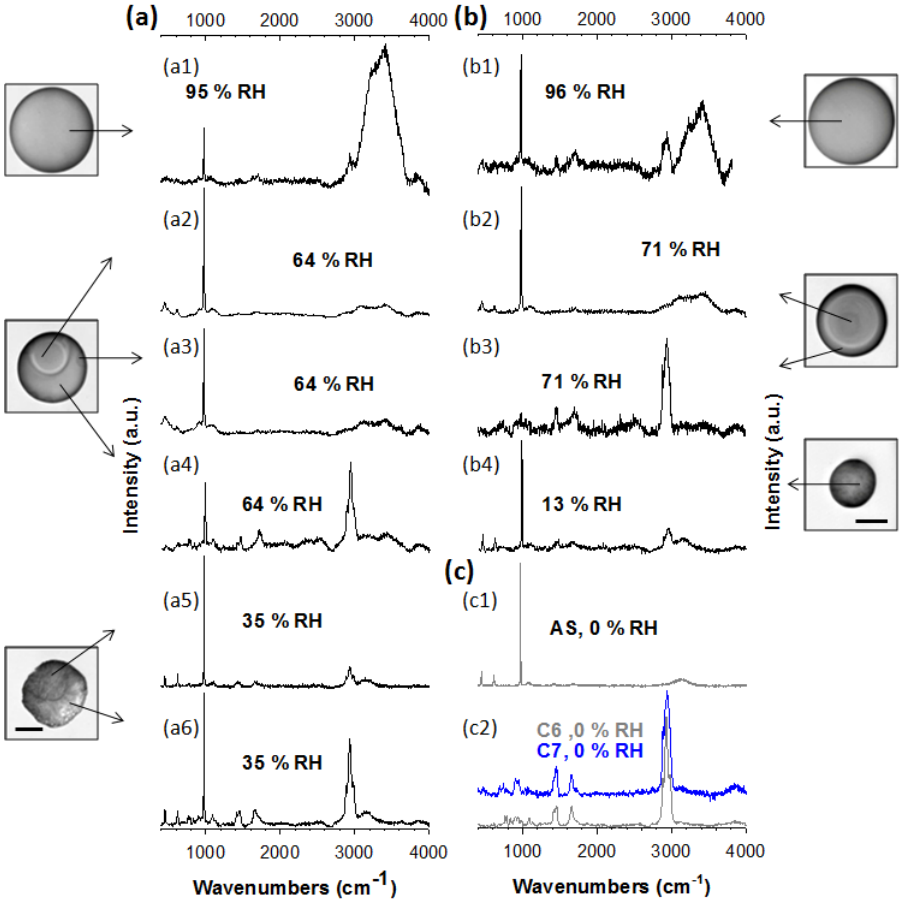

Figure 4.3 *Raman spectra and microscopic images of (a) C6/AS/H_2O and (b) C7/AS/H_2O particles with OIR = 1:1 at different RH. Reference spectra are included for AS (c1) and for the pure C6 and C7 organic mixtures (c2). Size bars in the microscopic images are 20 µm.*

In the one-liquid-phase state of C6/AS/H_2O and C7/AS/H_2O droplets, the sharp peak at ~980 cm^{-1} and the broad band between 2870 and 3000 cm^{-1}, originating from AS and dicarboxylic acids, respectively ((a1) and (b1) of Fig. 4.3), are clearly visible. In addition, at this high RH, symmetric and

antisymmetric O-H stretching modes of water molecules can be detected as an additional intense broad band in the range of 3030 – 3700 cm^{-1} (Yeung et al., 2009). This is clear evidence for the presence of both AS and organics in one aqueous phase.

At 64 % RH, when the C6/AS/H_2O droplet is in the two-liquid-phases state, Raman spectra were collected from the satellite inclusions, the inner phase and the outer phase. As shown by the dominance of the AS peak at 979 cm^{-1}, the low intensity of the water band and the hardly visible spectral features of the dicarboxylic acids in spectra (a2) and (a3) of Fig. 4.3a, the inner phase and the satellite inclusions consist of a concentrated aqueous AS solution containing only small amounts of organics. On the other hand, spectrum (a4) acquired from the outer phase of C6/AS/H_2O shows well discernable signals of the dicarboxylic acids and the AS and water bands appear only as weak features, establishing the outer phase as highly concentrated aqueous dicarboxylic acid solution with AS as a minor component (see also Ciobanu et al., 2009; Smith et al., 2011).

Raman spectra of the outer and the inner phases of the C7/AS/H_2O droplet measured at 71 % RH give evidence of an almost complete phase separation: the dicarboxylic acid peaks are hardly visible in the Raman spectrum of the inner aqueous AS phase ((b2) of Fig. 4.3b) and the main AS peak at 979 cm^{-1} is very weak in the Raman spectrum of the outer organic-rich phase (b3). Also, the spectral signature of the water band can be hardly detected in the organic-rich phase indicating its low water content. More complete phase separation in the C7/AS/H_2O system than in the C6/AS/H_2O system is expected because of the more hydrophobic nature (lower O:C) of the C7 compared with the C6 dicarboxylic acids.

Spectra of the effloresced particles were collected at 35 % and 13 % RH for the C6/AS/H_2O and the C7/AS/H_2O droplets, respectively. For both systems efflorescence of the AS component is confirmed by the increased sharpness of the peaks at 451 and 614 cm^{-1} and the shift of the main peak from ~979 to ~975 cm^{-1}. Such effects due to the crystallization of AS have been described by Zhang and Chan (2002) and Ciobanu et al. (2009). The Raman spectra do not provide any clear evidence of the phase state of the dicarboxylic acids. The distribution of the two liquid phases within the droplet is mostly

conserved during efflorescence as can be seen optically and from comparison of the Raman spectra (c1) and (c2) of Fig. 4.3c: the effloresced inner phase is enriched in crystalline AS compared with the outer phase. Nevertheless, a certain remixing of the phases takes place after efflorescence, as can be clearly seen from the increased intensity of the dicarboxylic acid spectral features in the inner phase of the C6/AS/H_2O droplet after efflorescence (spectrum (a5) compared with (a2)) and in the inner phase of the C7/AS/H_2O droplet (spectrum (b4) compared with (b2)). We assume that this remixing is driven by capillary forces that act in veins of polycrystalline AS and cavities between AS needles.

4.4.4 Phase diagrams of C6/AS/H_2O and C7/AS/H_2O systems

To fully assess the dependence of LLPS on mixing ratio and RH and to establish corresponding phase diagrams, C5/AS/H_2O, C6/AS/H_2O and C7/AS/H_2O particles with different OIR were investigated at 20°C. We performed small humidity cycles (from 95 % to 60 % to 95 %) to determine whether there is a hysteresis between the onset of LLPS upon drying and the merging of the two liquid phases upon moistening, and large humidity cycles (from 95 % to 20 % to 95 %) to observe efflorescence and deliquescence processes. Typically, a small humidity cycle was followed by a large one. For some particles, we performed one to several large humidity cycles. The sizes of the investigated droplets were in the range from 24 - 75 μm diameters.

In the C5/AS/H_2O particles LLPS did not occur for the investigated OIR = 2:1, 1:1 and 1:4, instead, efflorescence occurred at 32.4 %, 37.9 %, and 40.8 % RH, for OIR = 2:1, 1:1, and 1:4, respectively. If LLPS occurred in this system, it would be at RH < ERH. However, LLPS appeared in both C6/AS/H_2O and C7/AS/H_2O systems over a broad composition range. Figure 4.4 presents phase diagrams of (a) C6/AS/H_2O and (b) C7/AS/H_2O systems as a function of RH in terms of mf_d(AS) (lower x-axis) and OIR (upper x-axis).

In C6/AS/H_2O particles LLPS occurred upon drying for mf_d(AS) of 0.07 - 0.89. Humidity cycles performed between 95 % and 60 % RH show no

discernable hysteresis between onset and end of LLPS, i.e., the open and filled black circles in both Figs. 4.4a and b coincide within experimental uncertainties. The experiment carried out at $mf_d(AS) = 0.92$ did not show any discernable LLPS, marking the end of the miscibility gap to high AS concentrations, though we cannot exclude the possibility that separation occurred but could not be detected because of lack of contrast. For $mf_d(AS) = 0.30 - 0.89$ the onset and end of LLPS is in the narrow range from 72 - 74 % RH. On the other hand, in C7/AS/H_2O particles we observed LLPS over the whole investigated composition range with onset values between 84 - 92 % RH upon drying and end values between 86 - 90 % RH during moistening, i.e., with no discernable hysteresis (Fig. 4.4b). The larger miscibility gap of the C7/AS/H_2O compared with the C6/AS/H_2O system in terms of composition and RH range is consistent with the more hydrophobic character of the C7 compared with the C6 dicarboxylic acids.

A further decrease in RH leads to efflorescence of the particles. In Figs. 4.4a and b the average ERH of all experiments carried out with the same composition are shown as green filled circles, ERH of individual crystallization events as red filled circles. Open red circles show cases when crystal growth was very slow and mark the state with full needle coverage (this RH value depends on the rate at which particles were dried). The ERH scatters between individual experiments because nucleation is a stochastic process (Martin, 2000) while the instrumental uncertainty is smaller than this scatter by factors 3 to 4. In general, ERH decreases as AS concentrations decrease. For $mf_d(AS) \geq 0.5$, ERH values range from 35 – 48 % RH for the C6/AS/H_2O system and between 36 – 48 % RH for the C7/AS/H_2O system as well. These ranges are at the high end or above ERH observed for other dicarboxylic acid/AS/H_2O systems: e.g. Parsons et al. (2004) and Zardini et al. (2008) report ERH for malonic acid/AS, glutaric acid/AS, and citric acid/AS particles consistently below 40 %. A possible explanation for the high ERH values observed in this study might be an increase of the ion activity coefficients due to the energetically disadvantageous interactions between the ions of AS and the C6 and C7 dicarboxylic acids, enhancing the probability for the formation of stable AS crystal nuclei at higher RH as compared to mixtures with the more

hydrophilic malonic (C3 dicarboxylic acid), glutaric (C5 dicarboxylic acid) and citric acids.

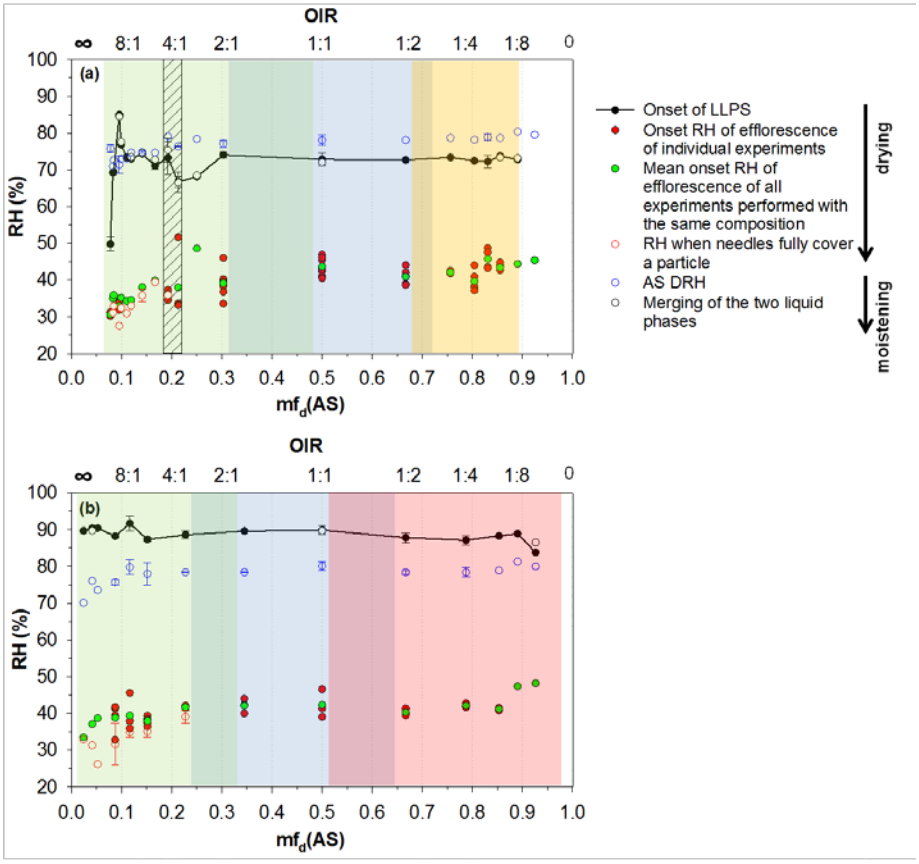

Figure 4.4 *Phase diagrams of (a) C6/AS/H_2O and (b) C7/AS/H_2O from humidity cycles. Black filled circles: LLPS onset. Red filled circles: efflorescence onset (mean values in green). Red open circles: completion of efflorescence. Blue open circles: AS deliquescence upon moistening. Black open circles: merging of the two liquid phases upon moistening. Background shadings represent different LLPS mechanisms upon drying: nucleation-and-growth (green), spinodal decomposition (blue), growth of a second phase at the surface of the particle (pink) and mechanism unclear*

(orange). Hatched area in (a): inconstant LLPS varying among different particles in the range of 0.19 < mf_d(AS) < 0.21. Error bars: standard deviation of experiments with different particles.

Figure 4.5 illustrates nucleation and crystal growth of AS for a C6/AS/H_2O particle with OIR = 11:1. The main phase of this particle is organic-rich. Aqueous AS inclusions are marked by arrows. Crystallization started from the rim of the particle at 35 % RH and slowly proceeded until after 6.5 min the particle was fully covered with needles. Because our experiments were carried out at constant drying rate, this translates to a crystal growth that occurs over several percent in RH until a droplet is fully covered by needles as indicated in Fig. 4.4 (open red circles). The needles mostly consist of AS because they deliquesce at around the DRH of AS (open blue circles in Fig. 4.4). The aqueous AS inclusions crystallized when the AS needle had reached them. We attribute the slow crystal growth to the high viscosity that is reached in the organic-rich phase.

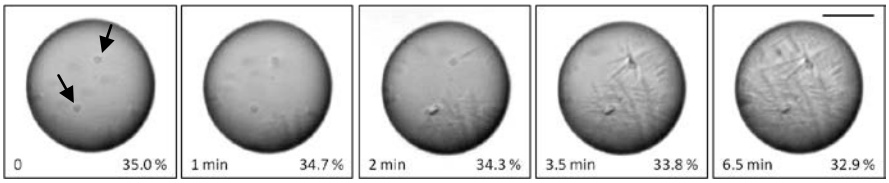

Figure 4.5 *Efflorescence process of a C6/AS/H_2O particle with mf_d(AS) = 0.083 (OIR = 11:1) from onset of efflorescence at 35.0 % until the particle is fully covered by needles at 32.9 % RH. Size bar: 20 µm. Aqueous AS inclusions are marked by arrows.*

Upon increasing RH, deliquescence of AS occurred between 70 % - 80 % RH for both systems over the whole composition range. This is in good agreement with previous work (Braban and Abbatt, 2004; Parsons et al., 2004; Sjogren et al., 2007; Ling and Chan 2008; Smith et al., 2011). Upon moistening, the C6/AS/H_2O and C7/AS/H_2O particles showed noticeably

different behavior. Whereas C6/AS/H_2O particles returned into a one-liquid phase state upon deliquescence of AS, a two-liquid-phases state was restored when AS deliquesces in C7/AS/H_2O particles. The reason for this different behavior is that for C7/AS/H_2O the miscibility gap extends to RH > AS DRH while the miscibility gap of C6/AS/H_2O is restricted to compositions that are supersaturated with respect to AS and therefore ends at RH < AS DRH.

In the C6 system, the situation is intricate at low AS concentration. LLPS was clearly visible for $mf_d(AS) \approx 0.1$. In this concentration range, the highest observed onset of LLPS occurred (at RH ≈ 85 % RH for $mf_d(AS) = 0.095$, OIR = 9.5:1). For $mf_d(AS) = 0.08$, LLPS drops to 50 % RH marking the end of the miscibility gap to low AS concentrations. Surprisingly, for mf_d (AS) = 0.19 and 0.21 (hatched area in Fig. 4.4a) LLPS was only detectable in 7 out of 12 and 7 out of 9 experiments, respectively. In cases with detectable LLPS, the onset RH scattered over quite a large RH range of 65 - 78 %. Interestingly, this large range cannot be explained by kinetically limited nucleation of the minor phase because no phase separation hysteresis could be observed when exposing the same particle to humidity cycles. Some particles showed reproducible LLPS during several humidity cycles while LLPS was reproducibly absent in others.

In order to clarify LLPS at high OIR in the C6/AS/H_2O system, we collected Raman spectra of the C6/AS/H_2O and the C7/AS/H_2O systems in the one-liquid-phase state and in the organic-rich phase of the phase separated system for different $mf_d(AS)$, see Fig. 4.6. From theory, we expect that mixtures with OIR within the miscibility gap partition into an organic-rich and an aqueous AS phase with constant compositions corresponding to the ones of the limits of the miscibility gap, irrespective of their OIR. This should be strictly true for systems measured at the same RH. The organic-rich phase (given by the red circles in Fig. 4.6) should therefore exhibit a constant dicarboxylic acid/AS Raman peak ratio irrespective of the OIR. By comparing the Raman peak height ratios of the organic-rich phase with the ones in the one-liquid-phase state, it is furthermore possible to estimate the AS concentration of the organic-rich phase. To do this, we use the C6 (2931 cm^{-1}) / AS (979 cm^{-1}) and the C7 (2937 cm^{-1}) / AS (979 cm^{-1}) Raman peak height ratios of the one-liquid-phase states (at 85 % and 95 % RH for the

C6/AS/H_2O and C7/AS/H_2O systems, respectively) as a measure of AS concentration given as mf_d(AS) on the x-axis of Fig. 4.6. From this, we deduce an estimate of the AS concentration in the organic-rich phase in the phase separated system at RH = 65 %. Figure 4.6b shows a constant C7/AS ratio of ~15 corresponding to mf_d(AS) well below 0.1 for the organic-rich phase of the C7/AS/H_2O system – as expected from theory. The organic-rich phase of the C6/AS/H_2O system exhibits a C6/AS ratio of ~1 that corresponds to mf_d(AS) ~0.3 for overall compositions of mf_d(AS) = 0.50 and 0.67 (Fig. 4.6a). This implies that the miscibility gap of this system is less complete than the one of the C7/AS/H_2O system and should end at mf_d(AS) ~0.3. However, the observed phase separation persists to lower mf_d(AS), and, in addition, the AS content of the organic-rich phase is no longer a constant but decreases with decreasing mf_d(AS) of the particle (corresponding to an increase of the C6/AS ratio up to ~8 for an overall mf_d(AS) of 0.08). This implicates that C6/AS/H_2O systems with mf_d(AS) below 0.3 do not exhibit a typical LLPS. This issue will be discussed in detail in Sect. 4.4.5.

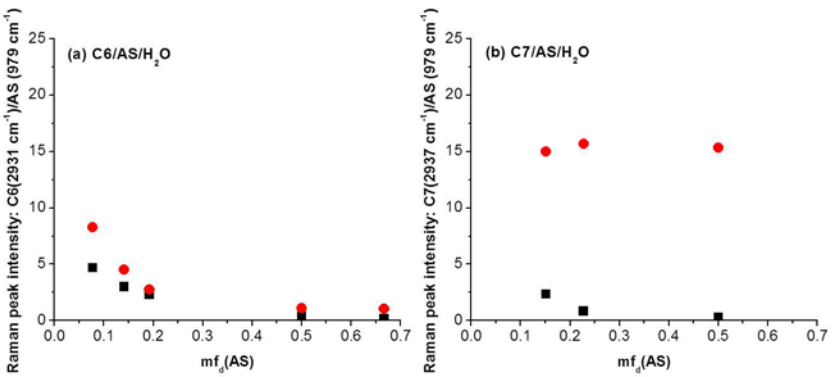

Figure 4.6 *(a) Ratios of C6 (2931 cm^{-1}) to AS (979 cm^{-1}) Raman peak intensities of a C6/AS/H_2O particle in the one-liquid-phase state at RH = 85 % (black squares) and of the organic-rich phase in the two-liquid-phases state at RH = 65 % (red circles), and (b) ratios of C7 (2937 cm^{-1}) to AS (979 cm^{-1}) Raman peak intensities of a C7/AS/H_2O particle in the one-liquid–*

phase state at RH = 95 % (black squares) and of the organic-rich phase in the two-liquid-phases state at RH = 65 % (red circles) as a function of the overall $mf_d(AS)$.

Ciobanu et al. (2009) found that LLPS may occur by spinodal decomposition, nucleation-and-growth, and growth of a second phase at the surface of the particle depending on OIR within internally mixed PEG-400/AS/H_2O particles. Nucleation-and-growth typically occurs in the metastable region of the phase diagram and is associated with overcoming an energy barrier to form stable nuclei of the second phase while spinodal decomposition occurs without a nucleation energy barrier at the border to the unstable region of the phase diagram (Shelby, 1995; Papon et al., 1999). To determine the different LLPS mechanisms from the microscopic images, we used the same methods as described by Ciobanu et al. (2009), which rely on the analysis of droplet morphology at the onset of phase separation and the evaluation of the number of AS inclusions as a function of time. Such assignment of phase separation mechanism is always prone to uncertainties because the very first stages of LLPS are not visible in optical microscopes due to limitations in spatial resolution and optical contrast. Given these limitations, in the C6/AS/H_2O systems, LLPS occurring at $0.07 < mf_d(AS) < 0.40$ matched best with a nucleation-and-growth mechanism whereas spinodal decomposition seemed to occur for $0.40 < mf_d(AS) < 0.70$ (Fig. 4.4a). However, we were not able to determine the separation mechanism for LLPS occurring at $0.70 < mf_d(AS) < 0.89$ in the C6/AS/H_2O systems (Figs. 4.4a) because the very first instances of phase separation are not clearly discernable due to lack of optical contrast. Figure 4.7a shows as an example for this case a time sequence of a droplet with OIR = 1:4. This droplet remained very dynamic with continuous appearance and coalescence of inclusions for a time period over 30 min (corresponding to an RH change of 20 %). Here, the organic-rich phase does not seem to spread on the aqueous AS phase but to form droplets or lenses on the surface which might be moved by the N_2/H_2O flow passing over the particle.

On the other hand, the C7/AS/H_2O particles are showing nucleation-and-growth mechanism (example in Fig. 4.7b), spinodal decomposition, and

growth of a second phase at the surface of the particle (example in Fig. 4.7c) at mf_d(AS) of < 0.30, 0.30 to 0.60 and 0.6 to 1.0, respectively. These different phase separation mechanisms are indicated as different shadings in Fig. 4.4b.

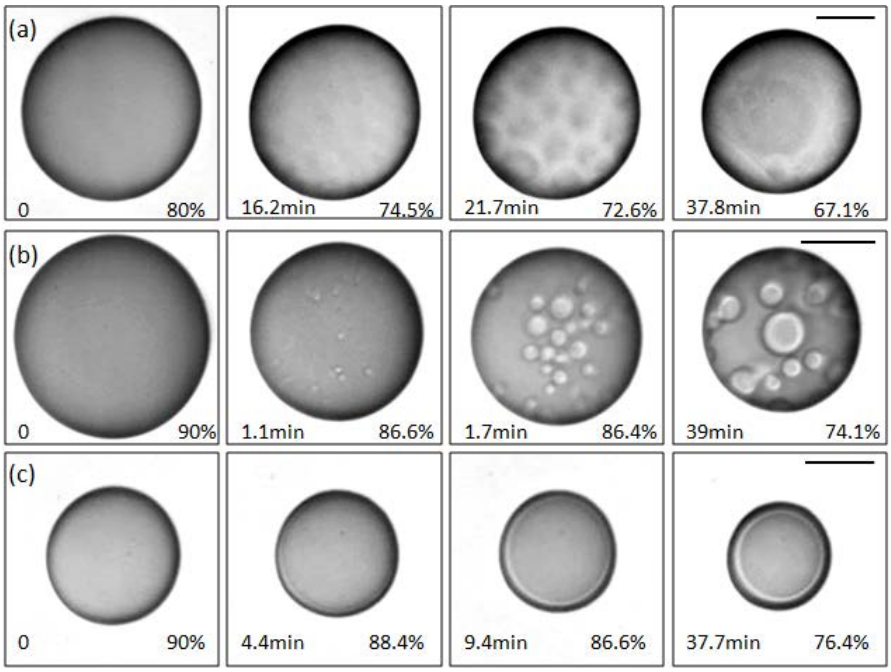

Figure 4.7 *Series of optical images for different LLPS mechanisms: (a) mechanism unclear (most probably growth and coalescence of organic lenses on the droplet surface) in a C6/AS/H_2O particle with OIR = 1:4, (b) nucleation-and-growth with subsequent coalescence in a C7/AS/H_2O particle with OIR = 6:1, and (c) growth of second phase from the particle surface in a C7/AS/H_2O particle with OIR = 1:6. The black bars represent 20 µm.*

4.4.5 Calculated phase diagrams

Thermodynamic model calculations for the three systems have been conducted to support the comparison and interpretation of the experimentally determined phase diagrams. While the measurements establish the phase diagrams in the RH vs. dry (water-free) composition space, a thermodynamic calculation reveals the compositions (including water content) of the two phases in liquid-liquid equilibrium (LLE).

On the basis of a mathematically much simpler computation of phase stabilities in case of only three thermodynamically independent components, the limit of stability between metastable and unstable one-phase states, the spinodal curves, were calculated only in case of the ternary systems (see Zuend et al., 2010). However, for reasons of similarity, further discussed below, the computed spinodal curves also support the interpretation of the phase stabilities in case of the C5/AS/H_2O, C6/AS/H_2O, and C7/AS/H_2O systems.

Figure 4.8 shows the computed phase diagrams for the different systems at room temperature. The model predicts a miscibility gap for all systems, the extent of which however differs in composition and RH range. In agreement with the experimental phase diagrams, the miscibility gap is largest in case of the C7/AS/H_2O system and becomes smaller with decreasing size of the dicarboxylic acids and increasing O:C, until it disappears completely. The mass fraction compositions of coexisting phases, as shown in the upper panels of Fig. 4.8, reveal that water is present in both phases in similar fractions, the difference being largest in case of the C7/AS/H_2O system, as seen from the slopes of the tie-lines. However, the difference in water contents is less pronounced when considered in terms of mole fractions since the difference in molar mass of the C5, C6, and C7 dicarboxylic acids explains a part of the apparent difference between panels (a), (b), and (c). The difference in terms of AS and organic fractions in coexisting phases is much more distinct. This implies that both the dicarboxylic acids and AS (dissociated into NH_4^+ and SO_4^{2-} ions in solution) are quite hydrophilic, but that interactions between the ions and the organics lead to a LLPS at higher AS mass fractions, when, at lower RH, the present fraction of water is not sufficient to moderate those interactions. Since mostly the interactions

between non-polar organic molecule segments, here the CH_2 and CH_3 groups, and ions are causing the phase separation, it is not surprising that the miscibility gap increases with a decrease in the O:C. The model also predicts that all three salt-free systems are miscible with water in all proportions.

While many features of the calculated phase diagrams agree with the droplet experiments at least qualitatively, there are also a number of differences, discussed in the following. Most strikingly, in contrast to the measurements, the model predicts a phase separation region in the C5/AS/H_2O. In principle, there could also be a phase separation region in the C5/AS/H_2O droplets in reality, but only present at RH below the ERH of the droplets and therefore outside of the experimentally accessible range. However, the model predicts the maximum onset RH of LLPS already at ~60 % (a_w = 0.6), see Fig. 4.8b. It is therefore obvious, that the predicted onset RH of LLPS is too high, in case of C5/AS/H_2O by at least 20 % RH. For an analogous ternary C4/AS/H_2O system containing succinic acid, the model still predicts a hypothetical LLPS (not shown), but only below the ERH of AS (< 40 % RH) and only for mf_d(AS) above 0.6. For a ternary C3/AS/H_2O system containing malonic acid, no LLPS is predicted in the entire composition space. Comparisons of predictions and measurements for the C6/AS/H_2O and C7/AS/H_2O systems, show that the model also predicts higher LLPS onset RH for these systems, with a difference (model – measurement) of ~8 % RH in case of C6/AS/H_2O and ~2 % RH in case of C7/AS/H_2O at OIR = 1:1. These differences are considerably smaller than in the case of the C5/AS/H_2O system. Regarding the group-contribution concept used within AIOMFAC to represent organic molecules and their interactions with other species/functional groups, it is not surprising that there are some differences between model predictions and measurements. As described in Zuend et al. (2011), the required AIOMFAC interaction parameters between ions and organic functional groups were determined based on a large, but unevenly distributed amount of experimental data, using a sophisticated parameter optimization procedure to obtain best simultaneous agreement between calculated and measured thermodynamic data. As it turns out, the parameterization database contains mainly water activity data for the optimization of interaction parameters between the NH_4^+ and SO_4^{2-} ions of

AS and the carboxyl group of dicarboxylic acids. Only three solid-liquid equilibria datasets and not a single LLE dataset have been available to better constrain these interactions with potential consequences for the prediction of LLPS. In view of this, the model predictions are in remarkably good agreement with the measured C7/AS/H_2O data. The larger deviations between model and measurements in case of the C5/AS/H_2O mixtures can also be understood as a result of less constrained AIOMFAC interaction coefficients towards high organic concentrations (and low water mass fractions).

The calculated and measured coexistence curves of the C6/AS/H_2O systems agree within ~8 % RH for mf_d(AS), from 0.3 to 0.9. Comparing the coexistence curve of the C6/AS/H_2O system at mf_d(AS) < 0.25 from Fig. 4.4a (measurements) with panel (e) of Fig. 4.8 shows that there is disagreement at those lower salt concentrations. While the model suggests a single mixed phase, the experimental data show that a phase separation is present, however, with rather unusual variations in the LLPS onset RH. For some experiments at compositions 0.19 < mf_d(AS) < 0.21 no LLPS was observed, which would be in agreement with the model results. Moreover, the mf_d(AS) measured by Raman spectroscopy in the organic-rich phase of C6/AS/H_2O phase separated systems agree with a miscibility gap that only extends to mf_d(AS) of ~ 0.3 (Fig. 4.6a). Furthermore, the measured variable AS concentration of the organic-rich phase for OIR = 4:1 and higher, suggests that we do not have a regular LLPS in this composition range. The reproducibly high onset and end of LLPS at RH = 85 % for mf_d(AS) = 0.095 might be considered as an indication that the minor phase has an almost fixed stoichiometry and might be highly structured. Also, additional ionic species might be important for the formation of this phase because at those lower AS mass fractions and higher water mass fractions, the dicarboxylic acids dissociate to a significant degree, yet concentration dependent and additional ionic species such as bisulfate ions (HSO_4^-) form, leading to a different mixture composition (than used in the model calculations). From Fig. 4.4b, it looks like a similar but less pronounced phase behavior could be present in the C7/AS/H_2O droplets at mf_d(AS) < 0.15.

The lower panels (c), (f), and (i) of Fig. 4.8 show model calculations for ternary mixtures containing glutaric acid, 2-methylglutaric acid, and 3,3-

dimethylglutaric acid, respectively, corresponding to the 5-component systems of the panels above them. The predicted phase separation regions of the ternary systems are highly similar to those of the corresponding 5-component systems. This result is expected, since the main difference between the 5-component systems and the ternary systems is the mixture of three similar dicarboxylic acids of equal mass, O:C and hydrogen-to-carbon atomic ratios (H:C), and the same kinds of functional groups, instead of only one dicarboxylic acid. Hence, the applied group-contribution approach of AIOMFAC can only lead to very small differences among the activity coefficients of structural isomers of dicarboxylic acids in aqueous AS solutions. Based on these phase diagram similarities and the underlying modeling reasons, it is also clear that the calculated spinodal curves of the ternary diagrams apply as well to the 5-component systems. The position and shape of the unstable one-phase region enclosed by the spinodal curve in panels (f) and (i) of Fig. 4.8, relative to the position of the coexistence curve (binodal), suggests that spinodal decomposition may occur in the C6/AS/H_2O system in the composition range of ~ 0.4 < mf_d(AS) < ~0.7, which is in good agreement with the observed mechanism in the experiments. At higher AS mass fractions, mf_d(AS) > ~0.7, a spinodal decomposition could still take place, but the a_w-difference between binodal and spinodal curves becomes larger, so that nucleation of a second phase already at a higher RH, before the spinodal curve is reached, becomes more likely. In case of the C7/AS/H_2O droplets, the model suggests that spinodal decomposition may occur in the mass fraction range ~0.11 < mf_d(AS) < ~0.55. As compared to the experiments, the predicted range is extended to lower mass fractions of AS; the experiments suggest a lower range limit of mf_d(AS) = ~ 0.3. The measured onset RH (89.7 %) for spinodal decomposition in C7/AS/H_2O droplets at OIR = 1:1 agrees well with the predicted spinodal curve (90 % RH) at this composition.

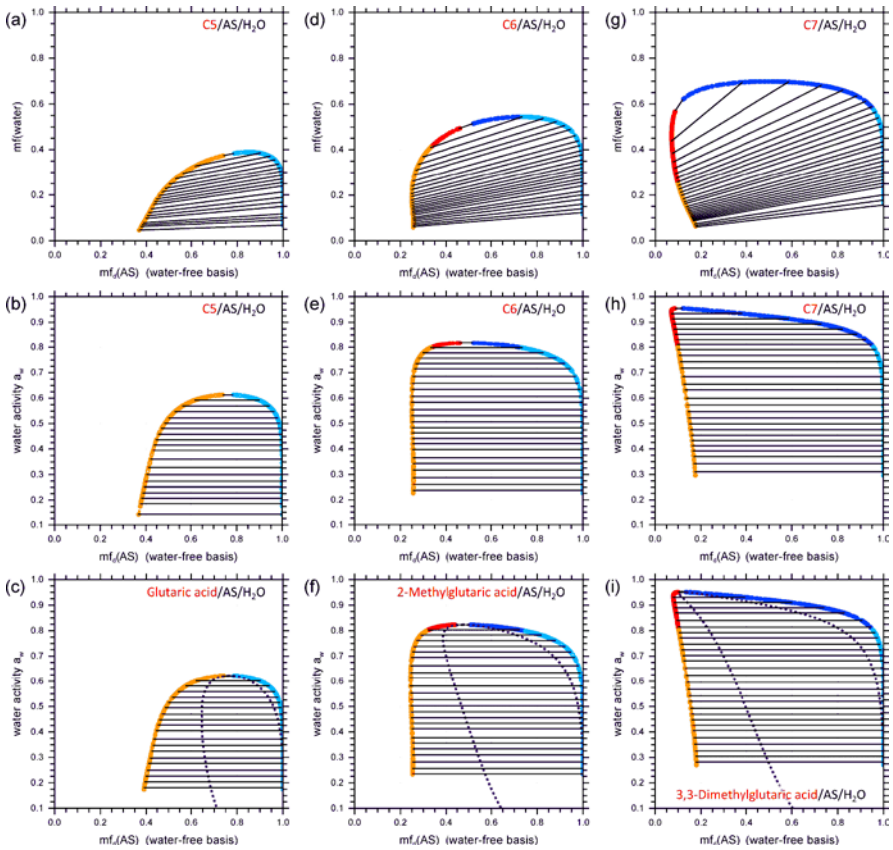

Figure 4.8 *Predicted phase diagrams of C5/AS/H_2O (left), C6/AS/H_2O (center), and C7/AS/H_2O (right) computed at 298 K using AIOMFAC. Top panels: liquid-liquid coexistence curve (colored) and tie-lines (black) given as water-free "dry" mass fraction of AS, mf_d(AS) vs. mass fraction of water, mf(water). Each tie-line connects the two coexisting equilibrium phase compositions. Center panels: same as top panels but mf(water) replaced by water activity (= RH when liquid and gas phase are in equilibrium). Bottom panels: same as center panels but for ternary systems. Dotted lines: spinodal curves. Coexistence curve colors: red and blue branches indicate aqueous organic-rich phase and aqueous AS-rich phase, respectively. Orange and light blue indicate supersaturation with respect to crystalline AS. The calculated coexistence curves are discontinued at low aw due to*

numerical stability issues at very high supersaturation of AS (AS would crystallize before reaching those conditions).

Figure 4.9 shows the computed Gibbs energy difference between a forced one-liquid-phase state of the mixture and the equilibrium state (two-liquid-phases state in the LLPS region) for the C6/AS/H_2O and C7/AS/H_2O systems at 298 K in the RH range from 100 % to 30 %. Close to the coexistence curve, the Gibbs energy difference ΔG is rather shallow but increases steeply at lower RH within the phase separation region. This indicates that metastable solutions can exist at water activities slightly below the coexistence curve so that the spinodal limit can be reached in experiments before a nucleation-and-growth event happens. The curvature of the ammonium sulfate solubility limit (the white dashed-dotted curve in Fig. 4.9) in both systems indicates AS deliquescence RH close to the value in the binary aqueous ammonium sulfate solution for the dry mass fraction range ~0.2 < mf_d(AS) ≤ 1.0. At higher organic contents, mf_d(AS) < ~0.2, the deliquescence RH drops sharply to lower values due to the reduced amount of AS in the mixture. These DRH predictions agree quite well with the measured AS DRH values shown in Fig. 4.4.

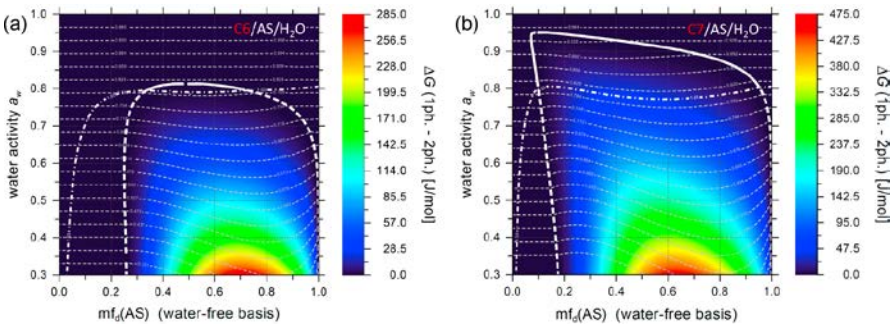

Figure 4.9 *Calculated Gibbs energy difference ΔG (color bar), between a hypothetical one-liquid-phase state (1ph.) and a two-liquid-phases state (2ph.) for (a) the C6/AS/H_2O and (b) the C7/AS/H_2O system at 298 K. The computed coexistence curves are shown in white (dashed where AS is*

supersaturated) and correspond to coexistence curves of panels (e) and (h) in Fig. 4.8. The solubility limit of AS (deliquescence onset) is shown as the white dashed-dotted curve. The light grey dashed lines are isolines of constant equilibrium-state water activity. They represent tie-lines within the LLPS region.

4.4.6 Possible morphologies of droplets on a hydrophobically coated substrate

The optical microscope gives only the top view of the droplets on the substrate. It is therefore not possible to directly observe whether inclusions of the minor phase have contact to the droplet/air or the droplet/substrate interface or whether they are floating within the droplet volume. To resolve this issue, we performed confocal Raman scans through the droplets by changing the laser focus from the bottom to the top of the droplets with step sizes of 6 - 7 µm. Figure 4.10 shows an example of such a vertical scan. Panel (a) gives the optical image of the droplet. The scan was performed through an inclusion with a diameter of ~19 µm (marked by a white arrow). For comparison, a Raman spectrum of the outer phase (marked by a black arrow) was also collected. Evaluation of the Raman spectra relied on the ratio of the peak height of the main peaks of AS (979 cm^{-1}) and C6 (2931 cm^{-1}). This AS/C6 peak ratio is shown in Fig. 4.10b as a function of laser focus within the droplet. We determined the bottom of the droplet (droplet height = 0 µm) optically as the point where the rim of the droplet appeared sharp and the diameter of the droplet was largest. Moving the focus upwards, the observed diameter decreased (gray arrows in (c)) and the droplet edge became increasingly blurred making the diameter measurement inaccurate. To determine the top of the droplet, we in addition reconstructed the droplet shape assuming a spherical cap with a contact angle of 81.6 ± 2° (determined for 2 µL C6/AS/H_2O droplets with OIR = 1:1 (≈ 40 wt % (C6 + AS)) deposited on the hydrophobically coated substrate (see panel (c)) leading to a droplet height of 25.4 µm for the investigated droplet with diameter of 58.9 µm. This droplet height is given as dashed gray line in (b). The highest AS/C6 Raman peak ratios were measured at droplet heights of 6 and 12 µm. Above 20 µm the AS/C6 peak ratio remained constant at a value

slightly above the one of the outer phase (given as a black triangle in (b)) while the absolute Raman intensities decreased because the laser focus was moving out of the droplet. This clearly shows that the inclusion was at the bottom of the droplet, probably with a high contact angle to the substrate (> 90 °) or forming almost a sphere. We performed similar experiments for two other droplets with smaller inclusions (~ 10 µm diameter), which clearly showed that these inclusions were also at the bottom of the droplet. This morphology is also supported by the calculation of the settling velocity of aqueous AS inclusions in the organic-rich phase: settling of 10 and 20 µm diameter AS-rich phase inclusions should occur at a rate of 0.5 - 3.3 and 2 - 13 µm min^{-1}, respectively. We therefore expect that the AS-rich inclusions settle to the bottom of the droplet driven by gravity within the timescale of the experiment (see Appendix A for details of the calculation).

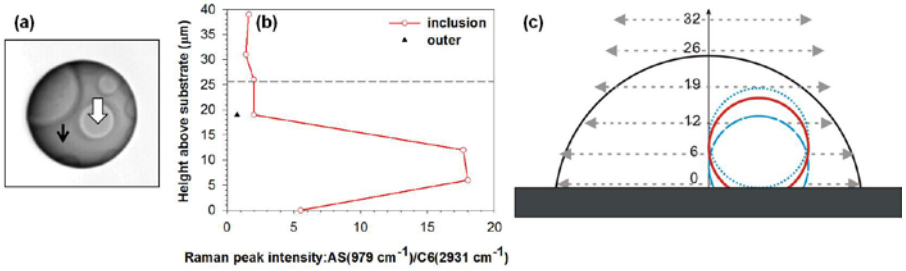

Figure 4.10 *Raman scan through a C6/AS/H_2O droplet with OIR = 1:1 on the hydrophobic coated substrate at 65 % RH. Panel (a): Optical image of the droplet (58.9 µm in diameter). The white arrow indicates the position of the Raman scan through the AS inclusion (~19.0 µm in diameter). Panel (b): Ratios of AS (979 cm-1) and C6 (2931 cm-1) Raman peak intensities. Red circles: vertical scan through the droplet at the position indicated by the white arrow in (a). Black triangle: reference point representing the AS/C6 Raman ratio of the outer phase measured at the position indicated by the black arrow in the (a). The gray dashed line sets the maximum height of the droplet (25.4 µm) as reconstructed in panel (c). Panel (c): Reconstructed side view of the droplet (black curved line) on the substrate and the*

inclusion (red) indicated by the white arrow in panel (a). In blue are shown inclusions with upper and lower limits of the estimated contact angle range from 105 to 140°. The horizontal gray arrows correspond to the particle diameter (µm) measured from the microscopic images at each scanning level of the droplet (red open circles in panel (b)).

In all investigated C6/AS/H_2O droplets with OIR = 1:1, the main AS inclusion moved from the middle to the edge of the droplet between ~70 - 66 % RH and remained in this partially engulfed configuration down to ERH. A similar behavior was observed for C6/AS/H_2O droplets between ~63 - 50 % RH with OIR = 1:2. Partial engulfed configurations were also observed for C7/AS/H_2O droplets ~88 % RH with OIR = 2:1.

The morphology of droplets with sizes of several tens of micrometers is influenced by surface and interfacial forces and by gravity. The spreading coefficient (Torza and Mason, 1970; Kwamena et al., 2010; Reid et al. 2011) can be used to predict the equilibrium morphology of two immiscible phases when in contact with each other. The spreading coefficient (S_i) of a liquid component (i) spreading over another component (j) can be determined when the surface (σ_{jk}, σ_{ik}) and interfacial tensions (σ_{ij}) are known:

$$S_i = \sigma_{jk} - (\sigma_{ij}+\sigma_{ik}). \quad (4.1)$$

For a partial engulfed configuration, the spreading coefficient of the organic-rich phase on the aqueous phase needs to be smaller than zero, which implies an interfacial tension between the two liquid phases of $\sigma_{org/AS} > \sigma_{AS} - \sigma_{org}$. Assuming an upper limit for the surface tension of the C6-rich phase of σ_{org} = 52 mN m^{-1} and a lower limit for the AS-rich phase of σ_{AS} = 67 mN m^{-1} (see Appendix B for estimates of surface and interfacial tensions), an interfacial tension of at least 15 mN m^{-1} is required for a partial engulfed configuration, which is in the typical range of interfacial tensions of aqueous/organic two-liquid-phases systems. It can be assumed that the interfacial tension increases with decreasing RH because water as mediating component between the phases becomes more and more scarce. Between 70 - 66 % RH the interfacial tension seems to reach a critical value where the

spreading coefficient of the C6-rich phase changes sign from a positive to a negative value making a partially engulfed configuration energetically more favorable.

Using Young's equation, the contact angle of the aqueous AS inclusion with the substrate can be estimated (see Appendix B), leading to values in the range of 105° - 140°. Droplets with these lower and upper values are sketched in blue in Fig. 4.10c, the best estimation of the droplet's morphology is given in red.

4.4.7 Atmospheric implications

Recently, O:C has been stressed as crucial parameter to describe hygroscopicity (Jimenez et al., 2009), oxidation (Heald et al., 2010; Kroll et al., 2011), volatility and mixing thermodynamics of organic aerosol (Donahue et al., 2011). O:C and H:C of ambient and laboratory aerosol particles can be derived from analysis of high resolution mass spectral data (Aiken et al., 2007; Aiken et al., 2008). Heald et al. (2010) established that atmospheric organic aerosols, obtained from various field measurements and laboratory studies, cluster along a narrow line with a slope of -1 in Van Krevelen space (H:C vs. O:C). O:C can also be an indicator of phase separation of mixed particles.

Figure 4.11 gives the position of the organic components of hydroxyl and PEG-400/AS/H_2O (blue) and aromatic or aliphatic carboxylic acid/AS/H_2O systems (red) from literature (see Table 4.2) in the Van Krevelen diagram. The C5/AS/H_2O, C6/AS/H_2O and C7/AS/H_2O systems from this study are also included (orange symbols). It can be seen that systems with O:C < 0.7 show LLPS (circles) while systems with O:C > 0.7 do not (triangles). This is in perfect agreement with Bertram et al. (2011) who reported in a recent study that O:C is a critical factor for LLPS of aerosol particles and showed that there is no phase separation for O:C > 0.7 for various single organic compounds in the presence of AS. Therefore, we expect that in the troposphere LLPS occurs in mixtures of AS and organic components with an O:C < 0.7. Analysis of ambient data indicates O:C up to 0.6 for semivolatile oxygenated organic aerosols (SV-OOA) and from 0.5 - 1.1 for

low volatility OOA (LV-OOA) (Ng et al., 2011). All of the SV-OOA and a part of the LV-OOA, therefore, fall into the O:C range for which we expect LLPS. The degree of oxidation that chamber organic aerosol reach strongly depend on the volatile organic precursor molecules: secondary organic aerosol (SOA) formed by oxidation of α-pinene, isoprene, m-xylene and toluene mostly exhibit O:C < 0.7 while e.g. acrolein and glyoxal SOA cover O:C > 0.7 (Chhabra et al., 2011). In addition, LLPS might promote the formation of particles with highly viscous and glassy coatings because the more viscous organic components are spatially separated from the less viscous inorganic salt solution.

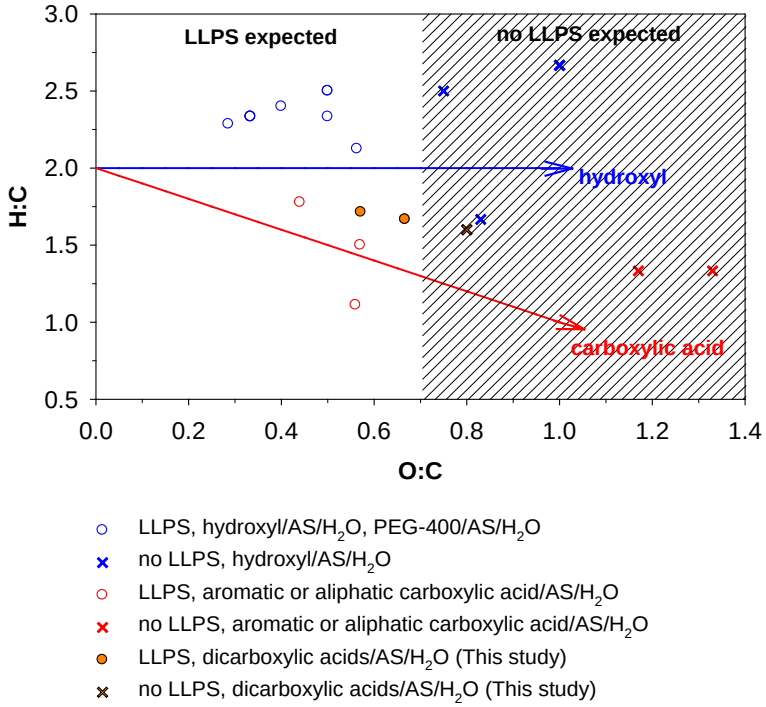

Figure 4.11 *Van Krevelen diagram showing organic/AS/H_2O systems with LLPS (circles) and without LLPS (triangles) from previous work (Marcolli and Krieger, 2006; Zuend et al., 2008; Ciobanu et al., 2009; Bertram et al., 2011, see Table 4.2 for the datasets) and this study (orange symbols). The*

blue and red arrows correspond to the addition of hydroxyl and carboxylic acid (or hydroxyl + ketone/aldehyde) functional groups to an alkane backbone, respectively, as discussed in Heald et al. (2010).

Table 4.2 *List of "no LLPS" and "LLPS" exhibiting mixtures consisting of aqueous AS with organic components containing hydroxyl (OH), carboxyl (COOH), ether (CH_nO), ester (CCOO), and aromatic (ACH_n) functional groups. Range of experimental conditions: 30 % < RH < 100 % and mf_d(AS) > 0.1. Data from the literature and this work.*

Compounds	Formula	Functional Groups	O:C	H:C	References
no LLPS					
glycerol	$C_3H_8O_3$	OH	1.00	2.67	Marcolli and Krieger (2006), Bertram et al. (2011)
1,2,4-butanetriol	$C_4H_{10}O_3$	OH	0.75	2.50	Zuend et al. (2008)
6,8-dioxabicyclo[3.2.1]octane-2,3,4-triol	$C_6H_{10}O_5$	CH_nO, OH	0.83	1.67	Bertram et al. (2011)
pentanedioic acid	$C_5H_8O_4$	COOH	0.80	1.60	Bertram et al. (2011)
citric acid	$C_6H_8O_7$	COOH, OH	1.17	1.33	Bertram et al. (2011)
propanedioic acid	$C_3H_4O_4$	COOH	1.33	1.33	Bertram et al. (2011)
C5: glutaric acid + dimethylmalonic acid + methylsuccinic acid	$C_5H_8O_4$	COOH	0.80	1.60	This work
LLPS					
1,2-hexanediol	$C_6H_{14}O_2$	OH	0.33	2.33	Marcolli and Krieger (2006)
1,4-butanediol	$C_4H_{10}O_2$	OH	0.50	2.50	Marcolli and Krieger (2006)
1,2,6-hexane-triol	$C_6H_{14}O_3$	OH	0.50	2.33	Bertram et al. (2011)
2,4-pentanediol	$C_5H_{12}O_2$	OH	0.40	2.40	Zuend et al. (2008)
2,5-hexanediol	$C_6H_{14}O_2$	OH	0.33	2.33	Zuend et al. (2008)
1,7-heptanediol	$C_7H_{16}O_2$	OH	0.29	2.29	Zuend et al. (2008)
monomethyloctane-1,8-dioate	$C_9H_{16}O_4$	COOH, CCOO	0.44	1.78	Bertram et al. (2011)

4-dihydroxy-3-methoxybenzeneacetic acid	$C_9H_{10}O_5$	COOH, OH, CH_nO, ACH_n	0.56	1.11	Bertram et al. (2011)
2,5-dihydroxybenzoic acid	$C_7H_6O_4$	COOH, OH, ACH_n	0.57	1.50	Bertram et al. (2011)
2,2-dimethylbutanedioic acid	$C_6H_{10}O_4$	COOH, OH	0.67	1.67	Bertram et al. (2011)
PEG-400	$C_{2n}H_{4n+2}O_{n+1}$, (n=8-9)	OH, CH_nO	0.56	2.12	Ciobanu et al. (2009)
C6: 2-methylglutaric acid + 3-methylglutaric acid + 2,2-dimethylsuccinic acid	$C_6H_{10}O_4$	COOH	0.67	1.67	This work
C7: 3-methyladipic acid + 3,3-dimethylglutaric acid + diethylmalonic acid	$C_7H_{12}O_4$	COOH	0.57	1.71	This work

In this study, partially engulfed configuration was observed in the C6/AS/H_2O system for OIR = 1:1 and 1:2 while both partial (OIR = 2:1) and complete engulfed (OIR = 1:1) configurations occurred in the C7/AS/H_2O system. No size dependence of the morphology was observed for particles within the investigated size ranges. Due to the Kelvin effect, more complex morphologies are thermodynamically not favored in accumulation mode particles. Based on this and other recent studies (Ciobanu et al., 2009; Kwamena et al., 2010; Bertram et al., 2011; Reid et al., 2011), core-shell and partially engulfed configurations seem to occur. A core-shell configuration will have more drastic consequences for heterogeneous chemistry and hygroscopicity than a partially engulfed configuration because the aqueous inorganic-rich phase will be totally enclosed by a probably highly viscous organic coating with low diffusivity for reactants and water. E.g., atmospheric chemistry related to the N_2O_5 heterogeneous hydrolysis onto organic coated aerosol particles is strongly influenced by particle morphology (Thornton and Abbatt, 2005; Anttila et al., 2006; Cosman and Bertram, 2008; Cosman et al., 2008). Significant reduction in reactive uptake coefficient with a factor of 2 - 42 has been observed with dependence on organic components on aqueous sulfuric acid solutions. Assuming that the aqueous AS phase is surrounded by the organic-rich phase, the N_2O_5 hydrolysis may be suppressed effectively.

4.5 Conclusions

We investigated phase transitions of micrometer-sized particles consisting of multicomponent mixtures of AS and C5, C6, and C7 dicarboxylic acids having O:C of 0.80, 0.67, and 0.57, respectively, during humidity cycles. We used optical microscopy to follow phase changes and Raman spectroscopy to infer chemical composition. Micrometer-sized particles of C5/AS/H_2O, C6/AS/H_2O, and C7/AS/H_2O showed significantly different phase transition behavior during RH cycles. While the C5/AS/H_2O particles showed no LLPS with OIR = 2:1, 1:1, and 1:4, the C6/AS/H_2O and C7/AS/H_2O particles exhibit LLPS upon drying at RH between 50 and 85 % and at ~ 90 %, respectively, depending on the OIR. Phase equilibria calculations using AIOMFAC are for the most part in good agreement with

the experimentally determined phase diagrams. From the investigated systems and literature data, we suggest that LLPS commonly occurs in atmospheric aerosol particles with O:C < 0.7. This is in excellent agreement with a very recent study by Bertram et al. (2011). Further investigations have to show how sensitive this limit is to the specific chemical composition of the organic and inorganic aerosol fractions, temperature, and the complexity of the organic fraction in aerosols.

Core-shell structure and partially engulfed configurations were observed in the particles on a hydrophobically coated substrate and therefore such morphologies might very likely be present in the troposphere. A core-shell configuration will have consequences for heterogeneous chemistry and hygroscopicity because the aqueous inorganic-rich phase will be totally enclosed by a probably highly viscous organic coating with low diffusivity for reactants and water. Definitive conclusions whether a core-shell or a partially engulfed morphology is prevalent in airborne particles is not possible from the present study because all experiments have been performed on a hydrophobically coated substrate, which might influence surface forces and the preferred morphology. Supplementary experiments should therefore be carried out on levitated particles in an electrodynamic balance or optical tweezers. Since also levitated particles are subject to additional forces that are not present in atmospheric aerosols, these measurements should be complemented by calculations of the preferred morphology using accurate surface and interfacial tension data of the investigated mixtures.

4.6 Acknowledgements

This work was supported by the Swiss National Foundation Project No. 200020-125151 and the Competence Center Environment and Sustainability of the ETH Domain (CCES) project IMBALANCE. We thank Uwe Weers and Edwin Hausammann for technical support.

4.7 Appendix A: Settling velocity

The settling velocity (ν) of an AS-rich inclusion within a C6-rich fluid is given by Stokes' law:

$$\nu = \frac{2(\rho_i - \rho_f)gr^2}{9\mu} \quad \text{(A1)}$$

where ρ_i and ρ_f are the densities of the inclusion and the fluid, respectively, g the gravitational acceleration, r the radius of the inclusion and μ the viscosity of the fluid. At a_w = 0.7, AS solution density is calculated as 1.30 g cm^{-3} at 20 °C using the parameterization by Tang and Munkelwitz (1994). We estimate the density of the C6-rich phase at a_w = 0.7 and 20 °C as 1.20 - 1.23 g cm^{-3} by extrapolating the densities of solutions of the structurally similar glutaric acid (Ben-Hamo et al., 2007) to estimated solute mass fractions of 0.75 – 0.80 at a_w = 0.7. Hence, we expect the aqueous AS phase to be of higher density than the organic-rich one.

The viscosity of aqueous adipic acid, the straight-chain C6 dicarboxylic acid, has only been measured for dilute solutions (Chmielewska and Bald, 2008). In the range where data is available, densities of aqueous solutions of adipic, glutaric, and citric acid show all similar concentration dependences (Laguerie et al., 1976; Chmielewska and Bald, 2008). To estimate the viscosity of the C6-rich phase, we therefore extrapolate the citric acid values to concentrations corresponding to solute mass fractions of 0.75 - 0.80, yielding viscosities of 100 - 500 mPa s. Applying these values, settling of 10 and 20 μm diameter AS-rich phase inclusions should occur at a rate of 0.5 - 3.3 and 2 - 13 μm min^{-1}, respectively. We therefore expect that the AS-rich inclusions settle to the bottom of the droplet driven by gravity within the timescale of the experiment, which is in accordance with the observed morphology of the Raman scans.

4.8 Appendix B: Estimation of surface and interfacial tensions

Surface tensions of aqueous solutions of the straight chain dicarboxylic acids have been measured by several groups (e.g. Shulman et al., 1996; Varga et al., 2007). A decrease of surface tension is observed with increasing solute concentration. For 1 - 2 wt % aqueous adipic acid (C6) solutions surface tensions of ~68 mN m^{-1} (pure water case: ~72 mN m^{-1}) and for 30 - 40 % aqueous glutaric acid (C5) solutions a reduction of 10 - 20 % has been reported (Shulman et al., 1996; Varga et al., 2007; Booth et al., 2009). Topping et al. (2007) give values for adipic acid surface tension in the supercooled liquid state of 45.5 mN m^{-1} and 52.4 mN m^{-1} depending on estimation method. The organic-rich phase in C6/AS/H_2O droplets is highly concentrated and we expect it to exhibit similar surface tensions as the supercooled liquid state of adipic acid, i.e. 45 - 52 mN m^{-1}. Surface tension in AS solutions is increased by 20 % at AS saturation (a_w = 0.8 at 25 °C) compared with pure water and is expected to increase even more in the supersaturated regime (Lewis, 2006). However, in the presence of small amounts of adipic acid (~ 0.5 wt %), this trend is reversed and surface tension decreases with increasing AS concentration (Booth et al., 2009). A solution containing 0.0007 mole fraction adipic acid and 0.009 mole fraction AS exhibited a surface tension of 67.1 mN m^{-1}. This value might quite well represent the surface tension of the AS-rich phase in the C6/AS/H_2O droplets.

Interfacial tensions of binary aqueous/organic two-phase systems typically vary between 6 - 52 mN m^{-1} (Backes et al., 1990). On the other hand, aqueous two-phase systems consisting of immiscible aqueous phases of incompatible polymers, surfactants or salts exhibit very low interfacial tensions (< 1 mN m^{-1}) (Giraldo-Zuniga et al., 2006; Nan et al., 2006; Spyropoulos et al., 2008).

Young's equation relates the interfacial forces (σ) to the contact angle (θ) that a droplet (d) in a fluid (f) makes with the surface (s):

$$\sigma_{s/d} + \sigma_{d/f} \cos\theta = \sigma_{s/f} \qquad \text{(A2)}$$

The fluid (f) is usually, but not necessarily, the vapor phase. Using this relation, the contact angle of the minor-phase inclusions on the substrate can

be roughly estimated. In a first step, the interfacial tensions between the substrate and the C6-rich phase $\sigma_{org/s}$ and the substrate and the AS-rich phase $\sigma_{AS/s}$ can be estimated using the following values for the surface tensions of the substrate σ_s = 25.3 mN m^{-1} (Frank and Belfort, 2001), the C6-rich phase σ_{org} = 45 - 52 mN m^{-1}, and the AS-rich phase σ_{AS} = 67.1 mN m^{-1}, and contact angles for saturated C6 and 40 wt % AS droplets of 76.7 ± 2.8 ° and 94.0 ± 1.1 °, respectively. This yields $\sigma_{org/s}$ = 17.7 ° – 18.7 ° and $\sigma_{AS/s}$ = 25.3 °. Using these numbers and lower and upper limits of interfacial tension $\sigma_{org/AS}$ of 15 and 44 mN m^{-1}, respectively, yields contact angles of 105 ° - 140 °.

Chapter 5

Liquid-liquid phase separation in aerosol particles: dependence on O:C, organic functionalities, and compositional complexity

This chapter is a reproduction of the article published in the *Geophysical Research Letters*:

Song, M., Marcolli, C., Krieger, U. K., Zuend, A., and Peter, T.: Liquid-liquid phase separation in aerosol particles: dependence on O:C, organic functionalities, and compositional complexity, Geophys. Res. Lett., 39, L19801, doi:10.1029/2012GL052807, 2012.

The layout of the article including the tables and figures has been revised to match with this thesis structure.

5.1 Abstract

Atmospheric aerosol particles may undergo liquid-liquid phase separation (LLPS) when exposed to varying relative humidity. In this study we investigated the occurrence of LLPS for mixtures consisting of up to ten organic compounds, ammonium sulfate, and water in relationship with the organic oxygen-to-carbon (O:C) ratio. LLPS always occurred for O:C < 0.56, never occurred for O:C > 0.80, and depended on the specific types and compositions of organic functional groups in the regime 0.56 < O:C < 0.80. In the intermediate regime, mixtures with a high share of aromatic compounds shifted the limit of occurrence of LLPS to lower O:C ratios. The number of mixture components and the spread of the O:C range did not notably influence the conditions for LLPS to occur. Since in ambient aerosols O:C range typically between 0.2 and 1.0, LLPS is expected to be a common feature of tropospheric aerosols.

5.2 Introduction

Tropospheric aerosol particles consisting of inorganic salts and organic compounds undergo phase transitions such as deliquescence and efflorescence as a consequence of changes in ambient relative humidity (RH) (Martin, 2000; Marcolli and Krieger, 2006; Martin et al., 2008). In addition, non-ideal interactions between dissolved inorganic ions, water, and organic compounds may lead to liquid-liquid phase separation (LLPS) (Marcolli and Krieger, 2006; Ciobanu et al., 2009; Zuend et al., 2010; Bertram et al., 2011; Song et al., 2012a; Zuend and Seinfeld, 2012). The physical state and the hygroscopicity of aerosol particles need to be considered for an accurate quantification of atmospheric and climate effects because they influence gas-particle partitioning of semivolatile compounds (e.g. Zuend et al., 2010; Zuend and Seinfeld, 2012), heterogeneous chemistry (e.g. Anttila et al., 2007; Cosman et al., 2008) and the scattering and absorption of light (e.g. Martin et al., 2004). The presence or absence of LLPS in aqueous mixtures can be determined in laboratory experiments with model mixtures representing tropospheric aerosols (e.g. Marcolli and Krieger, 2006;

Bertram et al., 2011; Song et al., 2012a) or computed using a liquid-liquid equilibrium model (Zuend et al., 2010; Zuend and Seinfeld, 2012).

While ammonium sulfate (AS) is a main constituent of aerosol particles and well suited to represent the inorganic aerosol fraction in model mixtures, selecting appropriate surrogates for the organic fraction is more complex. The fractions of organics (18 - 70 %), sulfate (10 - 67 %) and ammonium (6.9 - 19 %) have been measured by aerosol mass spectrometry at various locations (Zhang et al., 2007). The organic aerosol fraction typically consists of up to thousands of different compounds and their characterization and quantification is a task that challenges common analytical techniques. Typically only 10 – 20 % of the organic aerosol fraction can be identified on the level of individual substances using gas and liquid chromatography of filter extracts (Decesari et al., 2006; Hallquist et al., 2009). With this approach, classes representing the organic aerosol have been identified. These comprise oxidized aliphatic substances such as mono- or multifunctional carboxylic acids, alcohols, polyols, sugars, and oxidized aromatic substances such as aromatic acids and aldehydes. Alternative methods are needed to gain a more quantitative overview of organic functionalities. Functional group analysis by proton NMR spectroscopy has identified aliphatic groups bound to an unsaturated carbon, alkoxyl, acetal, alkylic, and aromatic groups as main functionalities representing the organic aerosol fraction (Decesari et al., 2006). FTIR spectroscopy is able to quantify alcohol, aromatic, aliphatic unsaturated, carbonyl, carboxylic acid, and amine groups (Gilardoni et al., 2009). An even more general characterization of organic aerosols based on their degree of oxidation is achieved by high-resolution mass spectrometry that allows quantifying O:C and H:C ratios (e.g. Heald et al., 2010; Ng et al., 2010). Typical values of organic O:C in ambient samples range from 0.2 to 1.0 (Heald et al., 2010; Takahama et al., 2011). Recent studies on a limited number of model systems have shown that LLPS in mixed organic/AS/H_2O particles commonly occurs for O:C < 0.7 (Bertram et al., 2011; Song et al., 2012a). Hence, the O:C ratio of the organic aerosol fraction may be a good predictor for the presence of LLPS in tropospheric aerosol particles because it reflects the polarity of organic compounds and their miscibility with water and

electrolytes. However, the investigated systems so far are small in number and most of them represent the organic fraction by one substance only. To determine whether the O:C ratio is indeed an accurate LLPS predictor for more realistic representations of the organic/inorganic aerosol, the following questions are addressed in this study: (i) Does in addition to the O:C ratio also the specific functional group composition influence the occurrence of LLPS? (ii) Does the number of components influence the occurrence of LLPS in organic/AS/H_2O mixtures? (iii) Does the spread of O:C ratios of the individual organic components present in a mixture influence the occurrence of LLPS? To answer these questions, we investigated the presence or absence of LLPS in model systems of aerosol particles, consisting of various organic components, AS, and water.

5.3 Experimental methods

Experiments were performed on droplets (20 - 65 μm in diameter) at 293 K using an optical microscope equipped with a temperature- and humidity-controlled flow-cell. The detailed experimental procedure is given in the Supplementary Material (see also Song et al., 2012a). All the compounds were purchased from Sigma-Aldrich with purities ≥ 98 % and used without further purification. We mixed the organic fraction together with AS at organic-to-inorganic dry mass ratios OIR = 2:1, 1:2, 1:6. With these mixtures, we performed humidity cycles to scan the phase diagram for miscibility gaps.

5.4 Results and discussion

In Table 5.1, we define different sets of components, which constitute the organic fraction of the investigated model mixtures. Mixtures O:C ratios given in the third and fourth column of Table 5.1 were obtained by varying dry mass fractions of the organic components (mf_d(org)) in a range from 0 – 50 wt%. The exact composition of all investigated mixtures together with their O:C ratio and information on whether they exhibit LLPS or not is listed in Tables S1 – S7 of the Supplementary Material. The van Krevelen diagrams given in Fig. 5.1 display the occurrence of LLPS in relation to the

O:C and H:C ratios of the mixtures. In the cases where only one or two of the investigated OIR led to a LLPS, as shown in Fig. 5.2a, LLPS was most persistent for OIR = 1:2. Figure 5.2b gives in addition the average onset RH of LLPS (SRH) over all investigated OIR as a function of O:C. In the following Sects. we discuss in detail the aspects (i)-(iii) outlined in the introduction based on the Figs. and Table 5.1.

Table 5.1 *Organic components of the investigated organic mixtures, together with the O:C ratios of the mixtures with LLPS and without LLPS. "-" = no experiment performed. Note that not all individual mixtures contain all components. O:C ratios of mixtures are obtained by varying dry mass fractions of the components in a range from 0 – 50 wt%. The individual mixture compositions with O:C and H:C ratios are given in the Supplementary Material, Tables S1-S7.*

Mixture name	Organic components (with O:C in brackets)	O:C ratios of mixtures	
		with LLPS	without LLPS
Polyol	sorbitol (1.00); 1,2,7,8-octanetetrol (0.50)	0.71	0.76
Dicarboxylic acids (DCA)	glutaric acid (0.80); methylsuccinic acid (0.80); dimethylmalonic acid (0.80); 2-methylglutaric acid (0.67); 3-methylglutaric acid (0.67); 2,2-dimethylsuccinic acid (0.67); 3-methyladipic acid (0.57); 3,3-dimethylglutaric acid (0.57); diethylmalonic acid (0.57)	0.57, 0.67	0.80
Oxidized aromatic compounds (OAC)	2,5-dihydroxybenzoic acid (0.57); 3,5-dihydroxybenzoic acid (0.57); 2,4,5-trimethoxybenzoic acid (0.50)	0.55	0.57
Multifunctional compounds	maleic acid (1.00); dehydroacetic acid (0.50); kojic acid (0.67); 3,4-dihydroxy-2,2-dimethyl-4-oxo-2H-pyran-6-	0.67, 0.79	0.85

(MFC)	carboxylic acid (0.50); itaconic acid (0.80); 2-oxoglutaric acid (1.00)		
Polyol+DCA	diethylmalonic acid (0.57); levoglucosan (0.83); glutaric acid (0.80); sorbitol (1.00); 1,2,7,8-octanetetrol (0.50); 2-methylglutaric acid (0.67)	0.72, 0.76	-
OAC+DCA	3-hydroxybenzoic acid (0.43); 4-hydroxybenzoic acid (0.43); 2,5-dihydroxybenzoic acid (0.57); 2,6-dihydroxybenzoic acid (0.57); 3,4-dihydroxybenzoic acid (0.57); 3,5-dihydroxybenzoic acid (0.57); malonic acid (1.33); malic acid (1.25); 2-methylglutaric acid (0.67); diethylmalonic acid (0.57)	-	0.56, 0.61, 0.68
Complex organic mixture (COM)	2-methylglutaric acid (0.67); methylmalonic acid (1.00); malonic acid (1.33); glutaric acid (0.80); 3-methyladipic acid (0.57); diethylmalonic acid (0.57); malic acid (1.25); levoglucosan (0.83); pinonic acid (0.30); pinolic acid (0.30); 3-hydroxybenzoic acid (0.43); 3,5-dihydroxybenzoic acid (0.57); 1,2,7,8-octanetetrol (0.50)	0.63, 0.68, 0.70	0.77
Carminic acid	Carminic acid (0.59)	0.59	-
Tannic acid	Tannic acid (0.61)	-	0.61

5.4.1 Dependence of LLPS on organic functional groups

Figure 5.1a shows the occurrence range of LLPS for organics/AS/H_2O droplets covering the same O:C ratios but consisting of different organic functional groups. The functional group composition also influences the hydrogen-to-carbon (H:C) ratio. H:C is higher for open chain hydrocarbons and alcohols, and lower for molecules with ring structures and carbon-carbon or carbon-oxygen double bonds. In Fig. 5.1a various mixtures are compared, comprising hydroxyl functionalities (Polyol/AS/H_2O, cyan), dicarboxylic acids containing 5 (C5), 6 (C6) or 7 (C7) carbon atoms

(DCA/AS/H_2O, green; DCA(C5+C6+C7)/AS/H_2O, yellow), oxidized aromatic compounds (OAC/AS/H_2O, pink) and a mixture with multifunctional compounds including ring structures and double bonds (MFC/AS/H_2O, gray). The components of the mixtures are plotted as differently colored triangles. The range of observed LLPS (circles) and no LLPS (stars) is very similar for the Polyol/AS/H_2O and DCA/AS/H_2O mixtures. It slightly shifts to higher O:C for MFC/AS/H_2O, but significantly shifts to lower O:C for OAC/AS/H_2O. The comparison with MFC/AS/H_2O indicates that differences in H:C are hardly responsible for the behavior of OAC/AS/H_2O, rather the high share of aromatic rings. This is confirmed by results of additional mixtures investigated in this study and shown in Fig. 5.1c. The occurrence range of LLPS for polyols and dicarboxylic acids (Polyol+DCA/AS/H_2O) mixtures are in line with the results of Polyol/AS/H_2O and DCA/AS/H_2O whereas the occurrence range of LLPS of mixtures with oxidized aromatic compounds and dicarboxylic acids (OAC+DCA/AS/H_2O) are shifted to lower O:C. Carminic acid and tannic acid are high molecular weight compounds of 492.4 g mol^{-1} and 1701.2 g mol^{-1}, respectively, both containing aromatic ring structures. They may represent high molecular weight organic molecules as are found in humic like substances (HULIS) (Graber and Rudich, 2006). Carminic acid (O:C = 0.59) showed LLPS in mixtures with AS while tannic acid (O:C = 0.61) did not, again confirming that high shares of aromatic rings shift the LLPS occurrence range to lower O:C. We attribute this shift to lower O:C of the occurrence range of LLPS in systems with high shares of aromatic rings to a smaller salting-out effect of AS for aromatic than for aliphatic systems, possibly due to cation–π interactions between the ammonium ion and the aromatic rings (e.g. Ma and Dougherty, 1997).

It can be seen from Fig. 5.2a that LLPS of systems with high SRH extend over all investigated OIR. This is consistent with miscibility gaps observed for PEG-400/AS/H_2O (O:C ≈ 0.56) and C7/AS/H_2O (O:C = 0.57) with SRH ~ 90 %, which extend over a broad composition range starting from mf_d(AS) < 0.05 and ending at mf_d(AS) > 0.95 (Ciobanu et al., 2009; Song et al., 2012a). For systems with lower SRH, the miscibility gap is most persistent for OIR = 1:2 and disappears when the organic fraction is high. Fig. 5.2b presents O:C versus SRH of all mixtures studied in this work (filled circles,

average of all OIR that showed LLPS) and literature (open circles) (Marcolli and Krieger, 2006; Ciobanu et al., 2009; Bertram et al., 2011; Song et al., 2012a). Mixtures which did not exhibit a miscibility gap are indicated by a star at 0 % RH. SRH decreases with increasing O:C. The lowest SRH was observed at 59.0 % in the MFC/AS/H_2O system for O:C = 0.79. Note that observation of LLPS is limited to the RH range above efflorescence, which typically occurred between 40 and 50 % RH for the systems investigated in this study. Fig. 5.2b also presents a second-order polynomial proposed by Bertram et al., (2011) (black line) and a three-parameter sigmoid curve fit of all available data to parameterize SRH (red line) as a function of O:C. The sigmoid curve parameterization avoids unphysical SRH values for both low and high O:C ratios. At O:C ratios higher than 0.8, AS effloresces before LLPS is expected to occur. Therefore, in the O:C range > 0.8, the sigmoid curve represents our expectation of the occurrence range of LLPS if AS efflorescence would be suppressed (i.e. an extrapolation, dashed curve parts). In comparison to our data, the data and the polynomial proposed by Bertram et al. (2011) shows a bias to low SRH. The direct comparison of SRH of the system 2,5-dihydroxybenzoic acid/AS/H_2O from this study (68.5 % RH, OIR = 1:2) with Bertram et al., (2011) (average: 61.9 % RH) shows a difference of ~7 % RH. With the same O:C ratio, the SRH of 2,6-dihydroxybenzoic acid/AS/H_2O from this study presents at 91.5 % RH. The parameterization of the sigmoid curve from all data is given in the Supplementary Material.

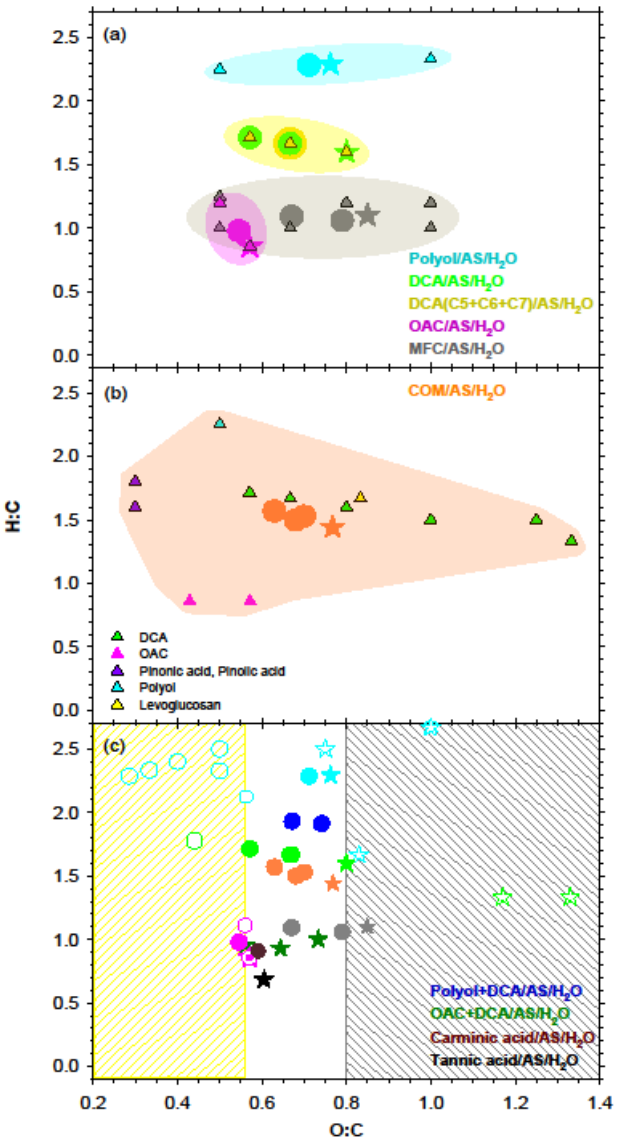

Figure 5.1 *Van Krevelen diagram showing organic/AS/H_2O systems with LLPS (circles) and without LLPS (stars) for OIR = 2:1, 1:1, 1:2 and 1:6. Triangles: Components of organic mixtures. (a) Mixtures of AS and*

organics with specific functionalities, namely: Polyol/AS/H_2O (cyan), carboxylic acids DCA/AS/H_2O including C5/AS/H_2O, C6/AS/H_2O, C7/AS/H_2O (all green) and (C5+C6+C7)/AS/H_2O (yellow), oxidized aromatic compounds OAC/AS/H_2O (pink), and multifunctional compounds MFC/AS/H_2O (gray). (b) Complex organic mixture COM/AS/H_2O (orange) with COM consisting of the following components (triangles): DCA (green), OAC (pink), pinonic and pinolic acid (purple), polyols (cyan) and levoglucosan (yellow). Colored regions in (a) and (b) indicate the O:C and H:C ranges covered by the individual organic components for each model system. (c) Collection of all investigated systems from this study (filled symbols) including those shown in (a) and (b) and from the literature (open symbols). Additional systems from this study: Polyol+DCA/AS/H_2O (blue), OAC+DCA/AS/H_2O (dark green), carminic acid/AS/H_2O (brown), and tannic acid/AS/H_2O (black). Systems from the literature: polyol/AS/H_2O (cyan, (Marcolli and Krieger, 2006; Zuend et al., 2008; Ciobanu et al., 2009; Bertram et al., 2011)), DCA/AS/H_2O (green, (Bertram et al., 2011; Song et al., 2012a)), OAC/AS/H_2O (pink, (Bertram et al., 2011)). Yellow-hatched region: LLPS observed in all investigated systems; gray-hatched region: no LLPS detected in any of the investigated systems.

5.4.2 Dependence of LLPS on compositional complexity

Most previous studies on LLPS in organic/AS/H_2O have been performed with a single organic substance representing the organic aerosol fraction (e.g., Ciobanu et al., 2009; Bertram et al., 2011). Here we investigate the influence of the compositional complexity of the organic aerosol fraction on the occurrence of LLPS by comparison of mixtures with similar O:C ratios but different number of components and different spread of O:C ratios of the components.

The most complex mixture investigated is COM/AS/H_2O consisting of 10 organic components, with O:C of components ranging from 0.30 – 1.33, as shown in Fig. 5.1b. This mixture comprises dicarboxylic acids (green), aromatic compounds (pink), pinolic and pinonic acids (purple), polyols (cyan), and levoglucosan (yellow). COM4/AS/H_2O (see Supplementary

Material, Table S1 for exact mixture composition) with O:C = 0.77 shows no LLPS while a LLPS occurs in case of the mixtures COM1, COM2, and COM3 with O:C ≤ 0.71. This range in O:C with regard to the occurrence of LLPS is in agreement with the ones of the simpler systems.

We investigated three different mixtures with O:C = 0.63 and 0.67 and different degree of compositional complexity: C6/AS/H_2O (O:C = 0.67) consisting of three dicarboxylic acids each with O:C = 0.67 (Song et al., 2012a); (C5+C6+C7)/AS/H_2O (O:C = 0.67) consisting of nine dicarboxylic acids with a spread of O:C from 0.57 – 0.80; and COM1/AS/H_2O (O:C = 0.63) containing 10 components with more variety of compounds and a spread of O:C from 0.30 – 1.25. These three mixtures exhibit SRH in a similar range, namely at 73 – 74 % (C6/AS/H_2O), 70 – 74 % (C5+C6+C7/AS/H_2O), and 72 – 85 % (COM1/AS/H_2O) for the investigated OIR (Fig. 5.2a). This suggests that the complexity of the mixture in terms of component number and spread of O:C of the components is of minor importance regarding the occurrence of LLPS but may influence the SRH.

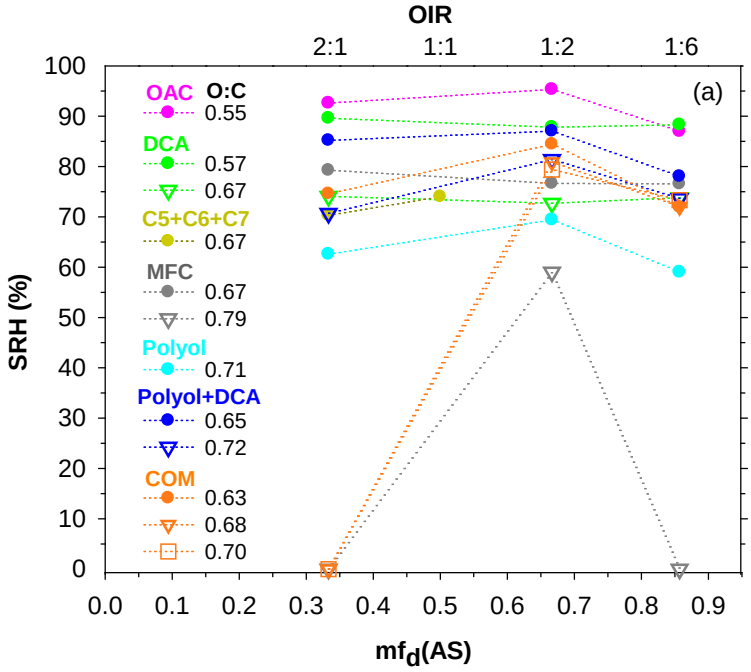
OIR
2:1
1:1
1:2
1:6
(a)
SRH (%)
mf$_d$(AS)
OAC O:C
0.55
DCA
0.57
0.67
C5+C6+C7
0.67
MFC
0.67
0.79
Polyol
0.71
Polyol+DCA
0.65
0.72
COM
0.63
0.68
0.70

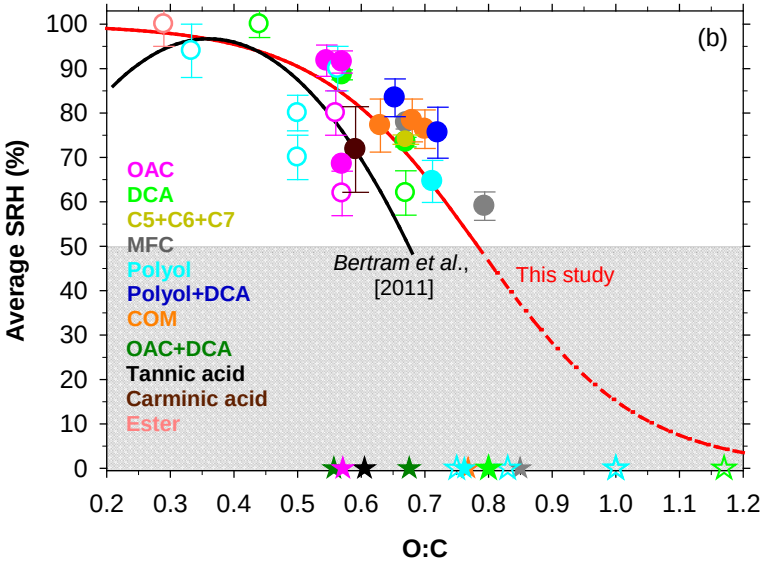
(b)
Average SRH (%)
O:C
OAC
DCA
C5+C6+C7
MFC
Polyol
Polyol+DCA
COM
OAC+DCA
Tannic acid
Carminic acid
Ester
Bertram et al., [2011]
This study

Figure 5.2 *Onset RH of LLPS (SRH) in the investigated organics/AS/H_2O droplets. (a) Systems showing LLPS with AS dry mass fraction (mf_d(AS)) = 0.33, 0.50, 0.67 and 0.86 (lower abscissa) corresponding to organic-to-inorganic dry mass ratios (OIR) = 2:1, 1:1, 1:2 and 1:6 (upper abscissa). (b) Average SRH (circles, average of all OIR that showed LLPS) from this study (filled symbols) and literature (open symbols, see Fig. 5.1c). Mixtures showing no LLPS are indicated as stars at RH = 0 %. The gray shaded region indicates the RH range in which efflorescence was observed in this study. The curves represent a second-order polynomial fit in black from Bertram et al., (2011) and a sigmoid fit in red from this study of all systems with LLPS (all circles). The dashed curve parts in the gray shaded region represent extrapolations and are not supported by experimental data (due to AS efflorescence). Error bars: standard deviation of the SRH from experiments with different particles.*

5.4.3 Summary of all investigated systems

Figure 5.1c summarizes the occurrence range of LLPS from all systems investigated in this study and from measurements reported in the literature. The yellow-hatched region in Fig. 5.1c marks the range of O:C < 0.56, in which all mixtures showed LLPS while the gray-hatched range of O:C > 0.80 indicates the region where LLPS never occurred. In the white region with 0.56 < O:C < 0.8, the occurrence of LLPS depends on the functional group composition. If one constrains the functional group composition to typical mixtures found in tropospheric aerosols with high shares of carboxylic acid and hydroxyl groups, and low amounts of aromatic compounds (below 1 %) (e.g. Gilardoni et al., 2009; Russell et al., 2009; Takahama et al., 2011), LLPS is expected for O:C < 0.71. Considering that typical values of O:C and OIR in ambient samples range between 0.2 and 1.0 (Heald et al., 2010; Takahama et al., 2011) and between 4:1 and 1:5, respectively (Zhang et al., 2007), LLPS is expected to be a phenomenon occurring frequently in tropospheric aerosols.

5.5 Atmospheric implications

The presence of LLPS affects the gas-particle partitioning of semivolatile compounds and water and influences efflorescence and deliquescence of the inorganic components compared to assuming completely mixed particles (Zuend et al., 2010; Zuend and Seinfeld, 2012), with consequences for aerosol size distribution and particulate matter mass, and thus, the direct radiative effect of aerosols. Atmospheric aerosol particles with LLPS may show a core-shell or a partially engulfed morphology (e.g., Kwamena et al., 2010; Song et al., 2012a). A core-shell morphology has more drastic consequences for the interaction of the particles with the surrounding gas phase, especially when the organic-rich phase is highly viscous (e.g. Krieger et al., 2012). Low diffusivities in the organic-rich coating may hinder gas-particle partitioning of semivolatile species and water, conserving thermodynamic non-equilibrium states. If the aqueous inorganic-rich phase is totally enclosed by an organic coating, heterogeneous chemical reactions such as the hydrolysis of N_2O_5 may be suppressed effectively (e.g. Anttila et al., 2007; Riemer et al., 2009). An AS-rich core surrounded by an organic-rich coating was the prevalent configuration of the investigated aerosol particles in this study. A comprehensive analysis of the particle morphology and its consequences will be the subject of a further study.

5.6 Acknowledgments

This work was supported by the Swiss National Foundation, Project No. 200020-125151 and by the CCES project IMBALANCE funded by the ETH Domain.

5.7 Supplementary Material

5.7.1 Experimental methods

The instrument operation, experimental procedure, and evaluation methods have been described in detail previously (Song et al., 2012a). Micrometer-sized aqueous droplets were deposited on a hydrophobically coated glass

slide using a droplet generator. The glass slide was mounted inside the flow-cell. Aqueous solutions for droplet injection were prepared with purified water (resistivity ≥ 18.0 MΩ cm). To change the relative humidity (RH) inside the flow-cell, the water vapor mixing ratio of a constant N_2/H_2O flow (180 sccm) was varied. This flow was brought to 293.2 ± 0.1 K before entering the cell, which was also kept at 293.2 ± 0.1 K. RH was measured by a G-TUCN.34 sensor (U.P.S.I., France), which was calibrated by observing the deliquescence RH (DRH) for pure $(NH_4)_2SO_4$ (80.0 %), NH_4NO_3 (65.5 %) and NaI (38.0 %) crystals at 293 K. At the beginning of an experiment, the droplets were equilibrated at a RH of < ~100 % during 15 minutes and a single droplet was chosen for observation. The RH was decreased continuously from ~100 % down to 25 % if (partial) efflorescence was observed and to ~0 % in case of no efflorescence. Subsequently, RH was continuously increased to ~100 %. Typically, experiments were carried out twice, once at a rate of 0.14 % and once at a rate of 0.39 % RH min^{-1}. No variation of the results was observed with these rates. The morphological changes of the particle were monitored optically with the microscope and recorded by a CCIR video camera with an acquisition frequency of 25 frames s^{-1}.

For the most volatile organic substances experiments were performed to test whether they show significant evaporation during a humidity cycle at 293 K. These semivolatile components are: pinonic acid, vapor pressure (VP) at 293 K: 7.90×10^{-3} Pa, estimate by the EVAPORATION model (Compernolle et al., 2011); 3-hydroxybenzoic acid, VP estimate at 293 K: 2.73×10^{-4} Pa or 2.97×10^{-5} Pa using the VP estimation model of Nannoolal et al. (2008) or Moller et al. (2008), respectively, from the E-AIM website http://www.aim.env.uea.ac.uk/aim/aim.php; and 2,4,5-trimethoxybenzoic acid (asaronic acid), VP estimate at 293 K: 3.85×10^{-3} Pa (Nannoolal et al., 2008) or 9.11×10^{-4} Pa (Moller et al., 2008). Small crystals of these substances were deposited in the flow-cell and monitored during a humidity cycle. For none of these substances any change in shape was visible, evidencing that there was no appreciable evaporation occurring. Furthermore, we checked whether the more hydrophobic (low O:C ratio) substances would spread on the substrate by measuring the contact angle of droplets with O:C = 0.33 (consisting of 1,2-hexanediol) and O:C = 0.50

(1,2-butanediol) on the substrate. They exhibited contact angles of 55° and 68°, respectively, and did not spread on the substrate.

5.7.2 O:C calculation

In this study, we mixed various organic components with ammonium sulfate (AS) in water, and determined the mixture's O:C ratio by the following equation:

$$\mathrm{O{:}C} = \frac{\sum_{k=1}^{n} \frac{mf_k}{MW_k} \times O_k}{\sum_{k=1}^{n} \frac{mf_k}{MW_k} \times C_k}$$

n: number of organic components in the mixture
k: organic component
mf_k: mass fraction of component k in the mixture
MW_k: molecular weight of component k
O_k: number of oxygen atoms in a molecule of component k
C_k: number of carbon atoms in a molecule of component k

5.7.3 Parameterization of average onset RH of liquid-liquid phase separation

A parameterization of the average onset RH of LLPS (SRH) in the range of AS dry mass fraction ($mf_d(AS)$), $0.1 < mf_d(AS) < 0.9$, as a function of O:C was obtained by fitting a three-parameter sigmoid function to data from this study and the literature (Marcolli and Krieger, 2006; Ciobanu et al., 2009; Bertram et al., 2011; Song et al., 2012a) at temperatures between 290 and 298 K.

$$\mathrm{SRH}\ (\%) = \frac{10^{1.76}}{10^{1.76} + 0.11 \times 10^{3.45 \times (\mathrm{O{:}C})}} \times 100\ \%$$

5.7.4 Supporting Tables

Table 5.2 show the list of investigated organic/AS/H_2O model mixtures, namely “complex organic mixture (COM)” (Table S1), “oxidized aromatic compound (OAC) + dicarboxylic acid (DCA)” (Table S2), “Polyol+DCA” (Table S3), “OAC” (Table S4), “Polyol” (Table S5), “multi-functional compound (MFC)” (Table S6) and “DCA” (Table S7). Each mixture consists of an organic fraction and AS with different organic-to-inorganic dry mass ratios (OIR). The Tables give the organic components in terms of organic dry mass fraction (mf_d(org) (%)), the O:C and H:C ratios, the occurrence of LLPS: present (“yes”) or absent (“no”), and the onset RH of LLPS (%) (SRH) for OIR = 2:1, 1:2 and 1:6 (“0” = no LLPS, “-” = no experiment performed). The uncertainty in the SRH was typically 1.5 % RH.

Table 5.2 *List of investigated organic/AS/H_2O model mixtures (S1- S7).*

Table S1. COM/AS/H_2O

	COM1	COM2	COM3	COM4
Components (O:C)	mf_d(org) (%)	mf_d(org) (%)	mf_d(org) (%)	mf_d(org) (%)
Diethylmalonic acid (0.57)	12.5	0.0	0.0	0.0
Methylmalonic acid (1.00)	0.0	12.5	0.0	12.5
Malonic acid (1.33)	0.0	0.0	12.5	12.5
Glutaric acid (0.80)	0.0	0.0	0.0	12.5
2-methylglutaric acid (0.67)	12.5	12.5	12.5	0.0
3-methyladipic acid (0.57)	12.5	12.5	12.5	0.0
Malic acid (1.25)	12.5	12.5	12.5	12.5
Levoglucosan (0.83)	12.5	12.5	12.5	12.5
Pinonic acid (0.30)	3.125	3.125	3.125	3.125
Pinolic acid (0.30)	3.125	3.125	3.125	3.125
3-hydroxybenzoic acid (0.43)	6.25	6.25	6.25	6.25
3,5-dihydroxybenzoic acid (0.57)	12.5	12.5	12.5	12.5
1,2,7,8-octanetetrol (0.50)	12.5	12.5	12.5	12.5
O:C	0.63	0.68	0.70	0.77

H:C	1.57	1.50	1.53	1.44
LLPS	yes	yes	yes	no
SRH for OIR = 2:1; 1:2; 1:6	74.6; 84.5; 71.9	0; 80.9; 72.0	0; 79.4; 73.3	0; 0; 0

Table S2. OAC+DCA/AS/H_2O

	OAC+DCA1	OAC+DCA2	OAC+DCA3
Components (O:C)	mf_d(org) (%)	mf_d(org) (%)	mf_d(org) (%)
3-hydroxybenzoic acid (0.43)	6.25	6.25	6.25
4-hydroxybenzoic acid (0.43)	6.25	6.25	6.25
2,5-dihydroxybenzoic acid (0.57)	12.5	18.75	18.75
2,6-dihydroxybenzoic acid (0.57)	6.25	6.25	6.25
3,4-dihydroxybenzoic acid (0.57)	6.25	6.25	6.25
3,5-dihydroxybenzoic acid (0.57)	37.5	43.75	43.75
Malonic acid (1.33)	12.5	6.25	0.0
Malic acid (1.25)	12.5	6.25	0.0
Diethylmalonic acid (0.57)	0.0	0.0	6.25
2-methylglutaric acid (0.67)	0.0	0.0	6.25
O:C	0.68	0.61	0.56
H:C	0.95	0.90	0.95
LLPS	no	no	no
SRH for OIR = 2:1; 1:2; 1:6	-; 0; -	-; -; 0	-; 0; 0

Table S3. Polyol+DCA/AS/H_2O

	Polyol+DCA1	Polyol+DCA2
Components (O:C)	mf_d(org) (%)	mf_d(org) (%)
Levoglucosan (0.83)	20	0.0
Glutaric acid (0.80)	20	0.0
2-methylglutaric acid (0.67)	0.0	30
Diethylmalonic acid (0.57)	20	30
Sorbitol (1.00)	20	20
1,2,7,8-octanetetrol (0.50)	20	20
O:C	0.72	0.65
H:C	1.90	1.92
LLPS	yes	yes
SRH for OIR = 2:1; 1:2; 1:6	70.7; 81.4; 73.6	85.2; 87.0: 78.0

Table S4. OAC/AS/H_2O

	OAC1	OAC2	2,5-dihydroxybenzoic acid	2,6-dihydroxybenzoic acid
Components (O:C)	mf_d(org) (%)	mf_d(org) (%)	mf_d(org) (%)	mf_d(org) (%)
2,4,5-trimethoxybenzoic acid (0.50)	35	0.0	0.0	0.0
3,5-dihydroxybenzoic acid (0.57)	35	70	0.0	0.0

2,5-dihydroxybenzoic acid (0.57)	30	30	100	0.0
2,6-dihydroxybenzoic acid (0.57)	0.0	0.0	0.0	100
O:C	0.55	0.57	0.57	0.57
H:C	0.98	0.86	0.86	0.86
LLPS	yes	no	yes	yes
SRH for OIR = 2:1; 1:2; 1:6	92.6; 95.3; 87.0	-; 0; 0	-; 68.5; -	-; 91.5; -

Table S5. Polyol/AS/H_2O

	Polyol1	Polyol2
Components (O:C)	mf_d(org) (%)	mf_d(org) (%)
Sorbitol (1.00)	50	60
1,2,7,8-octanetetrol (0.50)	50	40
O:C	0.71	0.76
H:C	2.29	2.29
LLPS	yes	no
SRH for OIR = 2:1; 1:2; 1:6	62.6; 69.4; 59.0	- ; 0; 0

Table S6. MFC/AS/H_2O

	MFC1	MFC2	MFC3
Components (O:C)	mf_d(org) (%)	mf_d(org) (%)	mf_d(org) (%)
2-oxoglutaric acid (1.00)	0.0	0.0	30
Maleic acid (1.00)	20	50	30
3,4-Dihydro-2,2-dimethyl-4-oxo-2H-pyran-6-carboxylic acid (0.50)	20	10	5
Itaconic acid (0.80)	20	15	15
Dehydroacetic acid (0.50)	20	10	5

Kojic acid (0.67)	20	15	15
O:C	0.67	0.79	0.84
H:C	1.09	1.06	1.10
LLPS	yes	yes	no
SRH for OIR = 2:1; 1:2; 1:6	79.3; 76.6; 76.5	0; 59.0; 0	-; 0; 0

Table S7. DCA/AS/H_2O

	DCA(C7)	DCA(C6)	DCA(C5)	DCA (C5+C6+ C7)
Components (O:C)	mf_d(org) (%)	mf_d(org) (%)	mf_d(org) (%)	mf_d(org) (%)
3-methyladipic acid (0.57)	33.3	0.0	0.0	11.1
3,3-dimethylglutaric acid (0.57)	33.3	0.0	0.0	11.1
Diethylmalonic acid (0.57)	33.3	0.0	0.0	11.1
2-methylglutaric acid (0.67)	0.0	33.3	0.0	11.1
3-methylglutaric acid (0.67)	0.0	33.3	0.0	11.1
2,2-dimethylsuccinic acid (0.67)	0.0	33.3	0.0	11.1
Glutaric acid (0.80)	0.0	0.0	33.3	11.1
Methylsuccinic acid (0.80)	0.0	0.0	33.3	11.1
Dimethylmalonic acid (0.80)	0.0	0.0	33.3	11.1
O:C	0.57	0.67	0.80	0.67
H:C	1.71	1.67	1.60	1.67
LLPS	yes	yes	no	yes
SRH for OIR = 2:1; 1:1; 1:2; 1:6	89.6; -; 87.8; 88.3	74.1; -; 72.7; 73.8	0; -; 0; -	70.3; 74.0; -; -

Chapter 6

Morphologies of mixed organic/inorganic/aqueous aerosol droplets

This chapter is a reproduction of the article accepted in the *Faraday Discussions*:

Song, M., C. Marcolli, U. K. Krieger, D. Lienhard, and Peter, T., Morphologies of mixed organic/inorganic/aqueous aerosol droplets, Accepted, Faraday Discuss. 2013.

6.1 Abstract

Despite major progress in the understanding of properties of tropospheric aerosol particles, it remains challenging to understand their physical state and morphology. To obtain more detailed knowledge of the phases, phase transitions and morphologies of internally mixed organic/inorganic aerosol particles, we evaluated liquid-liquid phase separation (LLPS), deliquescence relative humidity (DRH) and efflorescence relative humidity (ERH) of 33 organic/ammonium sulfate (AS)/H_2O systems from own and literature data. The organic fraction consists of single compounds or mixtures with up to ten aliphatic and/or aromatic components with carboxylic acid, hydroxyl, carbonyl, ether, and ester functionalities, covering O:C ratios between 0.29 and 1.33. Thirteen out of these 33 systems did not show LLPS for any of the studied organic-to-inorganic mixing ratios, sixteen underwent LLPS showing core-shell morphology, and four showed both core-shell and partially engulfed configurations depending on the organic-to-inorganic ratio and RH. In all cases the organic fractions of the systems with partially engulfed configurations consisted of dicarboxylic acids. AS in mixed organic/AS/H_2O particles deliquesced between 70 and 84 % RH. AS effloresced below 58 % RH or remained in a one-liquid-phase state. AS in droplets with LLPS always showed efflorescence with ERH between 30 and 50 % RH, providing clear evidence that the presence of LLPS facilitates AS efflorescence. Spreading coefficients of the organic-rich phase on the AS-rich phase for systems containing polyethylene glycol 400 (PEG-400) and a mixture of dicarboxylic acids are in agreement with the optically observed morphologies of droplets deposited on the hydrophobic substrate. Analysis of high resolution elastic Mie resonance spectra allowed the detection of LLPS for single levitated droplets consisting of PEG-400/AS/H_2O, whereas LLPS was difficult to detect in (2-methylglutaric acid + 3-methylglutaric acid + 2,2-dimethylsuccinic acid)/AS/H_2O. Measured Mie spectra of PEG-400/AS/H_2O at 93.5 % and at 80.9 % RH agreed with computed Mie spectra for a homogeneous and a core-shell configuration, respectively, confirming the results obtained from droplets deposited on a hydrophobic substrate. Based on the presented evidence, the core-shell morphology as the prevalent configuration of liquid-liquid-phase-separated tropospheric organic/AS/H_2O particles.

6.2 Introduction

Aerosol particles are an important atmospheric component, significantly affecting both climate and air quality (Seinfeld and Pandis, 2006). The chemical composition, physical state, morphology and size influence their forcing and therefore should be known to predict accurately the impact of aerosols on climate (Hanel, 1976; Martin, 2000; IPCC, 2007). Gas-particle partitioning of semivolatile compounds and atmospheric chemistry, specifically the heterogeneous reaction of N_2O_5, are linked with the physical state and morphology of the aerosol particles (Anttila et al., 2007; Cosman et al., 2008; Zuend et al., 2010; Zuend and Seinfeld, 2012).

Tropospheric aerosols comprise organic constituents, inorganic salts, and water. These components are mostly internally mixed (Lee et al., 2002; Marcolli et al., 2004b; Murphy et al., 2006). The physical state of aerosol particles depends on chemical composition, RH and temperature (Kwamena et al., 2010; Reid et al., 2011; Krieger et al., 2012). Depending on these factors, atmospheric aerosol particles may be present as one liquid phase, two liquid phases, crystalline phases, in a glassy state and as mixture of these phases (Krieger et al., 2012). When aerosol particles are exposed to varying humidity in the atmosphere, they may undergo phase transitions such as liquid-liquid phase separation (LLPS), deliquescence, and efflorescence. Recent laboratory studies using optical microscopy showed that LLPS in internally mixed organic/ammonium sulfate (AS)/H_2O aerosol particles is expected to be a common feature in the atmosphere (Bertram et al., 2011; Song et al., 2012a). Since O:C reflects the polarity of organic components and their affinities to water and electrolytes, it can be an important parameter to determine the occurrence of LLPS in an aerosol (Bertram et al., 2011; Song et al., 2012a). Song et al. (2012b), found for atmospheric relevant mixtures consisting of organics/AS/H_2O with up to 10 organic components that separation into two liquid phases always occurred for O:C < 0.56 and

depended on the specific types of organic functional groups in the range of 0.56 < O:C < 0.80. There is no direct measurement technique available that is able to observe LLPS in ambient aerosols. Recently, ambient aerosols were collected on filters and the physical state was observed in the laboratory (Pöhlker et al., 2012; You et al., 2012). Aerosol samples collected near the city of Atlanta that is highly influenced by both anthropogenic and biogenic emissions and exhibited O:C of roughly less than 0.5 also showed LLPS (You et al., 2012). Moreover, the presence of LLPS in Amazon aerosol samples, which contained a high share of aliphatic carboxylic acids and hydroxyl functional groups in the presence of inorganic microgranular material (Pöhlker et al., 2012), was in agreement with the O:C ranges of LLPS specified by Song et al. (2012b). The composition of the organic fraction and the mixing state of aerosol particles may influence deliquescence relative humidity (DRH) and efflorescence relative humidity (ERH) of inorganic salts during RH cycles (Marcolli et al., 2004a; Parsons et al., 2006; Ciobanu et al., 2009; Bertram et al., 2011; Smith et al., 2011; Smith et al., 2012; Song et al., 2012a). No significant reduction of ERH and DRH was observed for moderately hydrophobic aerosol particles with O:C < 0.60 such as PEG-400/AS/H_2O, C7/AS/H_2O, and secondary organic material (SOM) (produced by dark ozonolysis of α-pinene)/AS/H_2O over the whole investigated dry (water-free) mass fractions of AS (mf_d(AS)) from 0 – 1 (Ciobanu et al., 2009; Smith et al., 2011; Song et al., 2012a). Due to the high viscosity of the organic fraction in the organic-rich phase, the ERH was slightly decreased in systems consisting of C6/AS/H_2O and C7/AS/H_2O with mf_d(AS) < 0.25 (Song et al., 2012a). On the other hand, DRH and ERH of AS in hydrophilic organic/AS/H_2O particles (O:C > 0.70) were reduced significantly or even totally suppressed (Bertram et al., 2011).

LLPS in mixed aerosol particles may lead to different particle morphologies such as core-shell or partially engulfed configurations. Since there exist no in situ measurement techniques to monitor the ambient aerosols, determination of aerosol morphology is challenging. Using optical microscopy and Raman spectroscopy, a core-shell configuration consisting of an AS inner phase coated by an organic outer phase has been observed for O:C < 0.70 in phase separated

organic/AS/H_2O particles deposited on a hydrophobically coated substrate (Ciobanu et al., 2009; Bertram et al., 2011). Atlantic aerosol samples (O:C ~ 0.5) also adopted a core-shell structure when present in a two-liquid-phases state as observed by optical microscopy (You et al., 2012). In contrast, recent laboratory studies using micrometer-sized levitated particles showed that for particles composed of aqueous salts and organics with low O:C of ~0.1 a partially engulfed structure is the prevalent morphology (Kwamena et al., 2010; Reid et al., 2011). Song et al., (2012a) observed both morphologies in C6/AS/H_2O and C7/AS/H_2O particles on a substrate, but the partially engulfed structure was found only in a limited range of organic-to-inorganic mass ratio. Therefore, more laboratory experiments are necessary to obtain deeper insight into aerosol morphologies depending on their chemical composition and physical states.

The present study aims to explore how the deliquescence and efflorescence of AS in mixed organic/AS/H_2O particles is influenced by LLPS and to identify the corresponding morphologies with optical microscopy. To obtain conclusions whether the core-shell or the partially engulfed configuration is prevalent when there is no interaction with a substrate, we use an electrodynamic balance to investigate particles with compositions that led to core-shell or partially engulfed morphology on a hydrophobic substrate. Furthermore, surface and interfacial tensions of model systems are obtained and evaluated.

6.3 Experiments

Phase transitions and morphological changes of internally mixed organic/AS/H_2O particles during humidity cycles were observed using an optical microscope equipped with a temperature- and humidity-controlled flow-cell. The detailed experimental procedure and method have been previously described in Song et al. (2012a, 2012b). The solutions containing the organic components and AS were prepared in purified water (resistivity ≥ 18.0 MΩ cm). All substances were purchased from Sigma-Aldrich with purities ≥ 98 % and were used

without further purification.

Micrometer-sized aqueous droplets (20 – 65 μm in diameter) were deposited on a hydrophobically coated substrate using a droplet generator (Knopf, 2003), and the substrate was mounted inside the flow-cell and equilibrated at ~100 % RH for 15 minutes. The cell temperature was kept at 293.2 ± 0.1 K during the equilibration time and the humidity cycles. To observe the morphologies and phase transitions of the particles during humidity cycles, the water vapor mixing ratio of a constant total N_2/H_2O flow (180 sccm) through the cell was varied. After the equilibration at high RH, RH was continuously decreased down to 30 % if (partial) efflorescence was observed or to 0 % in the absence of efflorescence and subsequently, RH was continuously increased to ~100 % at rates of both 0.1 % and 0.4 % RH min^{-1}. RH and temperature were determined by a G-TUCN.34 sensor (U.P.S.I., France) and the temperature was also measured directly under the substrate by a Pt100 temperature sensor (Minco, USA). RH calibration of the G-TUCN.34 sensor was done by observing the DRH of pure crystals of salts such as $(NH_4)_2SO_4$ (80.0 %), NH_4NO_3 (65.5 %) and NaI (38.0 %) at 293 K. The uncertainty of the sensor was typically ± 1.5 % RH. To observe the morphological change of aerosol particles, a microscope equipped with a long working distance objective (Olympus BX-40, magnification 50, aperture 0.7) was used. We also recorded the optical images of the droplets during humidity cycles using a black and white CCIR video camera (25 frames s^{-1}).

Surface and interfacial tension measurements were carried out by IMETER (MessSysteme, Augsburg, Germany) using the ring method applying the DIN 53914, the ASTM D 1331 and the ISO 6889 norms for execution and evaluation. The ring method was corrected according to the German patent DE 4412405. The detection limit of the ring method for interfacial tension measurements is ~0.5 mN m^{-1} and depends among other factors on the flatness of the ring and the interface. Interfacial tensions were determined once in the phase separated systems. For surface tension measurements the two liquid phases were separated in a separating funnel. Samples for surface tension measurements were prepared and measured twice and the average of the two values was taken. Samples of PEG-400/AS/H_2O and C6+C7/AS/H_2O were measured

at 298 K, at 293 K, respectively. Density measurements were carried out using a pycnometer (BRAND, Germany) at 293 K.
To investigate the potential impact of the substrate on particle morphology when using the microscope technique we performed additional experiments on single particles levitated in an electrodynamic balance (EDB). The setup has been described in detail previously (Krieger et al., 2000, Colberg et al. 2004). While deliquescence and efflorescence are easily detected using temporal intensity fluctuations of scattered light (Krieger and Braun, 2001) or spatial distortions in the two dimensional angular scattering pattern (Braun and Krieger, 2001), it proved impossible to detect LLPS using these techniques (Marcolli and Krieger, 2006). Therefore, we added to the setup a tunable diode laser with narrow line width (New Focus, model Velocity 6312), to measure high resolution Mie resonance spectra. The wavelength of the laser is monitored using a Michelson interferometer (Te, 2011). The levitated particle is illuminated from below; the beam is weakly focused with 400 mm focal length lens. The detector (Si photodiode, New Focus femtowatt photoreceiver, model 2151) is placed at 90° relative to the incoming beam at the same height as the levitated particle; a lens integrates the scattered light of the particle over scattering angles ranging from 78° to 101°. The polarization of the incoming laser can be shifted using a motorized λ/2-wave plate so that the incident electric field is either parallel or perpendicular to the scattering plane (the plane defined by the forward direction of the laser beam and the scattering direction). Thus, either spectra of transversal electric polarization (TE) or transversal magnetic polarization (TM) are measured. Typically, we scan the laser from 765.0 nm to 781.5 nm using a scan speed of 0.04 nm s^{-1}, turn the λ/2-wave plate and measure TE and TM spectra subsequently. Refractive indices of bulk solutions, n_D, were measured with an Abbe type refractometer.

6.4 Results and discussion

Table 6.1 *Optical microscope and EDB experiments collected from this study and literature. Abbreviations: COM, complex organic mixture; DCA, dicarboxylic acids; OAC, oxidized aromatic compounds; MFC,*

*multifunctional compounds; SRH, onset RH of LLPS; Abs, no LLPS occurred; AS incs, AS inclusions in organic-rich phase; CS, core-shell configuration; PE, partially engulfed configuration; HA, homogeneous appearance; "?", not clear; "-", not measured or no information given; "0", particle did not crystallize. Literature: a, Song et al. (2012b) and this study; b, Song et al. (2012a); c, this study; d, Bertram et al. (2011) ; e, Ciobanu et al. (2009); f, Yeung et al. (2009); g, Pant et al. (2004); h, Parsons et al. (2004); i, Bodsworth et al. (2010); j, Zardini et al. (2008); k, Chan et al. (2006); l, Choi and Chan (2002); m, Ling and Chan (2008); n, Marcolli and Krieger (2006); o, Parsons et al. (2006); *, Song et al. (2012b); **, Bertram et al. (2011).*

Mixture (O:C)	Organic components (wt% of component in organic mixture)	Studied mf_d(AS)	LLPS SRH	LLPS Morph.	ERH	DRH
		Optical microscopy				
COM1/AS/H_2O [a] (0.63)	2-methylglutaric acid (12.5); 3-methyladipic acid (12.5); diethylmalonic acid (12.5); malic acid (12.5); levoglucosan (12.5); pinonic acid (3.125); pinolic acid (3.125); 3-hydroxybenzoic acid (6.25); 3,5-dihydroxybenzoic acid (12.5); 1,2,7,8-octanetetrol (12.5)	0.14, 0.20, 0.26, 0.30, 0.33, 0.40, 0.50, 0.67, 0.80, 0.86, 0.91	Abs, Abs, Abs, 70.1, *74.2, 81.0, 83.3, *84.5, 83.1, *71.9, Abs	HA, HA, HA, CS, CS, CS, CS, CS, CS, CS, HA	0, 21.0, 35.2, 46.6, 40.8, 43.9, 42.3, 43.6, 44.7, 44.9, 47.9	-, 72.3, 74.3, 75.3, 75.5, 76.2, 76.3, 77.0, 77.7, 78.0, 78.8
COM2/AS/H_2O [a] (0.68)	2-methylglutaric acid (12.5); 3-methyladipic acid (12.5); methylmalonic acid (12.5); malic acid (12.5); levoglucosan (12.5); pinonic acid (3.125); pinolic acid (3.125); 3-hydroxybenzoic acid (6.25); 3,5-dihydroxybenzoic acid (12.5); 1,2,7,8-octanetetrol (12.5)	0.14, 0.33, 0.67, 0.86	Abs, *Abs, *80.9, *72.0	HA, HA, CS, CS	0, 37.4, 42.7, 46.5	-, 74.7, 79.2, 78.1
COM3/AS/H_2O [a] (0.70)	2-methylglutaric acid (12.5); 3-methyladipic acid (12.5); malonic acid (12.5); malic acid (12.5); levoglucosan (12.5); pinonic acid (3.125); pinolic acid (3.125); 3-hydroxybenzoic acid (6.25); 3,5-dihydroxybenzoic acid (12.5); 1,2,7,8-octanetetrol (12.5)	0.33, 0.67, 0.86	*Abs, *79.4, *73.3	HA, CS, CS	33.6, 47.5, 44.4	74.1, 77.1, 77.7
COM4/AS/H_2O [a] (0.77)	Malonic acid (12.5); glutaric acid (12.5); methylmalonic acid	0.33, 0.67, 0.86	*Abs, *Abs, *Abs	HA, HA, HA	27.0, 41.5, 47.9	71.9, 76.4, 77.5

	(12.5); malic acid (12.5); levoglucosan (12.5); pinonic acid (3.125); pinolic acid (3.125); 3-hydroxybenzoic acid (6.25); 3,5-dihydroxybenzoic acid (12.5); 1,2,7,8-octanetetrol (12.5)					
OAC+DCA1/AS/H_2O[a] (0.68)	3-hydroxybenzoic acid (6.25); 4-hydroxybenzoic acid (6.25); 2,5-dihydroxybenzoic acid (12.5); 2,6-dihydroxybenzoic acid (6.25); 3,4-dihydroxybenzoic acid (6.25); 3,5-dihydroxybenzoic acid (37.5); malonic acid (12.5); malic acid (12.5)	0.67	*Abs	HA	49.4	77.0
OAC+DCA2/AS/H_2O[a] (0.61)	3-hydroxybenzoic acid (6.25); 4-hydroxybenzoic acid (6.25); 2,5-dihydroxybenzoic acid (18.75); 2,6-dihydroxybenzoic acid (6.25); 3,4-dihydroxybenzoic acid (6.25); 3,5-dihydroxybenzoic acid (43.75); malonic acid (6.25); malic acid (6.25)	0.86	*Abs	HA	45.0	78.4
OAC+DCA3/AS/H_2O[a] (0.56)	3-hydroxybenzoic acid (6.25); 4-hydroxybenzoic acid (6.25); 2,5-dihydroxybenzoic acid (18.75); 2,6-dihydroxybenzoic acid (6.25); 3,4-dihydroxybenzoic acid (6.25); 3,5-dihydroxybenzoic acid (43.75); 2-methylglutaric acid (6.25); diethylmalonic acid	0.67, 0.86	*Abs, *Abs	HA, HA	45.1, 51.6	77.9, 78.8

	(6.25)					
Polyol+DCA1/AS/H_2O[a] (0.72)	Diethylmalonic acid (20); levoglucosan (20); glutaric acid (20); sorbitol (20); 1,2,7,8-octanetetrol (20)	0.33, 0.67, 0.86	*70.7, *81.4, *73.6	CS, CS, CS	42.1, 44.0, 42.8	74.5, 77.2, 78.1
Polyol+DCA2/AS/H_2O[a] (0.65)	2-methylglutaric acid (30); diethylmalonic acid (30); sorbitol (20); 1,2,7,8-octanetetrol (20)	0.33, 0.67, 0.86	*85.2, *87.0, *78.0	CS, CS, CS	41.9, 45.9, 43.3	76.0, 78.3, 78.7
OAC1/AS/H_2O[a] (0.55)	2,5-dihydroxybenzoic acid (30); 3,5-dihydroxybenzoic acid (35); 2,4,5-trimethoxybenzoic acid (35)	0.33, 0.67, 0.86	*92.6, *95.3 *87.0	CS, CS, CS	43.7, 44.7, 46.4	78.2, 78.9, 79.1
OAC2/AS/H_2O[a] (0.57)	2,5-dihydroxybenzoic acid (30); 3,5-dihydroxybenzoic acid (70)	0.67, 0.86	*Abs, *Abs,	HA, HA	49.0, 46.8	77.8, 79.0
Polyol1/AS/H_2O[a] (0.71)	Sorbitol (50); 1,2,7,8-octanetetrol (50)	0.33, 0.67, 0.86	*62.6, *69.4, *59.0	CS, CS, CS	29.7, 45.2, 44.0	75.3, 76.8, 78.6
Polyol2/AS/H_2O[a] (0.76)	Sorbitol (60); 1,2,7,8-octanetetrol (40)	0.67, 0.86	*Abs, *Abs,	HA, HA	41.1, 40.6	77.4, 78.5
MFC1/AS/H_2O[a] (0.67)	Maleic acid (20); dehydroacetic acid (20); kojic acid (20); 3,4-dihydroxy-2,2-dimethyl-4-oxo-2H-pyran-6-carboxylic acid (20); itaconic acid (20)	0.33, 0.67, 0.86	*79.1, *76.6, *76.5	CS, CS, CS	38.5, 43.9, 45.1	76.7, 78.2, 78.6
MFC2/AS/H_2O[a] (0.79)	Maleic acid (50); dehydroacetic acid (10); kojic acid (15); 3,4-dihydroxy-2,2-dimethyl-4-oxo-2H-pyran-6-carboxylic acid (10); itaconic acid (15)	0.33, 0.67, 0.86	*Abs, *59.0, *Abs	HA, CS, HA	40.1, 49.5, 44.4	72.0, 77.3, 78.0
MFC3/AS/H_2O[a] (0.84)	2-oxoglutaric acid (1.00); maleic acid (30); dehydroacetic acid (5); kojic acid	0.67, 0.86	*Abs, *Abs	HA, HA	46.7, 46.6	76.9, 78.3

	(15); 3,4-dihydroxy-2,2-dimethyl-4-oxo-2H-pyran-6-carboxylic acid (5); itaconic acid (15)					
DCA(C7)/AS/H_2O[b] (0.57)	3-methyladipic acid (33.3); 3,3-dimethylglutaric acid (33.3); diethylmalonic acid (33.3)	0.02-0.23, 0.34, 0.50-0.93	88.2-91.7, 89.6, 83.8-89.9	AS incs, PE, CS	33.5-41.7, 42.1, 40.3-48.2	70.1-79.8, 78.4, 78.4-81.3
DCA(C6)/AS/H_2O[b] (0.67)	2-methylglutaric acid (33.3); 3-methylglutaric acid (33.3); 2,2-dimethylsuccinic acid (33.3)	0.08-0.33, 0.50, 0.67, 0.76-0.89, 0.92	49.9-85.0, 72.9, 72.7, 72.3-72.8, Abs	AS incs, CS->PE CS->PE ?, HA	29.9-48.6, 43.7, 40.9, 39.7-45.8, 45.4	71.0-79.1, 78.1, 78.1, 78.2-80.4, 79.5
DCA(C5)/AS/H_2O[b] (0.80)	Glutaric acid (33.3); methylsuccinic acid (33.3); dimethylmalonic acid (33.3)	0.33, 0.50, 0.80	Abs, Abs, Abs	HA, HA, HA	32.4, 37.9, 40.8	75.1, 77.8, 77.9
DCA(C5+C6+C7)/AS/H_2O[a] (0.67)	Glutaric acid (11.1); methylsuccinic acid (11.1); dimethylmalonic acid (11.1); 2-methylglutaric acid (11.1); 3-methylglutaric acid (11.1); 2,2-dimethylsuccinic acid (11.1); 3-methyladipic acid (11.1); 3,3-dimethylglutaric acid (11.1); diethylmalonic acid (11.1)	0.11, 0.33, 0.50	*Abs, *70.3, *74.0	HA, AS incs, PE	18.7, 43.1, 47.8	71.8, 77.5, 78.2
DCA(C6+C7)/AS/H_2O[c] (0.61)	3-methyladipic acid (19.9); 3,3-dimethylglutaric acid (19.9); diethylmalonic acid (19.9); 2-methylglutaric acid (15.0); 3-methylglutaric acid (15.0); 2,2-dimethylsuccinic acid (10.0)	0.33, 0.50	83.3, 87.2	CS->PE CS	44.7, 49.1	78.0, 79.0
Diethyl decanedioate/A	Diethyl decanedioate (100)	0.11-0.66, 0.80	97.5-100, Abs	CS, HA	34.1-36.0, 35.8	79.1-80.2, 80.4

S/H_2O[d] (O:C = 0.29)						
Monomethyl octane- 1,8 – dioate/AS/H_2O[d] (O:C = 0.44)	Monomethyl octane- 1,8 – dioate (100)	0.18-0.68	~100	CS	33.2-35.2	78.4-79.6
1,2,6-trihydroxyhexane/AS/H_2O[d] (O:C = 0.5)	1,2,6-trihydroxyhexane (100)	0.15-0.74	69.0-72.5	CS	32.5-36.7	79.7-82.8
α,4-dihydroxy-3-methoxybenzeneacetic acid/AS/H_2O [d] (O:C =0.56)	α,4-dihydroxy-3-methoxybenzeneacetic acid (100)	0.11, 0.24-0.66	Abs, 79.0-81.3	HA, CS	0, 37.8-40.3	-, 82.5-84.1
2,5-dihydroxybenzoic acid/AS/H_2O[d] (O:C =0.57)	2,5-dihydroxybenzoic acid (100)	0.33-0.42, 0.58, 0.58-0.80	Org crys, Abs, 61.5-64.2	HA, HA, CS	-, 32.9, 33.6-36.7	-, -, -
2,2-dimethylbutane dioic acid/AS/H_2O[d] (O:C =0.67)	2,2-dimethylbutanedioic acid (100)	0.19-0.32, 0.37-0.42, 0.58-0.70	Org crys, Abs, 61.5-63.8	HA, HA, CS	-, -, 32.1-40.3	-, -, -
PEG-400/AS/H_2O[e] (~0.56)	Polyethylene glycol-400 (100)	0.11-0.33, 0.4-0.90	87-88, 87-89	As incs, CS	30-35, 30-37	77-80, 80
Adipic acid/AS/H_2O[f] (0.67)	Adipic acid (100)	0.10-0.97	-	-	35.3-40.5	79-81
Glutaric acid/AS/H_2O[g] (0.80)	Glutaric acid (100)	0.50-0.90	**Abs	**HA	29.5-34	79-79.5
Levoglucosan/ AS/H_2O[h] (0.83)	Levoglucosan (100)	0.29-0.83	**Abs	**HA	10-30	72-80
Glycerol/AS/H_2O[h] (1.00)	Glycerol (100)	0.51-0.91	**Abs	**HA	5-30	72-80
Citric acid/AS/H_2O[i] (1.17)	Citric acid (100)	0.67-1.00	**Abs	**HA	24-35	-
Malonic acid/AS/H_2O[h] (1.33)	Malonic acid (100)	0.53-0.90	**Abs	**HA	0-32	72-80
EDB measurement						
Adipic acid/AS/H_2O[j] (0.67)	Adipic acid (100)	0.25, 0.67	-	-	35, 38	80, 79
Glutaric acid/AS/H_2O[k] (0.80)	Glutaric acid (100)	0.51, 0.87	-	-	40.8, 50.7	80.0, 80.9
Glutaric acid/AS/H_2O[l] (0.80)	Glutaric acid (100)	0.50	-	-	57.5	76.6

Glutaric acid/AS/H_2O[m] (0.80)	Glutaric acid (100)	0.50	-	-	33.5	79.0
Glutaric acid/AS/H_2O[j] (0.80)	Glutaric acid (100)	0.50	-	-	32	77.5
Succinic acid/AS/H_2O[m] (1.00)	Succinic acid (100)	0.48	-	-	30	80
Succinic acid/AS/H_2O[l] (1.00)	Succinic acid (100)	0.48	-	-	48.3	79
M5/AS/H_2O[n] (1.08)	Malic acid (18); malonic acid (36); maleic acid (16); glutaric acid (22); methylsuccinic acid (8)	0.5	-	-	27	73.3
M5/AS/H_2O[n] (1.08)	Malic acid (17); malonic acid (37); maleic acid (17.5); glutaric acid (20.5); methylsuccinic acid (8)	0.8	-	-	35	78.3
Malonic acid/AS/H_2O[o] (1.33)	Malonic acid (100)	0.41-0.71	-	-	0-30	-

6.4.1 Deliquescent and efflorescent behaviors depending on mixing states of aerosols

Table 6.1 gives literature data and results from this study for ERH, DRH, LLPS and the morphology of organic/AS/H_2O particles from optical microscopy and EDB measurements. It shows that AS in mixed organic/AS/H_2O particles deliquesced between 70 and 84 % RH and effloresced below 58 % RH or remained in a one-liquid-phase state when all mixtures are considered. AS in droplets with LLPS always effloresced between 30 and 50 % RH and deliquesced between 70 and 84 % RH.

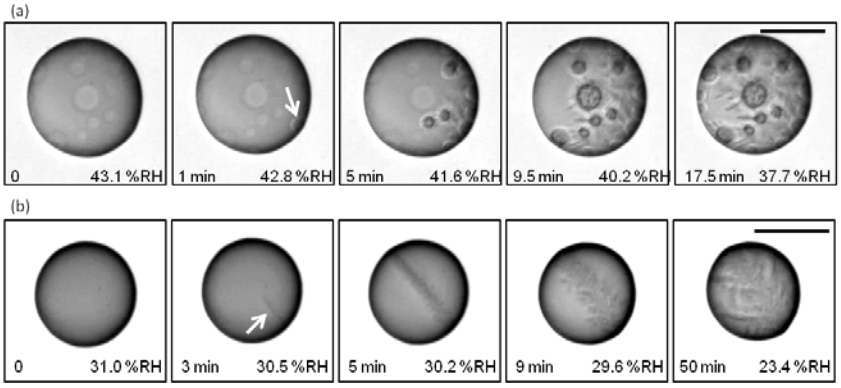

Figure 6.1 *Efflorescence process of (a) C7/AS/H_2O (O:C = 0.57), mf_d(AS) = 0.15, and (b) COM4/AS/H_2O (O:C = 0.77), mf_d(AS) = 0.33. Onset of crystallization is marked by an arrow. At time t = 0, particles are liquid. Size bar: 20 µm.*

The process of crystallization in mixed organic/AS/H_2O particles is shown in Figs. 1a, and 1b for optically monitored particles of C7/AS/H_2O (O:C = 0.57, mf_d(AS) = 0.15), and COM4/AS/H_2O (O:C = 0.77, mf_d(AS) = 0.33). In the particle of C7/AS/H_2O, which showed LLPS at 90 % RH by nucleation and growth (Song et al., 2012a), crystallization started from an aqueous AS inclusion at the rim of the particle at 42.8 % RH (marked by an arrow, t = 1 min). Subsequently, AS needles slowly grew from the inclusion into the aqueous organic-rich phase, causing the crystallization of other aqueous AS inclusions when they came in contact with them. At the end of the experiment (t = 17.5 min), all AS inclusions had effloresced and the particle was covered with needles. On the other hand, the one-liquid-phase state particle of the COM4/AS/H_2O system crystallized by forming a needle from the rim of the particle at 30.5 % RH (t = 3 min). After the needle reached the other side of the particle (t = 5 min), it started to branch into the organic-rich phase (t = 9 min). At the end of the experiment, the needles covered the particle (t = 50 min, RH = 23.4 %). Due to the high viscosity, the growth of crystalline AS occurred on the timescale of minutes in organic-rich

one-liquid-phase particles and in the organic-rich phase of mixed organic/AS/H_2O particles (Krieger et al., 2012). On the other hand, the low viscosity of the AS-rich phase allowed instantaneous crystallization (within milliseconds; see also Ciobanu et al. (2009)) of AS inclusions as soon as they were reached by a needle.

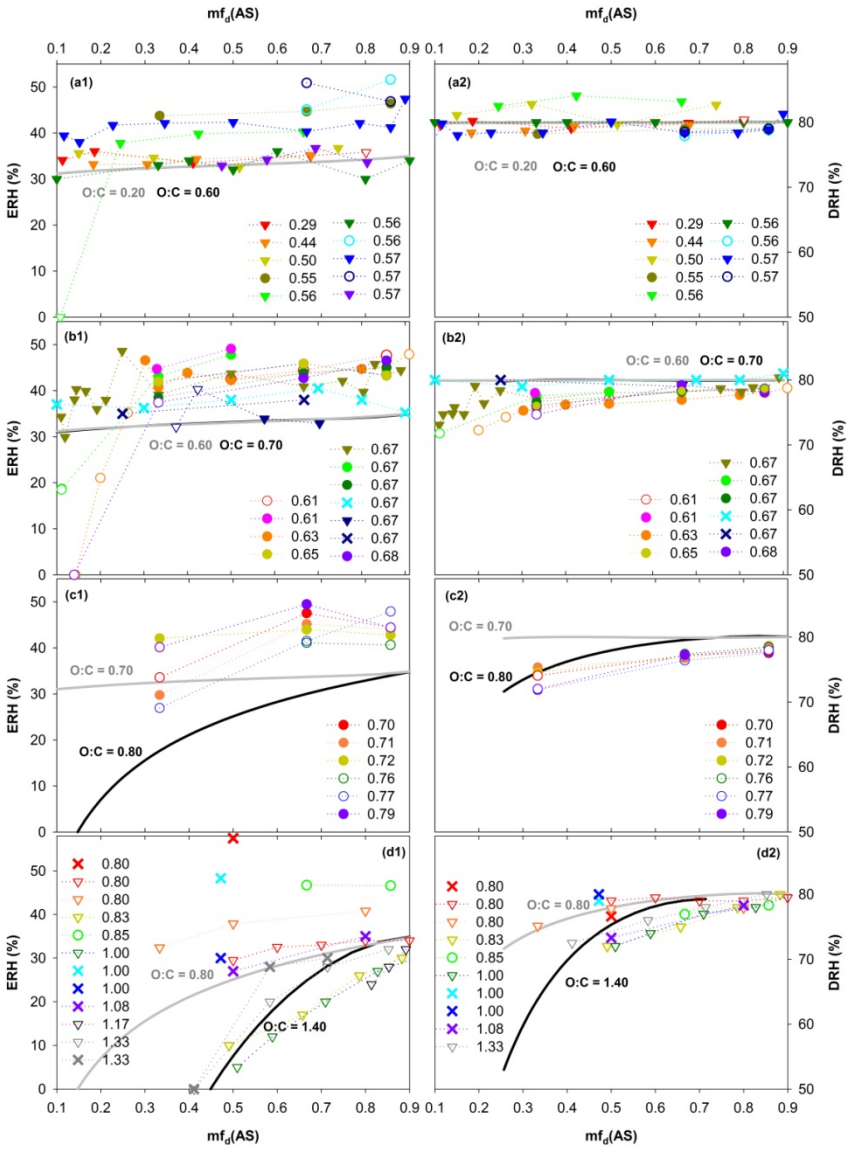

Figure 6.2 *ERH (panels a1-d1) and DRH (panels a2-d2) of organic/AS/H_2O particles as a function of AS dry mass fraction (mf_d(AS)) from this study and literature. The grey and black lines represent the prediction from Bertram et al.,15 for AS ERH and DRH based on O:C ratios. Circles: systems*

measured within this study and Song et al. (2012a) by optical microscopy. Triangles: systems measured by optical microscopy from literature. The solid and open symbols represent the presence or absence of LLPS, respectively. Crosses: systems mostly measured by EDB for which no LLPS information is provided. Panels a1 and a2: systems covering 0.2 < O:C < 0.6: O:C = 0.29 (red triangle), diethyl decanedioate; 0.44 (orange triangle), monomethyl octane-1,8-dioate; 0.50 (yellow triangle), 1,2,6-hexanetriol; 0.55 (olive circle), OAC1; 0.56 (green triangle), α,4-dihydroxy-3-methoxybenzeneacetic acid; 0.56 (dark green triangle), PEG-400; 0.56 (cyan circle), OAC+DCA3; 0.57 (blue triangle), C7; 0.57 (dark blue circle), OAC2; 0.57 (purple triangle), 2,5-dihydroxybenzoic acid. Panels b1 and b2: systems covering 0.60 < O:C < 0.70: 0.61 (red circle), OAC+DCA2; 0.61 (pink circle), C6+C7; 0.63 (orange circle), COM1; 0.65 (yellow circle), Polyol+DCA2; 0.67 (olive triangle), C6; 0.67 (green circle), C5+C6+C7; 0.67 (dark green circle), MFC1; 0.67 (cyan cross), adipic acid; 0.67 (dark blue triangle), 2,2-dimethylbutanedioic acid; 0.67 (dark blue cross), adipic acid; 0.68 (purple circle), COM2. Panels c1 and c2: systems covering 0.70 < O:C < 0.80: 0.70 (red circle), COM3; 0.71 (orange circle), Polyol1; 0.72 (yellow circle), Polyol+DCA1; 0.76 (green circle), Polyol2; 0.77 (blue circle), COM4; 0.79 (purple circle), MFC2. Panels d1 and d2: 0.80 < O:C < 1.40: 0.80 (red cross), glutaric acid; 0.80 (red triangle), glutaric acid; 0.80 (orange triangle), C5; 0.83 (yellow triangle), levoglucosan; 0.85 (green circle), MFC3; 1.00 (dark green triangle), glycerol; 1.00 (cyan cross), succinic acid; 1.00 (blue cross), succinic acid; 1.08 (purple cross), M5; 1.17 (black triangle), citric acid; 1.33 (grey triangle), malonic acid; 1.33 (grey cross), malonic acid.

Figure 6.2 presents the optical microscope measurements of DRH and ERH in terms of mf_d(AS) for organic/AS/H_2O particles from this work (circles) and literature (triangles) covering 0.29 < O:C < 1.33. To complete the picture, EDB measurements of DRH and ERH (crosses) of organic/AS/H_2O particles with 0.67 < O:C < 1.33 are also shown. To investigate the dependence of deliquescence and efflorescence of AS on the O:C ratio, we classify all available data of DRH and ERH into the O:C ranges of 0.20 - 0.60, 0.60 - 0.70, 0.70 - 0.80 and 0.80 - 1.40.

Prediction curves for ERH and DRH of mixed organic/AS/H_2O particles parameterized by Bertram et al. (2011) are given in Fig. 6.2 (grey and black lines) according to this classification. Presence and absence of LLPS are represented as solid and open symbols, respectively (see also Table 6.1).

In most mixtures covering O:C ratios from 0.20 to 0.60, LLPS occurred in the whole range of $0 < mf_d(AS) < 1$. AS effloresced in these phase-separated particles between 30.0 – 51.6 % RH (Fig. 6.2, panel (a1)). The highest ERH was observed for the systems that did not show LLPS (cyan circle, OAC+DCA3/AS/H_2O, O:C = 0.56 and dark blue circle, OAC2/AS/H_2O, O:C = 0.57). Upon moistening, the effloresced particles deliquesced at 78.9 ± 2.6 % RH (Fig. 6.2, panel (a2)). For 0.60 < O:C < 0.70, a clear dependence of ERH on the phase state of the particles can be seen (Fig. 6.2, panel (b1)). Systems consisting of Polyol+DCA2/AS/H_2O (yellow circle, O:C = 0.65), C6/AS/H_2O (olive triangle, O:C = 0.67), and MFC1/AS/H_2O (dark green circle, O:C = 0.67), which exhibited LLPS (solid symbols) in the entire range of $mf_d(AS)$, effloresced within values of 39.8 ± 4.8 % RH. However, for low AS fractions, AS ERH decreased significantly when the particle was present in a one-liquid-phase state as can be seen for the systems COM1/AS/H_2O (orange circle, O:C = 0.63), C5+C6+C7/AS/H_2O (green circle, O:C = 0.67), and COM2/AS/H_2O (purple circle, O:C = 0.68). Such a decrease is also observed for AS deliquescence in particles with 0.60 < O:C < 0.70 as shown in panel (b2) of Fig. 6.2. For 0.70 < O:C < 0.80, almost constant ERH = 43.0 ± 0.96 % and DRH = 76.6 ± 1.87 % was observed for the system Polyol+DCA1/AS/H_2O (yellow circle, O:C = 0.72) which led to complete LLPS (Fig. 6.2, panels (c1) and (c2)). However, a significant decrease of ERH and DRH occurred for organic-rich compositions of COM3/AS/H_2O (red circle, O:C = 0.70), and MFC2/AS/H_2O (purple circle, O:C = 0.79) systems, which were present in a one-liquid-phase state. A reason for the low ERH (29.7 %) and DRH (75.3 %) in the Polyol1/AS/H_2O system (orange circle, O:C = 0.71) at $mf_d(AS) = 0.33$ could be that the system at this composition is close to the boundary of the miscibility gap. In this case, most AS is mixed in the organic-rich phase and the volume of the AS-rich phase is very small. Systems with 0.80 < O:C < 1.4 exhibited no LLPS and showed the

largest decrease in ERH and even complete inhibition of AS efflorescence for low mf_d(AS) (Fig. 6.2, panels (d1) and (d2)). AS ERH in glutaric acid/AS/H_2O particles shows a wide spread from 29.5 to 57.5 % RH (Fig. 6.2, red cross and red triangles in panel (d1), see also Table 6.1) when results from different studies are compared. This spread is similar to the one observed for ERH of pure AS particles with diameters from 0.05 to 40 µm, which scattered between 31 and 48 % RH when results from different studies and measurement techniques such as EDB, optical microscopy, HTDMA, and FTIR are compared (Cohen et al., 1987; Xu et al., 1998; Han and Martin, 1999; Onasch, 1999; Badger et al., 2006; Pant et al., 2006; Parsons, 2006; Ciobanu et al., 2010). Ciobanu et al. (2009) have shown that efflorescence of AS particles that are deposited on a hydrophobic substrate preferentially starts from the particle surface or the substrate/particle contact line rather than in the volume of the particle. Discrepancies between AS ERH reported by different studies might therefore result from different surface properties and interactions with the substrate also in the case of mixed organic/AS/H_2O particles. For pure AS particles, ERH values above 40 % are suspected to occur due to heterogeneous impurities (Ciobanu et al., 2010). However, in the case of mixed particles, the high ERH values (> 48 %) of OAC+DCA3/AS/H_2O (cyan circle, O:C = 0.56), OAC2/AS/H_2O (dark blue circle, O:C = 0.57), and MFC2/AS/H_2O (purple circle, O:C = 0.79) shown in Fig. 6.2, panels (a1) and (c1), might be due to repulsive interactions between the ions of AS and the organic substances.

Overall, AS in mixed organic/AS/H_2O particles covering the O:C range of 0.29 - 1.33 deliquesced between 70 and 84 % RH and effloresced below 58 % RH or remained in a one-liquid-phase state. A more pronounced RH decrease was observed for AS efflorescence than for AS deliquescence. The decrease of ERH and DRH becomes more pronounced with decreasing AS mass fraction. The decrease in ERH may result from both thermodynamic and kinetic factors whereas the decrease in DRH is given by thermodynamics. Highly polar organic substances with high O:C may increase the solubility of AS in aqueous organic mixtures and thus decrease AS ERH and DRH (Marcolli et al., 2004a; Marcolli and Krieger, 2006). Moreover, high viscosity in organic-rich

particles may hinder the crystallization of AS (Krieger et al., 2012; Song et al., 2012a).

The parameterization of AS ERH as a function of organic-to-sulfate mass ratio and O:C by Bertram et al. (2009) is generally at the lower limit of the observed range of ERH in the mixed particles. It predicts almost no dependence of ERH on O:C for O:C < 0.7 and a drastic decrease for 0.7 < O:C < 0.8 and low organic-to-sulfate ratios. Such a dependence is in contrast to the experimental data in Fig. 6.2, which shows a rather gradual decrease of ERH with increasing O:C. Moreover, since this parameterization does not discriminate between liquid-liquid-phase-separated and one-liquid-phase systems it does not capture the low AS ERH of organic-rich particles with O:C < 0.7 that do not show LLPS.

6.4.2 Investigation of aerosol morphologies

6.4.2.1 Possible morphologies of tropospheric aerosols

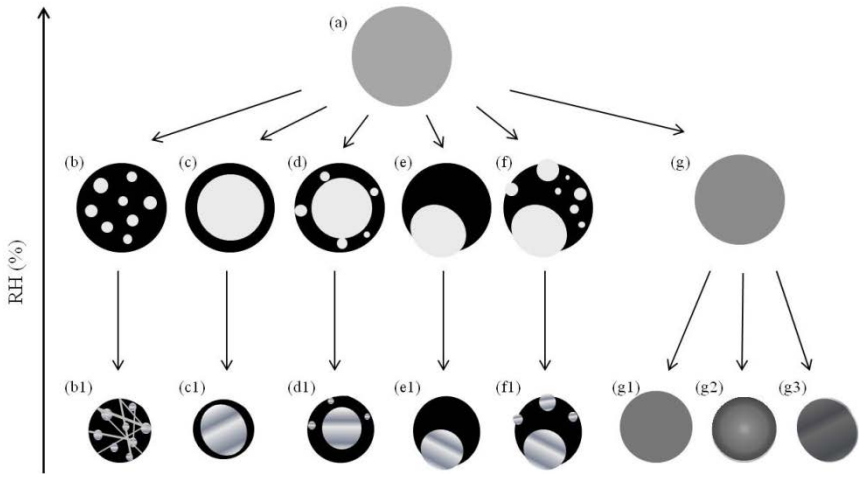

Figure 6.3 *Schematic diagram of possible morphologies of organic/AS/H_2O aerosol particles as a function of RH. Black: organic-rich phase, light grey: AS-rich phase, grey: mixed organic/AS phase. The following morphologies*

are expected: at high RH: (a) homogeneous droplet. Upon drying: (b) two liquid phases with aqueous AS inclusions in the organic-rich phase, (c) two liquid phases with a core-shell morphology, (d) two liquid phases with a core-shell morphology and additional AS inclusions, (e) two liquid phases with a partially engulfed configuration, (f) two liquid phases with a partially engulfed configuration and additional AS inclusions, and (g) a mixed liquid droplet. Further decrease in RH: (b1) crystalline AS phase with AS needles in the organic-rich liquid or glassy phase, (c1,d1,e1 and f1) crystalline AS phase surrounded by a liquid or a glassy organic-rich phase, (g1) mixed homogeneous droplet, (g2) mixed viscous droplet with concentration gradient, and (g3) crystallized particle with organic-rich phase in pores and veins.

Figure 6.3 illustrates the possible morphologies of tropospheric aerosol particles as a function of RH summarizing observations from literature (Ciobanu et al., 2009; Kwamena et al., 2010; Reid et al., 2011; Song et al., 2012a; Song et al., 2012b) and this study. Grey spheres represent mixed one phase droplets. Black and light grey colours stand for an aqueous organic-rich phase and an aqueous AS-rich phase, respectively, and the light grey lines and stripes represent crystallized AS. High RH leads to a mixed organic/AS/H_2O particle consisting of one liquid phase (grey sphere, a). As water is released, organic/AS/H_2O particles may undergo LLPS (b, c, d, e and f) for organic compositions with low O:C or remain as a homogeneous one-liquid-phase particle for high O:C (g). For compositions with high fractions of organics, LLPS occurs by nucleation and growth (Papon et al., 1999), resulting in a configuration of several small AS inclusions in an organic-rich phase (b). A further decrease in RH leads to crystallization of the AS inclusions and growth of AS needles (light grey lines) in the organic-rich phase (b1). The organic-rich phase is expected to remain in liquid state or turn glassy (Zobrist et al., 2008; Krieger et al., 2012). LLPS tends to occur by spinodal decomposition when organics and AS are present in similar fractions (Papon et al., 1999). Spinodal decomposition is followed by coalescence of the initially formed inclusions and may result in a core-shell morphology (c), a core-shell morphology with AS inclusions (d), a

partially engulfed configuration (e), or a partially engulfed configuration with AS inclusions (f) (Krieger et al., 2012; Song et al., 2012a). Because surface forces and the Kelvin effect become more important with decreasing size of the droplets and the AS inclusions, accumulation mode particles with LLPS are expected to be either present in core-shell or partially engulfed morphologies without any additional AS inclusions. This is supported by Ciobanu et al. (2009) who found a decreasing number of AS satellite inclusions for decreasing diameters of PEG-400/AS/H_2O particles. For particles with high fractions of AS, Ciobanu et al. (2009) and Song et al. (2012a) always observed a core-shell configuration (c) via 2nd phase formation from the surface of the particles. It depends on thermodynamic and kinetic factors whether AS effloresces at low RH. In droplets with LLPS, AS crystallization starts from the AS-rich phase and may proceed by the growth of needles into the organic-rich phase (b1, see also Fig. 6.1a). Effloresced droplets with core-shell and partially engulfed morphologies largely retain the morphology present before efflorescence (c1, d1, e1 and f1). Some satellite inclusions may disappear instead of crystallizing due to the diffusion of ammonium and sulfate ions to the crystallized regions of the particle (d → d1; f → f1). When homogeneous liquid particles effloresce (g → g3) the remaining liquid organic constituents may distribute in pores and veins and around the crystallized AS. Attractive interactions between organic functional groups and AS may suppress efflorescence in particles with a large organic fraction and high O:C (g1). AS crystallization may also be suppressed when particles become highly viscous or turn glassy at low RH (g1 and g2). Highly viscous particles may show concentration gradients (g2) instead of a homogeneous composition (g1) (Krieger et al., 2012).

6.4.2.2 Identification of droplet morphologies

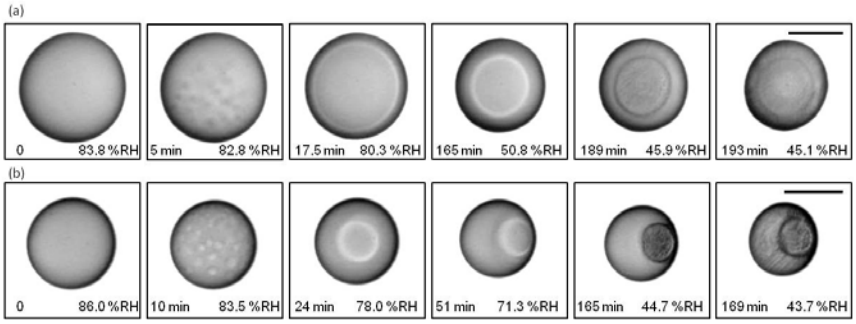

Figure 6.4 *Image sequence of LLPS and AS efflorescence leading to (a) core-shell morphology of COM1/AS/H_2O (O:C = 0.63, mf_d(AS) = 0.40) and (b) partially engulfed configuration of C6+C7/AS/H_2O (O:C = 0.61, mf_d(AS) = 0.33). Size bar: 20 µm.*

Table 6.1 summarizes the observed phases and phase changes of the organic/AS/H_2O systems investigated in this study together with the available literature data. Out of the 21 systems investigated in this study, eight systems did not show LLPS for all investigated organic-to-inorganic ratios, nine showed core-shell morphology and four showed both core-shell and partially engulfed configurations depending on the mass fraction of AS in the mixture and RH. Figure 6.4 exemplifies the process leading to core-shell configuration in COM1/AS/H_2O for mf_d(AS) = 0.40, and the partially engulfed morphology in C6+C7/AS/H_2O for mf_d(AS) = 0.33. Both systems underwent LLPS by spinodal decomposition. While the COM1/AS/H_2O particle showed LLPS at 82.8 % RH forming a core-shell configuration and effloresced at 45.9 % RH (Fig. 6.4a), the C6+C7/AS/H_2O particle exhibited LLPS at 83.5 % RH. Subsequently, the inner phase moved towards the edge of the particle between 78.0 and 71.3 % RH within 30 min leading to a partially engulfed morphology and remained in this configuration down to 44.7 % RH when AS effloresced (Fig. 6.4b).
Droplets that showed partially engulfed configurations all contained

dicarboxylic acids as the organic fraction. C6/AS/H_2O mixtures with mf_d(AS) = 0.50 and 0.67 showed a transition from core-shell to partially engulfed morphology in the RH range from 70 – 66 % and 63 – 50 %, respectively. For C7/AS/H_2O with mf_d(AS) = 0.34 and C5+C6+C7/AS/H_2O with mf_d(AS) = 0.5 spinodal decomposition directly led to a partially engulfed configuration at 88 % RH and 74 % RH, respectively.

6.4.2.3 Calculation of equilibrium configurations

Since the optical microscope gives only the top view of the droplets on the substrate, it is difficult to determine whether the AS inclusion contacts the droplet/air or the droplet/substrate interface or whether it is floating within the droplet volume. Therefore, Song et al. (2012a) performed confocal Raman scans through C6/AS/H_2O droplets revealing that the AS inclusion is at the bottom of the droplet. While the movement of the main AS inclusion from the middle to the edge of the particle is a clear indication of the transition from a core-shell to a partially engulfed configuration, it remains unclear whether an apparent core-shell morphology with the main AS inclusion in the middle of the droplet always fulfils the condition of complete wetting of the AS-rich phase by the organic-rich phase. If the top of the AS inclusion had direct contact to the gas phase, the top-view of the particle would be similar. Moreover, the hydrophobic glass slide might influence the droplet morphology. We therefore attempt to complement and confirm the optically observed morphologies by calculating the preferred morphology based on surface and interfacial tension measurements of the involved phases.

The spreading coefficient (S_i) gives an indication of the resulting equilibrium configuration of two immiscible liquid phases i and j within a gas phase k (Torza and Mason, 1970; Kwamena et al., 2010; Reid et al., 2011). It can be calculated when the surface (σ_{jk}, σ_{ik}) and interfacial tensions (σ_{ij}) are known:

$$S_i = \sigma_{jk} - (\sigma_{ij} + \sigma_{ik}) \quad (6.1)$$

Since the surface tension of the AS-rich phase (σ_{AS}) is larger than the

one of the organic-rich phase (σ_{org}), the aqueous AS-rich phase does not spread on the organic-rich phase. Therefore, the conceivable configurations are an organic-rich phase that fully (core-shell) or partially engulf the AS-rich phase. The conditions for a core-shell configuration and a partially engulfed configuration are given by Eq. 6.2 and Eq. 6.3, respectively:

$$\text{Core-shell configuration: } S_{org} = \sigma_{AS} - (\sigma_{org/AS} + \sigma_{org}) > 0 \quad (6.2)$$

$$\text{Partially engulfed configuration: } S_{org} = \sigma_{AS} - (\sigma_{org/AS} + \sigma_{org}) < 0 \quad (6.3)$$

It should be noted that this use of spreading coefficient is only strictly valid for phases of infinite volume where the surface and interfacial area changes can be approximated as the same. This may render morphology predictions less reliable in cases of finite volumes when the spreading coefficient is close to zero. Surface and interfacial tensions of solutions can be measured by standard methods such as the ring method (see Sect. 6.2). Because these methods need bulk volumes, measurements are restricted to samples that are not supersaturated with respect to any component. Since solution saturation of AS is reached at water activity, $a_w = 0.8$, LLPS has to be present for $a_w > 0.8$. Systems that fulfill these conditions are PEG-400/AS/H_2O, which always showed a core-shell morphology and C6+C7/AS/H_2O, which showed core-shell or partially engulfed configurations, depending on mf_d(AS) and RH (see Table 6.1). Interfacial and surface tensions were determined for the liquid-liquid-phase-separated systems prepared with $mf_d(AS) = 0.5$ and water contents leading to $a_w = 0.82$, 0,86, and 0.89 for PEG-400/AS/H_2O and $a_w = 0.85$ for C6+C7/AS/H_2O. Table 6.2 presents the measured surface and interfacial tensions, together with the calculated spreading coefficients and the observed morphologies.

For the investigated a_w range of 0.82 – 0.89, the surface tensions of the organic-rich phase of PEG-400/AS/H_2O vary between 42.1 – 42.7 mN m^{-1} with no clear dependence on a_w. These values are slightly lower than the surface tension of pure PEG-400 (this study: 44.32 mN m^{-1}; Ciobanu et al. (2009): 44.5 mN m^{-1}), probably due to a different arrangement of the PEG molecules on the surface of the solution.

Table 6.2 *Water activities (a_w), densities (at 293 K), surface and interfacial tensions of PEG-400/AS/H_2O (at 298 K) and C6+C7/AS/H_2O (at 293 K) of the upper organic-rich and lower AS-rich phases for $mf_d(AS)$ = 0.5. Spreading coefficients are calculated according to Eqs. 6.2 and 6.3. Observed morphology is given for indicated a_w.*

Mixture	a_w	Density (g cm^{-3})		Surface tension (mN m^{-1})		Interfacial tension (mN m^{-1})	Spreading coefficient (mN m^{-1})	Observed morphology
		organic-rich	AS-rich	organic-rich	AS-rich			
PEG-400/AS/H_2O	0.82	1.13	1.25	42.6 ±1.58	51.2 ±0.03	1.07	7.54	Core-shell
	0.86	1.12	1.21	42.1 ±0.79	52.6 ±0.42	0.46	9.97	
	0.89	1.12	1.19	42.7 ±0.89	52.2 ±1.07	0.08	9.43	
C6+C7/AS/H_2O	0.85 ±0.002	1.19	1.21	40.7 ±0.11	41.6 ±0.01	below detection limit	0.4-0.8	Core-shell

We therefore assume that a decrease of a_w will not lead to a further decrease of the surface tension. Surface tension in saturated AS solutions is increased by 20 % compared with the one of pure water (71.99 mN m^{-1}) (Song et al., 2012a). However, the surface tension of the AS-rich phase of PEG-400/AS/H_2O shows a strong decrease to values between 51.2 – 52.6 mN m^{-1} in the investigated a_w range of 0.82 – 0.89, indicating that small amounts of PEG-400 are present in the AS-rich phase and enriched on the surface. Interfacial tensions between the organic-rich and the AS-rich phase are low (0.08 – 1.07 mN m^{-1}) but show a clear tendency to larger values with decreasing a_w. Such an increase of interfacial tension with decreasing water content has also been observed by Wu et al. (1996) for PEG-1000/AS/H_2O, PEG-2000/AS/H_2O, and PEG-4000/AS/H_2O systems and can be rationalized by considering that the concentration of water as the common component is getting less and the two liquid phases become more dissimilar when a_w decreases. The spreading coefficient calculated from these interfacial and surface tension values is clearly positive (7.5 – 10 mN m^{-1}), indicating a core-shell morphology as the thermodynamically favored configuration,

which is in accordance with the optical appearance of the phase-separated droplets of this system on the hydrophobic substrate. If one assumes constant surface tensions of the two liquid phases and an increase of the interfacial tension of 1 – 2 mN m^{-1} for a decrease of a_w of 0.1, the spreading coefficient would be ~ 0 mN m^{-1} when $a_w \approx$ ERH. A movement of the main AS inclusion to the edge of the particle has not been observed for this system, indicating that the core-shell morphology remains energetically favored. However, it cannot be totally excluded that high viscosity of the organic-rich phase at low RH inhibits the movement of the AS inclusion within the droplet (Ciobanu et al., 2009) and that a partially engulfed configuration is realized by incomplete wetting of the top of the AS inclusion by the organic-rich phase.

For the system C6+C7/AS/H_2O the surface tension of the organic-rich phase (40.7 mN m^{-1}) at a_w = 0.85 is below the range estimated by Topping et al. (2007) for the surface tension of adipic acid (straight chain C6 dicarboxylic acid) in the supercooled liquid state (45 – 52 mN m^{-1}). Surprisingly, the surface tension of the AS-rich phase is also reduced to a similarly low value (41.6 mN m^{-1}). The interfacial tension of this system at a_w = 0.85 was too low to be measured. We therefore assume a value between 0.1 – 0.5 mN m^{-1}, which is just below the detection limit of the ring method (< 0.5 mN m^{-1}). This assumption leads to a positive spreading coefficient of the investigated mixture, which is in accordance with the observed core-shell morphology of the droplet deposited on the hydrophobic substrate. If we assume an increase of the interfacial tension and constant surface tensions of the liquid phases with decreasing a_w – as it is the case for the PEG-400/AS/H_2O system – a transition from core-shell to partially engulfed morphology should occur when droplets of C6+C7/AS/H_2O are exposed to decreasing RH. Such a transition is indeed observed between 78.0 % RH and 71.3 % RH in the C6+C7/AS/H_2O mixture for mf_d(AS) = 0.33. We therefore assume that the interfacial tension reaches a critical value where the spreading coefficient of the organic-rich phase changes sign from a positive to a negative value indicating that a partially engulfed configuration becomes energetically favored. Several systems with dicarboxylic acids as the organic fraction exhibited a partially engulfed configuration. We therefore consider the surface and interfacial tension values measured for

C6+C7/AS/H_2O as typical for these systems.
The comparison of the optically observed morphology of liquid-liquid-phase-separated droplets and calculated spreading coefficients shows that the movement of the main AS inclusion from the middle to the edge of a droplet deposited on a hydrophobic substrate is indicative for the transition from a core-shell to a partially engulfed configuration. The presence of the main AS inclusion in the middle of the droplet should therefore be a good indicator for a core-shell configuration as the energetically favored one. This conclusion is certainly valid at intermediate and high RH when the viscosity of the organic-rich phase is low enough to allow movement of the AS inclusion within the droplet. In case of highly viscous particles at low RH, the energetically favored configuration may not be realized or LLPS might even be totally impeded (Ciobanu et al., 2009). If an airborne particle with core-shell morphology is exposed to decreasing RH, it might therefore remain in a core-shell configuration because of kinetic restraints.

6.4.2.4 LLPS and morphology of single levitated aerosol particles

To investigate whether the contact to the substrate in optical microscope experiments influences the onset relative humidity of LLPS (SRH), the relative humidity range of the phase transition and – most important – the morphology of the phase separated aerosol, we performed measurements on single, levitated aerosol particles. We chose two systems for the comparison with bulk predictions (see 6.4.2.3) and the optical microscope experiments (see 6.4.2.2): PEG-400/AS/H_2O and C6/AS/H_2O both with mf_d(AS) = 0.5. Both optical microscopy and bulk measurements of interfacial tensions show that the morphology of the phase separated particle is core-shell for the PEG-400/AS/H_2O system over the entire RH range below SRH and above ERH, while a transition from core-shell morphology to partially engulfed morphology occurs below SRH for the C6/AS/H_2O system.
The experiments in the electrodynamic balance were performed at 291 K on at least three different particles with radii between 7 and 15 µm at 91 % RH. The particles were exposed to cyclic changes in RH to pass through the LLPS transition but typically avoiding efflorescence.

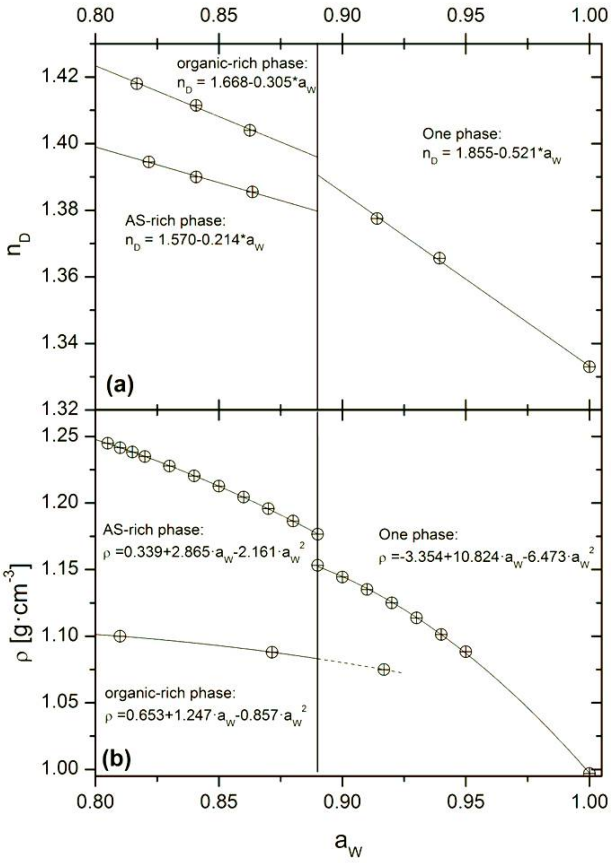

Figure 6.5 *Panel (a) shows refractive index data, n_D, measured in bulk samples for solute concentrations with one phase and for the two phases at concentrations lower than the one where LLPS occurs. Linear fits for the refractive indices in terms of aw are provided in the figure. Panel (b) shows density data. We use density data of the binary PEG/H_2O solution and for the binary AS/H_2O solution to represent densities of the organic-rich and the AS-rich phases, respectively. We believe these are good approximations, since the AS-rich phase contains little PEG and the organic-rich phase little AS. Polynomial fits for density are provided as well.*

For the PEG-400/AS/H_2O system thermodynamic data (a_w and volume fraction of the two phases) were determined previously (Marcolli and Krieger, 2006). In order to compute Mie resonance spectra for different morphologies, additional data for the densities and refractive indices of the involved aqueous solutions were required. Figure 6.5 shows the results and gives the parameterizations in terms of a_w. We also used the data of Marcolli and Krieger (2006) to parameterize the mass fraction of solute (mf_s) in terms of a_w as: $mf_s = \frac{(1-a_W)^a}{1+b\cdot a_W+c\cdot {a_W}^2}; 1 > a_W > 0.8$ (a = 0.818, b = - 0.517, c = - 0.0995), and the volume ratio, VR = (volume of PEG-rich phase)/(volume AS-rich phase) as $V_R = 1.173 - 0.432 \cdot a_W$.
With these data available we can compare measured Mie resonance spectra with computed ones. For the computations, we use the Mie scattering codes provided by Mätzler (2002) for homogeneous spheres, Pena and Pal (2009) for those of spherical symmetric core-shell morphology and that of Ngo et al. (1996) for core-shell particles with a nonconcentric core.

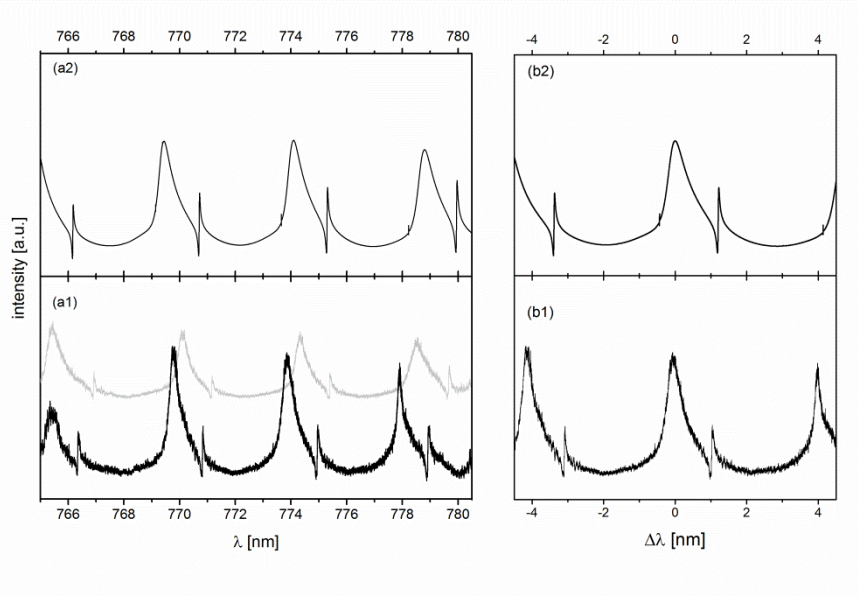

Figure 6.6 *Comparison of measured Mie resonance spectra (TE-polarization) with computed spectra at RH = 93.5 %, T = 291 K. Panel (a1) shows two consecutively measured Mie resonance spectra, 7 minutes apart at nominally 93.58 % RH (grey) and 93.54 % RH (black). Panel (a2) shows the computed Mie spectrum for* a_w *= 0.9354 using a standard Mie code and the parameterizations as detailed above. Panels (b1) and (b2) show the same spectra but centered relative to the central peak of panel (a1) and (a2).*

Figure 6.6 shows such a comparison for a particle significantly above SRH, i.e. the morphology of the particle is a homogeneous liquid. Let us first note that tiny changes in RH (e.g. nominally 0.04 %) at high humidities, with the associated large growth factors, lead to a significant shift in the resonance spectra; cf. the grey and black spectrum in panel (a1) of Fig. 6.6. This also means that small fluctuations of RH during a single scan will lead to a significant relative shift between the resonance peaks. For calculating Mie resonance spectra, a_w has to be known accurately but the uncertainty in our RH measurements is ± 1.5 %. In addition the parameterizations given above lead to uncertainties in the parameters needed to compute Mie resonance spectra. Hence a comparison with computed spectra should be based on the shape and occurrence of spectral features rather than absolute resonance positions. Accordingly we compare the computed spectrum relative to the central peak (panel (b2) of Fig. 6.6) with the measured spectrum in panel (b1) of Fig. 6.6. The only free parameter in the computation is the size of the particle, which was fixed by evaluating a series of spectra at 90.5 % RH. The satisfactory agreement between modeled and computed spectrum shows that our parameterizations based on bulk measurements can be successfully applied to levitated aerosol particles at least if the particle is homogeneous.

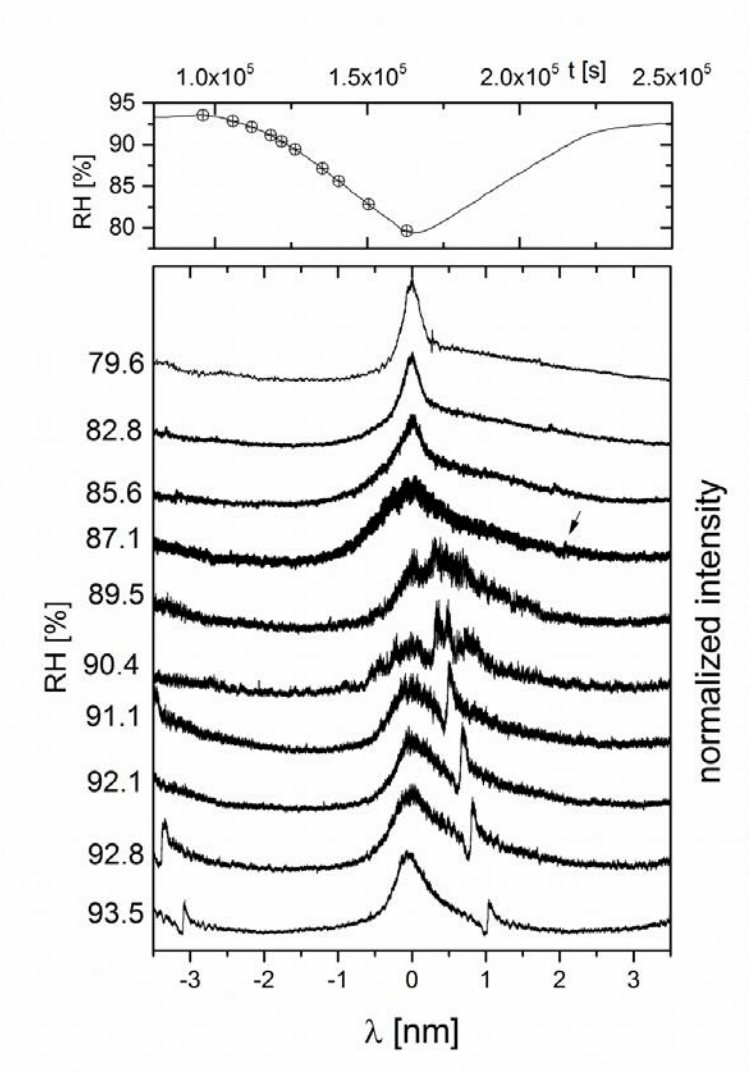

Figure 6.7 *Series of Mie resonance spectra (TE-polarization) upon slow drying from 93.5 % RH to 79.6 % RH. The scattered intensity is normalized to the maximum intensity in the spectra, the wavelength scale is relative to the peak center, for clarity spectra are shifted vertically to each other. The upper panel shows the change in RH with time. The symbols mark the times and humidities at which the spectra in the lower panel were recorded.*

In Fig. 6.7 we show a series of spectra at different RH passing through the LLPS upon drying. We attribute the disappearance of the sharp resonance at about +0.5 nm relative to the central peak at 90.4 % RH together with a general increase in noisy features in the spectrum to the onset of LLPS. This onset RH is slightly higher but agrees within the error of our RH sensor with the one determined from bulk measurements (SRH = 89.2 %, Marcolli and Krieger (2006)) and the one determined using optical microscopy (SRH = 89.7 %, Ciobanu et al. (2009)). It is interesting to note that it takes almost 4 hours slowly drying to about 87.1 % RH until the noisy features reduce and a very small but sharp resonance appears at about +2.0 nm relative to the central peak (marked by an arrow in Fig. 6.7). Upon further drying the noise is further reduced, but the general spectral features are largely unchanged. When comparing these findings with the optical microscopic observations of Ciobanu et al. (2009) we speculate that this end of the transition marks the coalescence of satellite inclusions of the AS-rich phase with a central core AS-rich phase in the particle. This speculation is supported by the corresponding spectra upon subsequent humidification (Fig. 6.8).

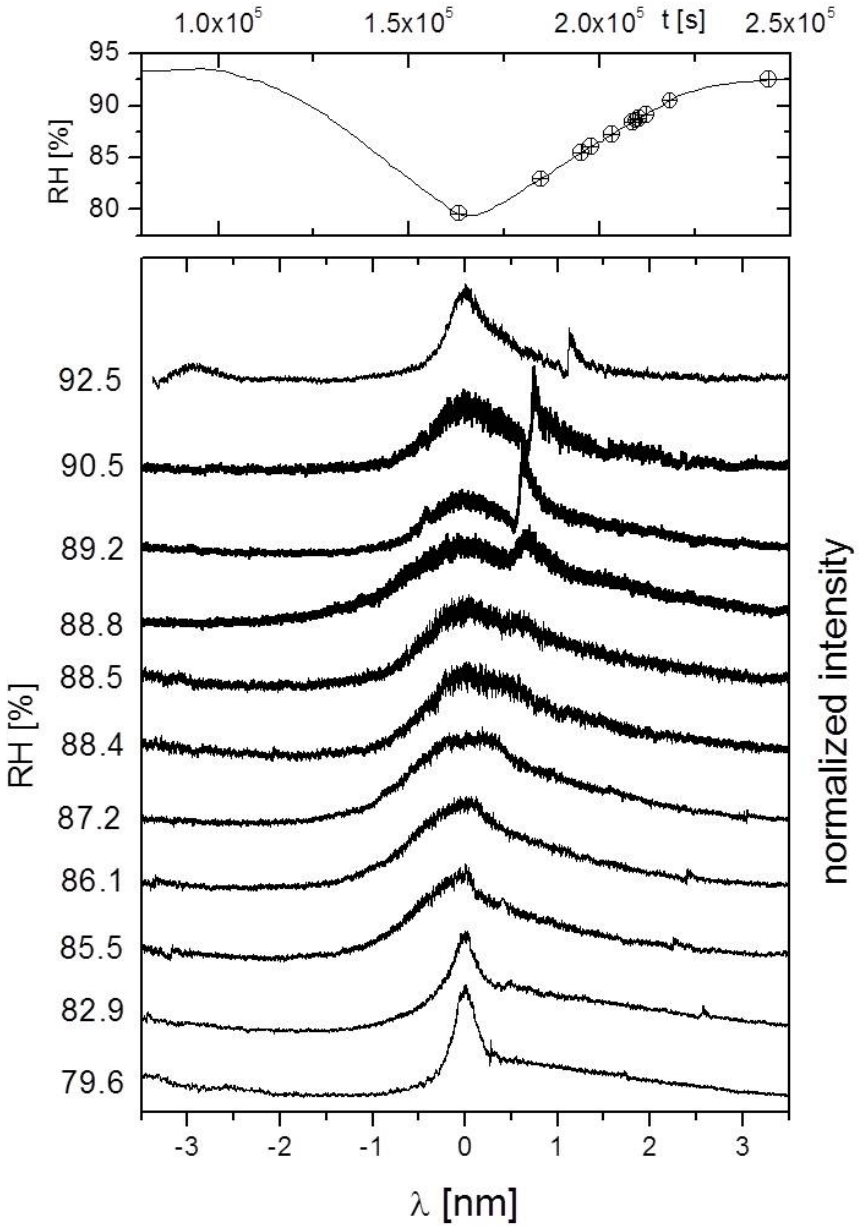

Figure 6.8 *Series of Mie resonance spectra (TE-polarization) upon humidification cf. Fig. 6.7.*

We observe a clear reverse transition (note the disappearance of the very small, but sharp resonance about +2.5 nm relative to the central peak), but now the transition is much narrower in terms of the RH-range and time, namely between about 88.4 % and 88.8 % RH and about half an hour. The transition RH is slightly lower but within error the same as observed upon drying and in agreement with bulk and optical microscope experiments. We attribute the reduction in RH range for the transition from ΔRH ~3.3% upon drying to ΔRH ~0.4% upon humidification to the fact that coalescence of satellite inclusions occurs only when drying.

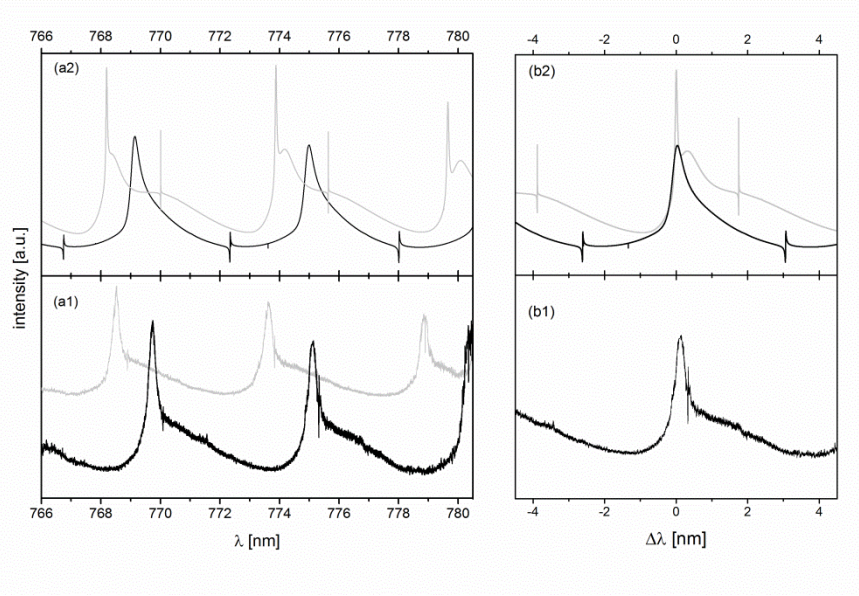

Figure 6.9 *Comparison of measured with computed spectra (TE-polarization) as in Fig. 6.6, but at RH = 80.9 %, in the LLPS regime. Panel (a1) shows two subsequent spectra at RH=80.9 % (black line) and RH= 80.7 % (grey line). The computed spectra in panels (a2) and (b2) are calculated for RH = 80.9 % assuming a homogeneous droplet (grey line) and assuming a spherical symmetric core-shell morphology (black line, code of Pena and Pal (2009)). Panels (b1) and (b2) show the same spectra*

but centered relative to the central peak of the spectra at 80.9 % RH of panel (a1) and (a2).

We compare the Mie resonance spectra (TE-polarization) at about 81 % RH, significantly below SRH, to computed spectra for different morphologies in Fig. 6.9. First, note that at 81 % RH a change of 0.2 % in RH leads to roughly the same shift in the Mie Resonance spectra as does a shift of ΔRH = 0.04 % at 93.5 %. This is due to the significantly lower slope in the growth factor at lower humidity. Hence fluctuations in RH become less important at lower humidity. The uncertainty in the parameters needed for the Mie computations suggest that one should focus on the shape of the resonances rather than their absolute peak position. Therefore, the better agreement of peak position of the measured spectrum (black line) with the one computed for core-shell morphology may be accidental. If we compare the resonance shape of the broader resonance in panels (b1) and (b2) the agreement between measured and calculated spectrum is considerably better for the one with the core-shell morphology. We not only calculated Mie resonance spectra of spherical symmetric core-shell morphology, but also computed spectra with the core located off centre using the code of Ngo et al. (1996) The shape of the broader resonances does not change when the core is no longer in the centre of the droplet, but the location of the sharpest resonances shift, especially if the core is located at the outer edge of the particle. Note that the sharp resonance close to the central peak of the measured spectrum is not present in both of the computed spectra. When comparing measured with computed spectra at much lower humidity (RH=41.3%), close to the efflorescence humidity, we were not able to reproduce the measured spectra closely. While the spectra (see Fig. 6.10) exhibited consistent resonance features, including sharp resonances, all computed spectra look significantly different.

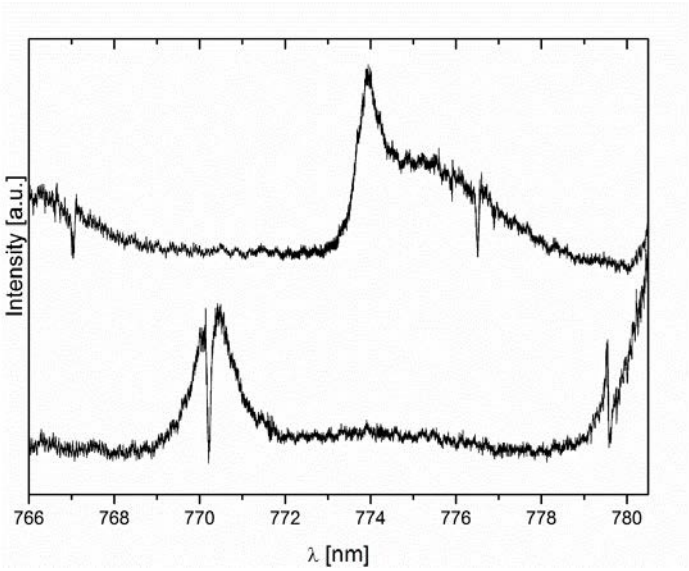

Figure 6.10 *Resonance spectra (lower trace TM-polarization, upper trace TE-polarization) of a second particle of the PEG-400/AS/H_2O system at low humidity (RH = 41.3 %).*

We varied size, volume ratio, refractive index and location of the core relative to the centre of the droplet (using the code of Ngo et al. (1996)), but were not able to reproduce the measured spectra closely. At present we do not have any explanation for this disagreement, but suggest that further experiments with particles with varying total size may help to understand these differences. Nevertheless, we conclude that the particle exhibits core-shell morphology when phase separated in agreement with both predictions from bulk measurements of interfacial tensions and optical microscope images. We exclude partially engulfed morphology because spectra of particles with this morphology appear distinctly different (see Fig. 6.11 and discussion below).

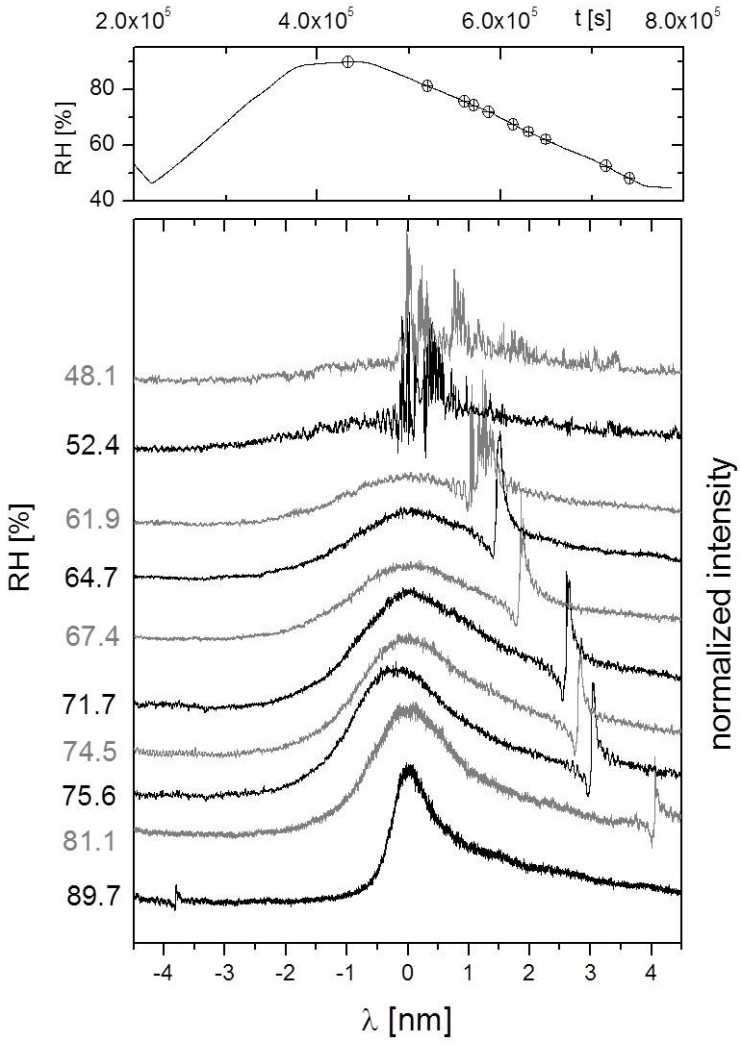

Figure 6.11 *Series of subsequent Mie resonance spectra (TE-polarization) recorded upon drying a particle of the C6/AS/H_2O system, analogous to Figs. 6.8 and 6.7.*

To compare Mie resonance spectra of a system for which we expect core-shell morphology to one for which we expect a transition from core-shell to partially engulfed morphology, we also investigated the

C6/AS/H_2O system. A series of subsequent spectra upon drying are shown in Fig. 6.11. There is a continuous shift of the sharp resonance observed at initially (RH = 89.7%) +6.3 nm (not shown) towards the central, broader peak upon drying. At 61.9 % RH the sharp resonance becomes noisy and its spectral position scatters when recording the spectra in time. This noise increases further upon drying with only a broad noisy resonance being observed at RH around 50 %. Subsequent drying cycles and repeated experiments with different particles showed always this pattern in the Mie resonance spectra with the described transition occurring between 65.6 % RH and 61.9 % RH. Upon humidifying the transition back to non-distorted spectra occurred at slightly higher RH around 66 %.

According to our optical microscope experiments the onset RH of LLPS is 73.4 %. No sudden changes in the Mie resonance spectra occurred around this humidity, probably indicating that the transition from homogeneous to core-shell morphology is fast and not accompanied over a broader humidity range with deviations of spherical symmetry. A comparison with computed spectra, which could reveal the transition, is difficult because the supportive data needed to perform such a calculation is lacking. The transition happens below the deliquescence humidity of AS, making bulk measurements of the needed parameters, like density, refractive index and volume ratio impossible.

The transition to partially engulfed morphology occurred at 67.2 % RH in the optical microscope experiments, slightly higher than the transition we observe with the levitated particle. However, the agreement is close enough to attribute the appearance of significant noise in the spectra of Fig. 6.11 to the transition from core-shell morphology to partially engulfed morphology. Also, the increase of the noise upon further drying supports this interpretation, since the deviation from spherical symmetry will become more pronounced with decreasing volume fraction of the AS-rich phase. Since the particle performs rotational Brownian motion when trapped in the EDB (Krieger and Zardini, 2008) and the position of the resonances for a non-spherical particle depends on scattering angle, the scattered intensity depends on wavelength and time, so that during slow scanning of the laser wavelength several resonances will be recorded closely spaced in time, which result then in a noisy spectrum in

wavelength space. This is also consistent with the observations of Reid et al. (2011) that sharp whispering gallery mode resonances in stimulated Raman spectra are suppressed for particles with partially engulfed morphology. Let us note at the side, that in one particular experiment we observed a further transition back to core-shell morphology occurring at RH = 56 %.

6.5 Conclusion

In this study, we analyzed and evaluated phases, phase transitions and morphologies of 33 organic/AS/H_2O systems investigated in this work and literature. The organic fractions of these systems consist of one to ten aliphatic and/or aromatic oxidized compounds with carboxylic acid, hydroxyl, carbonyl, ether, and ester functionalities and cover the O:C range from 0.29 to 1.33. Thirteen out of these 33 systems did not show LLPS for all studied organic-to-inorganic mixing ratios, sixteen showed core-shell morphology when present in a two-liquid-phases state and four showed both core-shell and partially engulfed configurations depending on the organic-to-inorganic ratio and RH. The organic fractions of the systems with partially engulfed configurations consisted in all cases of dicarboxylic acids. In some of these systems partially engulfed configuration was established immediately when LLPS occurred, other systems showed a transition from core-shell to partially engulfed configuration when RH was decreased. AS in mixed organic/AS/H_2O particles deliquesced between 70 and 84 % RH and effloresced below 58 % RH or remained in a one-liquid-phase state when all mixtures are considered. AS in droplets with LLPS always effloresced between 30 and 50 % RH and deliquesced between 70 and 84 % RH. The decrease of ERH and DRH became more pronounced with decreasing AS mass fraction and may be caused by an increased solubility of AS in the presence of highly polar organic substances or crystallization inhibition in highly viscous particles. These results clearly show that the presence or absence of LLPS influences AS efflorescence.

Whether aerosol particles consisting of two liquid phases show core-shell or partially engulfed morphologies depends on the balance of

surface and interfacial tensions, which determine the spreading of the immiscible liquid phases on each other. The calculation of spreading coefficients for the systems PEG-400/AS/H_2O and C6+C7/AS/H_2O confirmed that the movement of an AS inclusion from the middle to the edge of a droplet deposited on a hydrophobic substrate is indicative for the transition from a core-shell to a partially engulfed configuration. Interestingly, the surface tension of the AS-rich phase is strongly reduced compared with a pure aqueous AS solution and seems to depend more on the nature of the organic solutes than on the inorganic salt. The interfacial tensions between the organic-rich and the AS-rich phase are very low at the onset of LLPS and show a clear tendency to larger values with decreasing RH. A transition from core-shell to partially engulfed configuration with decreasing RH seems therefore to be triggered by this quantity. Analysis of high resolution elastic Mie resonance spectra allowed the detection of LLPS for single levitated droplets consisting of PEG-400/AS/H_2O. Mie spectra measured at 93.5 % and at 80.9 % RH agreed with computed Mie spectra for a homogeneous and a core-shell configuration, respectively, confirming the results obtained from droplets deposited on a hydrophobic substrate. While the transition from a homogeneous particle to a core-shell configuration was not detected unambiguously in the C6/AS/H_2O system, the transition from core-shell to partially engulfed morphology could be clearly seen.

Based on the experimental evidence presented in this work, we consider the core-shell morphology as the prevalent configuration in organic/AS/H_2O particles in the atmosphere. This conclusion seems to be in conflict with Reid et al. (2011) who postulated a predominance of partially engulfed structures. However, this apparent disagreement might be resolved considering that the analysis by Reid et al. (2011) relies on systems with NaCl as the inorganic component and organic compounds that show LLPS also in the absence of an inorganic salt. Such hydrophobic substances are however not typical for the organic fraction in ambient aerosols. Further studies are needed to investigate how sensitively phase transitions and morphology of mixed organic/inorganic particles depend on the chemical composition of the inorganic fraction, temperature and particle size.

Acknowledgements

This work was supported by the Swiss National Foundation Project No. 200020-125151 and the ETH Research Grant ETH-0210-1.

Chapter 7

Final remarks

7.1 Summary and conclusion

In this PhD work, the phase transitions and morphologies of internally mixed organic/AS/H_2O particles during humidity cycles have been investigated at 293 K. The study of single particles allows for the investigation of miscibility gaps in solutions that are supersaturated with respect to a crystalline species and, hence, not accessible to bulk measurements. It also allows studying particle morphologies. Laboratory experiments of single aerosol particles are thus essential to improve our understanding of aerosol properties and processes on the single particle level.

The main scientific questions of this PhD thesis were:

- Can the O:C ratio be considered as the key parameter to predict the occurrence of LLPS in organic/AS/H_2O particles? (Chapters 4 and 5)
- Does in addition to the O:C ratio also the specific functional group composition influence the occurrence of LLPS? (Chapter 5)
- Does the number of components influence the occurrence of LLPS in organic/AS/H_2O mixtures? (Chapter 5)
- Does the spread of O:C ratios of the individual organic components present in a mixture influence the occurrence of LLPS? (Chapter 5)
- Does LLPS influence the deliquescence and efflorescence of AS in mixed organic/AS/H_2O particles? (Chapter 6)
- What are the morphologies of particles consisting of the investigated model mixtures depending on RH conditions? (Chapters 4 and 6)

- What is the prevalent morphology in the mixed organic/AS/H_2O particle consisting of two liquid phases in the atmosphere? (Chapter 6)

In order to answer these questions, we subjected aerosol particles deposited on a hydrophobically coated substrate to RH cycles, and observed the phase transitions and the morphologies using optical microscopy and Raman spectroscopy. To explore the phase diagram, we mixed the components in different organic-to-inorganic dry mass ratios (OIR).

We found the following answers to the above questions based on these laboratory experiments:

- *Micrometer-sized particles of C5/AS/H_2O, C6/AS/H_2O, and C7/AS/H_2O showed significantly different phase transition behavior*. (Chapter 4)

  While the C5/AS/H_2O particles showed no LLPS with OIR = 2:1, 1:1, and 1:4, the C6/AS/H_2O and C7/AS/H_2O particles exhibit LLPS upon drying at RH between 50 % and 85 % and at ~ 90 %, respectively, depending on the OIR.

- *LLPS occurred within the range of O:C < 0.7 in DCA/AS/H_2O aerosols*. (Chapter 4)

  O:C ratio of the organic aerosol fraction may be a good predictor for the presence of LLPS in tropospheric aerosol particles because it reflects the polarity of organic compounds and their miscibility with water and electrolytes.

- *LLPS always occurred for O:C < 0.56, never occurred for O:C > 0.80, and depended on the specific types and compositions of*

organic functional groups in the regime 0.56 < O:C < 0.80. (Chapter 5)

Various organic mixtures were compared, comprising hydroxyl functionalities, dicarboxylic acids containing 5, 6 or 7 carbon atoms, oxidized aromatic compounds, and a mixture with multifunctional compounds including ring structures and double bonds. In the intermediate regime 0.56 < O:C < 0.80, the mixtures with a high share of aromatic compounds shifted the limit of occurrence of LLPS to lower O:C ratios.

· *Complexity of the mixture in terms of component number and the spread of O:C of the components did not notably influence the conditions for LLPS to occur.* (Chapter 5)

The range in O:C with regard to the occurrence of LLPS of the most complex mixture investigated consisting of 10 organic components with O:C of components ranging from 0.30 – 1.33 is in agreement with the ones of the simpler systems. In addition, we compared three model systems with dicarboxylic acids as the organic fraction: C6/AS/H_2O (O:C = 0.67) consisting of three dicarboxylic acids each with O:C = 0.67, (C5+C6+C7)/AS/H_2O (O:C = 0.67) consisting of nine dicarboxylic acids with a spread of O:C from 0.57 – 0.80, and COM/AS/H_2O (O:C = 0.63) containing 10 components with more variety of compounds and a spread of O:C from 0.30 – 1.25. These three mixtures exhibit SRH in a similar range, namely at 73 – 74 % (C6/AS/H_2O), 70 – 74 % (C5+C6+C7/AS/H_2O), and 72 – 85 % (COM1/AS/H_2O) for the investigated OIR.

· *A strong reduction or complete inhibition of AS efflorescence occurred for mixtures that did not exhibit LLPS.* (Chapter 6)

The decrease of ERH and DRH became more pronounced with decreasing AS mass fraction and may be caused by an increased solubility of AS in the presence of highly polar organic substances or crystallization inhibition in highly viscous particles. These results

clearly show that the presence or absence of LLPS influences AS efflorescence.

· *Core-shell structures and partially engulfed structures were observed in DCA/AS/H_2O particles on a hydrophobically coated substrate*. (Chapter 4)

Partially engulfed configuration was observed in the C6/AS/H_2O system for OIR = 1:1 and 1:2 while both partial (OIR = 2:1) and complete engulfed (OIR = 1:1) configurations occurred in the C7/AS/H_2O system, suggesting that such morphologies might also exist in tropospheric aerosols.

· *Core-shell morphology was prevalent in organic/AS/H_2O particles deposited on a hydrophobically coated substrate when LLPS occurred*. (Chapter 6)

Thirteen out of 33 systems from this work and literature did not show LLPS for all studied OIR, sixteen showed core-shell morphology when present in a two-liquid-phases state and four showed both core-shell and partially engulfed configurations depending on OIR and RH. The ones that exhibited core-shell morphology all contained dicarboxylic acids as the organic fraction.

· *Core-shell morphology might be very likely the prevalent configuration in the troposphere*. (Chapter 6)

Spreading coefficients of the organic-rich phase on the AS-rich phase for PEG-400/AS/H_2O and C6+C7/AS/H_2O proved to be in agreement with the optically observed morphologies of droplets on the hydrophobic substrate. In addition, the high resolution elastic Mie resonance spectra of single levitated droplets consisting of PEG-400/AS/H_2O and C6/AS/H_2O differed distinctively for homogeneous, core-shell and partially engulfed configuration, confirming the results obtained from droplets deposited on the hydrophobic substrate.

7.2 Outlook

By performing laboratory experiments with particles consisting of AS, water and organic mixtures of atmospheric relevance, we have shown that LLPS might be a common feature in mixed organic/AS/H_2O particles in the atmosphere. In this work, AS represented the inorganic fraction. Considering inorganic constituents of tropospheric aerosols, model systems with other inorganic compositions such as NH_4NO_3, NH_4HSO_4, and NaCl which are also abundant inorganic salts in the atmosphere have different characteristics for hygroscopicity and interactions with the organic components. They should be investigated to explore how the variability of the inorganic fraction influences ERH and DRH of aerosol particles and the occurrence of LLPS. The presence of LLPS affects the gas-particle partitioning of semivolatile compounds and water (Zuend and Seinfeld, 2012), and it influences efflorescence and deliquescence of the inorganic components compared to assuming completely mixed particles. Moreover, to gain definitive conclusions for the phase and phase transitions of atmospheric aerosol particle, the results obtained from this study should be directly compared to ambient aerosol samples. Recently, ambient aerosol samples from Atlanta and Amazon were collected onto filters to investigate the physical states and chemical compositions of the aerosols (Pöhlker et al., 2012; You et al., 2012). It turned out that LLPS in the ambient aerosols was present for O:C $\leq$ 0.5 in agreement with the O:C ranges of LLPS specified by Song et al. (2012b). Further investigations of real aerosols from various locations are needed to show how well occurrence of LLPS obtained from laboratory studies applies to natural samples. Furthermore, the morphologies of ambient aerosol should be analyzed and used to explore their influence on heterogeneous chemistry. A core-shell configuration will have more drastic consequences for heterogeneous chemistry and hygroscopicity than a partially engulfed configuration because the aqueous inorganic-rich phase will be totally enclosed by a probably highly viscous organic coating with low diffusivity for reactants and water. E.g., atmospheric chemistry related to the N_2O_5 heterogeneous hydrolysis onto organic coated aerosol particles is strongly influenced by particle morphology (Folkers et al., 2003; Anttila

et al., 2006: McNeill et al., 2006; Anttila et al., 2007; Cosman et al., 2008; Riemer et al., 2009: You et al., 2012). Low diffusivities in the organic-rich coating may hinder gas-particle partitioning of semivolatile species and water, conserving thermodynamic non-equilibrium states.

List of Figures

List of Tables

Bibliography

Abbatt, J. P. D., K. Broekhuizen, and P. P. Kumar (2005), Cloud condensation nucleus activity of internally mixed ammonium sulfate/organic acid aerosol particles, Atmos. Environ., 39(26), 4767-4778.

Aiken, A. C., P. F. DeCarlo, and J. L. Jimenez (2007), Elemental analysis of organic species with electron ionization high-resolution mass spectrometry, Anal. Chem., 79(21), 8350-8358.

Aiken, A. C., et al. (2008), O/C and OM/OC ratios of primary, secondary, and ambient organic aerosols with high-resolution time-of-flight aerosol mass spectrometry, Environ. Sci. Technol., 42(12), 4478-4485.

Alves, C., A. Carvalho, and C. Pio (2002), Mass balance of organic carbon fractions in atmospheric aerosols, J. Geophys. Res.-Atmos., 107(D21), doi:10.1029/2001JD000616.

Anttila, T., A. Kiendler-Scharr, R. Tillmann, and T. F. Mentel (2006), On the reactive uptake of gaseous compounds by organic-coated aqueous aerosols: Theoretical analysis and application to the heterogeneous hydrolysis of N2O5, J. Phys. Chem. A, 110(35), 10435-10443.

Anttila, T., A. Kiendler-Scharr, T. F. Mentel, and R. Tillmann (2007), Size dependent partitioning of organic material: evidence for the formation of organic coatings on aqueous aerosols, J. Atmos. Chem., 57(3), 215-237.

Backes, H. M., J. M. Jing, E. Bender, and G. Maurer (1990), Interfacial-Tensions in Binary and Ternary Liquid Liquid-Systems, Chem. Eng. Sci., 45(1), 275-286.

Badger, C. L., I. George, P. T. Griffiths, C. F. Braban, R. A. Cox, and J. P. D. Abbatt (2006), Phase transitions and hygroscopic growth of aerosol particles containing humic acid and mixtures of humic acid and ammonium sulphate, Atmos. Chem. Phys., 6, 755-768.

Ben-Hamo, M., A. Apelblat, and E. Manzurola (2007), Volumetric properties of aqueous solutions of glutaric acid, J. Chem. Thermodyn., 39(7), 1071-1076.

Bertram, A. K., S. T. Martin, S. J. Hanna, M. L. Smith, A. Bodsworth, Q. Chen, M. Kuwata, A. Liu, Y. You, and S. R. Zorn (2011), Predicting the relative humidities of liquid-liquid phase separation, efflorescence, and deliquescence of mixed particles of ammonium sulfate, organic material, and water using the organic-to-sulfate mass ratio of the particle and the oxygen-to-carbon elemental ratio of the organic component, Atmos. Chem. Phys., 11(21), 10995-11006.

Biskos, G., L. M. Russell, P. R. Buseck, and S. T. Martin (2006), Nanosize effect on the hygroscopic growth factor of aerosol particles, Geophys. Res. Lett., 33(7), doi:10.1029/2005GL025199.

Bodsworth, A., B. Zobrist, and A. K. Bertram (2010), Inhibition of efflorescence in mixed organic-inorganic particles at temperatures less than 250 K, Phys. Chem. Chem. Phys., 12(38), 12259-12266.

Booth, A. M., D. O. Topping, G. McFiggans, and C. J. Percival (2009), Surface tension of mixed inorganic and dicarboxylic acid aqueous solutions at 298.15 K and their importance for cloud activation predictions, Phys. Chem. Chem. Phys., 11(36), 8021-8028.

Braban, C. F., and J. P. D. Abbatt (2004), A study of the phase transition behavior of internally mixed ammonium sulfate-malonic acid aerosols, Atmos. Chem. Phys., 4, 1451-1459.

Braban, C. F., M. F. Carroll, S. A. Styler, and J. P. D. Abbatt (2003), Phase transitions of malonic and oxalic acid aerosols, J. Phys. Chem. A, 107(34), 6594-6602.

Braun, C., and U. K. Krieger (2001), Two dimensional angular light scattering in aqueous NaCl single aerosol particles during deliquescence and efflorescence, Opt. Express, 8(6), 314-321.

Buajarern, J., L. Mitchem, and J. P. Reid (2007), Characterizing multiphase Organic/Inorganic/Aqueous aerosol droplets, J. Phys. Chem. A, 111(37), 9054-9061.

Cai, B. Y., J. T. Yang, and T. M. Guo (1996), Interfacial tension of hydrocarbon plus water/brine systems under high pressure, J. Chem. Eng. Data, 41(3), 493-496.

Chan, M. N., A. K. Y. Lee, and C. K. Chan (2006), Responses of ammonium sulfate particles coated with glutaric acid to cyclic changes in relative humidity: Hygroscopicity and Raman characterization, Environ. Sci. Technol., 40(22), 6983-6989.

Chan, M. N., S. M. Kreidenweis, and C. K. Chan (2008), Measurements of the hygroscopic and deliquescence properties of organic compounds of different solubilities in water and their relationship with cloud condensation nuclei activities, Environ. Sci. Technol., 42(10), 3602-3608.

Chang, E. I., and J. F. Pankow (2006), Prediction of activity coefficients in liquid aerosol particles containing organic compounds, dissolved inorganic salts, and water - Part 2: Consideration of phase separation effects by an X-UNIFAC model, Atmos. Environ., 40(33), 6422-6436.

Chen, Q., et al. (2009), Mass spectral characterization of submicron biogenic organic particles in the Amazon Basin, Geophys. Res. Lett., 36, doi:10.1029/2009GL039880.

Chhabra, P. S., N. L. Ng, M. R. Canagaratna, A. L. Corrigan, L. M. Russell, D. R. Worsnop, R. C. Flagan, and J. H. Seinfeld (2011), Elemental composition and oxidation of chamber organic aerosol, Atmos. Chem. Phys., 11(17), 8827-8845.

Chmielewska, A., and A. Bald (2008), Viscosimetric studies of aqueous solutions of dicarboxylic acids, J. Mol. Liq., 137(1-3), 116-121.

Choi, M. Y., and C. K. Chan (2002), The effects of organic species on the hygroscopic behaviors of inorganic aerosols, Environ. Sci. Technol., 36(11), 2422-2428.

Ciobanu, V. G., C. Marcolli, U. K. Krieger, U. Weers, and T. Peter (2009), Liquid-Liquid Phase Separation in Mixed Organic/Inorganic Aerosol Particles, J. Phys. Chem. A, 113(41), 10966-10978.

Ciobanu, V. G., C. Marcolli, U. K. Krieger, A. Zuend, and T. Peter (2010), Efflorescence of Ammonium Sulfate and Coated Ammonium Sulfate Particles: Evidence for Surface Nucleation, J. Phys. Chem. A, 114(35), 9486-9495.

Cohen, M. D., R. C. Flagan, and J. H. Seinfeld (1987), Studies of Concentrated Electrolyte-Solutions Using the Electrodynamic Balance .1. Water Activities for Single-Electrolyte Solutions, J. Phys. Chem.-Us, 91(17), 4563-4574.

Colberg, C. A., U. K. Krieger, and T. Peter (2004), Morphological investigations of single levitated H2SO4/NH3/H2O aerosol particles during deliquescence/efflorescence experiments, J. Phys. Chem. A, *108*(14), 2700-2709.

Compernolle, S., K. Ceulemans, and J. F. Muller (2011), EVAPORATION: a new vapour pressure estimation methodfor organic molecules including non-additivity and intramolecular interactions, Atmos. Chem. Phys., 11(18), 9431-9450.

Cosman, L. M., and A. K. Bertram (2008), Reactive uptake of N2O5 on aqueous H2SO4 solutions coated with 1-component and 2-component monolayers, J. Phys. Chem. A, 112(20), 4625-4635.

Cosman, L. M., D. A. Knopf, and A. K. Bertram (2008), N2O5 reactive uptake on aqueous sulfuric acid solutions coated with branched and

straight-chain insoluble organic surfactants, J. Phys. Chem. A, 112(11), 2386-2396.

Cziczo, D. J., J. B. Nowak, J. H. Hu, and J. P. D. Abbatt (1997), Infrared spectroscopy of model tropospheric aerosols as a function of relative humidity: Observation of deliquescence and crystallization, J. Geophys. Res.-Atmos., 102(D15), 18843-18850.

Decesari, S., et al. (2006), Characterization of the organic composition of aerosols from Rondonia, Brazil, during the LBA-SMOCC 2002 experiment and its representation through model compounds, Atmos. Chem. Phys., 6, 375-402.

Donahue, N. M., S. A. Epstein, S. N. Pandis, and A. L. Robinson (2011), A two-dimensional volatility basis set: 1. organic-aerosol mixing thermodynamics, Atmos. Chem. Phys., 11(7), 3303-3318.

Erdakos, G. B., and J. F. Pankow (2004), Gas/particle partitioning of neutral and ionizing compounds to single- and multi-phase aerosol particles. 2. Phase separation in liquid particulate matter containing both polar and low-polarity organic compounds, Atmos. Environ., 38(7), 1005-1013.

Ervens, B., B. J. Turpin, and R. J. Weber (2011), Secondary organic aerosol formation in cloud droplets and aqueous particles (aqSOA): a review of laboratory, field and model studies, Atmos. Chem. Phys., 11(21), 11069-11102.

Folkers, M., T. F. Mentel, and A. Wahner (2003), Influence of an organic coating on the reactivity of aqueous aerosols probed by the heterogeneous hydrolysis of N2O5, Geophys. Res. Lett., 30(12), doi:10.1029/2003GL017168.

Frank, B. P., and G. Belfort (2001), Atomic force microscopy for low-adhesion surfaces: Thermodynamic criteria, critical surface tension, and intermolecular forces, Langmuir, 17(6), 1905-1912.

Fuzzi, S., S. Decesari, M. C. Facchini, E. Matta, M. Mircea, and E. Tagliavini (2001), A simplified model of the water soluble organic component of atmospheric aerosols, Geophys. Res. Lett., 28(21), 4079-4082.

Fuzzi, S., et al. (2006), Critical assessment of the current state of scientific knowledge, terminology, and research needs concerning the role of organic aerosols in the atmosphere, climate, and global change, Atmos. Chem. Phys., 6, 2017-2038.

Gilardoni, S., S. Liu, S. Takahama, L. M. Russell, J. D. Allan, R. Steinbrecher, J. L. Jimenez, P. F. De Carlo, E. J. Dunlea, and D. Baumgardner (2009), Characterization of organic ambient aerosol during MIRAGE 2006 on three platforms, Atmos. Chem. Phys., 9(15), 5417-5432.

Gill, P. S., T. E. Graedel, and C. J. Weschler (1983), Organic Films on Atmospheric Aerosol-Particles, Fog Droplets, Cloud Droplets, Raindrops, and Snowflakes, Rev. Geophys., 21(4), 903-920.

Giraldo-Zuniga, A. D., J. S. D. Coimbra, D. A. Arquete, L. A. Minim, L. H. M. da Silva, and M. C. Maffia (2006), Interfacial tension and viscosity for poly(ethylene glycol) plus maltodextrin aqueous two-phase systems, J. Chem. Eng. Data, 51(3), 1144-1147.

Goldstein, A. H., and I. E. Galbally (2007), Known and unexplored organic constituents in the earth's atmosphere, Environ. Sci. Technol., 41(5), 1514-1521.

Graber, E. R., and Y. Rudich (2006), Atmospheric HULIS: How humic-like are they? A comprehensive and critical review, Atmos. Chem. Phys., 6, 729-753.

Hallquist, M., D. J. Stewart, S. K. Stephenson, and R. A. Cox (2003), Hydrolysis of N2O5 on sub-micron sulfate aerosols, Phys. Chem. Chem. Phys., 5(16), 3453-3463.

Hallquist, M., et al. (2009), The formation, properties and impact of secondary organic aerosol: current and emerging issues, Atmos. Chem. Phys., 9(14), 5155-5236.

Han, J. H., and S. T. Martin (1999), Heterogeneous nucleation of the efflorescence of (NH(4))(2)SO(4) particles internally mixed with Al(2)O(3), TiO(2), and ZrO(2), J. Geophys. Res.-Atmos., 104(D3), 3543-3553.

Hanel, G. (1976), Single-Scattering Albedo of Atmospheric Aerosol-Particles as a Function of Relative Humidity, J. Atmos. Sci., 33(6), 1120-1124.

Hawkins, L. N., L. M. Russell, D. S. Covert, P. K. Quinn, and T. S. Bates (2010), Carboxylic acids, sulfates, and organosulfates in processed continental organic aerosol over the southeast Pacific Ocean during VOCALS-REx 2008, J. Geophys. Res.-Atmos., 115, doi:10.1029/2009JD013276.

Heald, C. L., D. A. Ridley, S. M. Kreidenweis, and E. E. Drury (2010), Satellite observations cap the atmospheric organic aerosol budget, Geophys. Res. Lett., 37, doi:10.1029/2010gl042737.

Iinuma, Y., O. Boge, T. Gnauk, and H. Herrmann (2004), Aerosol-chamber study of the alpha-pinene/O-3 reaction: influence of particle acidity on aerosol yields and products, Atmos. Environ., 38(5), 761-773.

IPCC (2007), Solomon, S., Qin, D., Manning, M., Chen, Z., Marquis, M., Averyt, K. B., Tignor, M., and Miller, H. L.: Climate Change 2007: The physical science basis. Contribution of working group I to the Fourth Assessment Report of the Intergovernmental Panel on Climate Change, Cambridge University Press, Cambridge, United Kingdom and New York, NY, USA.

Jimenez, J. L., et al. (2009), Evolution of Organic Aerosols in the Atmosphere, Science, 326(5959), 1525-1529.

Kanakidou, M., et al. (2005), Organic aerosol and global climate modelling: a review, Atmos. Chem. Phys., 5, 1053-1123.

Kawamura, K., and K. Ikushima (1993), Seasonal-Changes in the Distribution of Dicarboxylic-Acids in the Urban Atmosphere, Environ. Sci. Technol., 27(10), 2227-2235.

Kiendler-Scharr, A., Q. Zhang, T. Hohaus, E. Kleist, A. Mensah, T. F. Mentel, C. Spindler, R. Uerlings, R. Tillmann, and J. Wildt (2009), Aerosol Mass Spectrometric Features of Biogenic SOA: Observations from a Plant Chamber and in Rural Atmospheric Environments, Environ. Sci. Technol., 43(21), 8166-8172.

Knopf, D. A. (2003), Thermodynamic properties and nucleation processes of upper tropospheric and lower stratospheric aerosol particles, Diss. ETH No. 15103, Zurich, Switzerland.

Knopf, D. A., and M. D. Lopez (2009), Homogeneous ice freezing temperatures and ice nucleation rates of aqueous ammonium sulfate and aqueous levoglucosan particles for relevant atmospheric conditions, Phys. Chem. Chem. Phys., 11(36), 8056-8068.

Knopf, D. A., L. M. Anthony, and A. K. Bertram (2005), Reactive uptake of O-3 by multicomponent and multiphase mixtures containing oleic acid, J. Phys. Chem. A, 109(25), 5579-5589.

Kostorz, G.(2001) Phase Transformations in Materials, Wiley-VCH,Weinheim, Germany, 409–480.

Krieger, U. K., and C. Braun (2001), Light-scattering intensity fluctuations in single aerosol particles during deliquescence, J. Quant. Spectrosc. Ra, 70(4-6), 545-554.

Krieger, U. K., C. A. Colberg, U. Weers, T. Koop, and T. Peter (2000), Supercooling of single H2SO4/H2O aerosols to 158 K: No evidence for the occurrence of the octrahydrate, Geophys. Res. Lett., 27(14), 2097-2100.

Krieger, U. K., C. Marcolli, and J. P. Reid (2012), Exploring the complexity of aerosol particle properties and processes using single particle techniques, Chem. Soc. Rev., 41(19), 6631-6662.

Krieger, U. K., and A. A. Zardini (2008), Using dynamic light scattering to characterize mixed phase single particles levitated in a quasi-electrostatic balance, *Faraday Discuss*, *137*, 377-388.

Kroll, J. H., et al. (2011), Carbon oxidation state as a metric for describing the chemistry of atmospheric organic aerosol, Nat. Chem., 3(2), 133-139.

Kwamena, N. O. A., J. Buajarern, and J. P. Reid (2010), Equilibrium Morphology of Mixed Organic/Inorganic/Aqueous Aerosol Droplets: Investigating the Effect of Relative Humidity and Surfactants, J. Phys. Chem. A, 114(18), 5787-5795.

Laguerie, C., M. Aubry, and J. P. Couderc (1976), Some Physicochemical Data on Monohydrate Citric-Acid Solutions in Water - Solubility, Density, Viscosity, Diffusivity, Ph of Standard Solution, and Refractive-Index, J. Chem. Eng. Data, 21(1), 85-87.

Lang-Yona, N., Y. Rudich, T. F. Mentel, A. Bohne, A. Buchholz, A. Kiendler-Scharr, E. Kleist, C. Spindler, R. Tillmann, and J. Wildt (2010), The chemical and microphysical properties of secondary organic aerosols from Holm Oak emissions, Atmos. Chem. Phys., 10(15), 7253-7265.

Lee, S. H., D. M. Murphy, D. S. Thomson, and A. M. Middlebrook (2002), Chemical components of single particles measured with Particle Analysis by Laser Mass Spectrometry (PALMS) during the Atlanta SuperSite Project: Focus on organic/sulfate, lead, soot, and mineral particles, J. Geophys. Res.-Atmos., 107(D1-D2), doi:10.1029/2000jd000011.

Lee, M., M. Song, K. J. Moon, J. S. Han, G. Lee, and K. R. Kim (2007), Origins and chemical characteristics of fine aerosols during the northeastern Asia regional experiment (atmospheric brown cloud east Asia regional experiment 2005), J. Geophys. Res.-Atmos., 112(D22), doi:10.1029/2006JD008210.

Lewis, E. R. (2006), The effect of surface tension (Kelvin effect) on the equilibrium radius of a hygroscopic aqueous aerosol particle, J. Aerosol. Sci., 37(11), 1605-1617.

Ling, T. Y., and C. K. Chan (2008), Partial crystallization and deliquescence of particles containing ammonium sulfate and dicarboxylic acids, J. Geophys. Res.-Atmos., 113(D14), doi:10.1029/2008JD009779.

Ma, J. C., and D. A. Dougherty (1997), The cation-pi interaction, Chem. Rev., 97(5), 1303-1324.

Marcolli, C., and U. K. Krieger (2006), Phase changes during hygroscopic cycles of mixed organic/inorganic model systems of tropospheric aerosols, J. Phys. Chem. A, 110(5), 1881-1893.

Marcolli, C., B. P. Luo, and T. Peter (2004a), Mixing of the organic aerosol fractions: Liquids as the thermodynamically stable phases, J. Phys. Chem. A, 108(12), 2216-2224.

Marcolli, C., B. P. Luo, T. Peter, and F. G. Wienhold (2004b), Internal mixing of the organic aerosol by gas phase diffusion of semivolatile organic compounds, Atmos. Chem. Phys., 4, 2593-2599.

Martin, S. T. (2000), Phase transitions of aqueous atmospheric particles, Chem. Rev., 100(9), 3403-3453.

Martin, S. T., T. Rosenoern, Q. Chen, and D. R. Collins (2008), Phase changes of ambient particles in the Southern Great Plains of Oklahoma, Geophys. Res. Lett., 35(22), doi:10.1029/2008GL035650.

Martin, S. T., H. M. Hung, R. J. Park, D. J. Jacob, R. J. D. Spurr, K. V. Chance, and M. Chin (2004), Effects of the physical state of tropospheric ammonium-sulfate-nitrate particles on global aerosol direct radiative forcing, Atmos. Chem. Phys., 4, 183-214.

Martin, S. T., et al. (2010), An overview of the Amazonian Aerosol Characterization Experiment 2008 (AMAZE-08), Atmos. Chem. Phys., 10(23), 11415-11438.

Mätzler, C. (2002), MATLAB Functions for Mie Scattering and Absorption.

McNeill, V. F., J. Patterson, G. M. Wolfe, and J. A. Thornton (2006), The effect of varying levels of surfactant on the reactive uptake of N2O5 to aqueous aerosol, Atmos. Chem. Phys., 6, 1635-1644.

Moller, B., J. Rarey, and D. Ramjugernath (2008), Estimation of the vapour pressure of non-electrolyte organic compounds via group contributions and group interactions, J. Mol. Liq., 143(1), 52-63.

Murphy, D. M., D. J. Cziczo, K. D. Froyd, P. K. Hudson, B. M. Matthew, A. M. Middlebrook, R. E. Peltier, A. Sullivan, D. S. Thomson, and R. J. Weber (2006), Single-particle mass spectrometry of tropospheric aerosol particles, J. Geophys. Res.-Atmos., 111(D23), D23S32, doi:10.1029/2006JD007340.

Murray, B. J. (2008), Inhibition of ice crystallisation in highly viscous aqueous organic acid droplets, Atmos. Chem. Phys., 8(17), 5423-5433

Nan, Y. Q., H. L. Liu, and Y. Hu (2006), Composition, microstructure and rheology of aqueous two-phase cationic/anionic surfactant systems, Colloid Surface A, 277(1-3), 230-238.

Nannoolal, Y., J. Rarey, and D. Ramjugernath (2008), Estimation of pure component properties - Part 3. Estimation of the vapor pressure of non-electrolyte organic compounds via group contributions and group interactions, Fluid Phase Equilibr., 269(1-2), 117-133.

Ng, N. L., M. R. Canagaratna, J. L. Jimenez, P. S. Chhabra, J. H. Seinfeld, and D. R. Worsnop (2011), Changes in organic aerosol composition with aging inferred from aerosol mass spectra, Atmos. Chem. Phys., 11(13), 6465-6474.

Ng, N. L., et al. (2010), Organic aerosol components observed in Northern Hemispheric datasets from Aerosol Mass Spectrometry, Atmos. Chem. Phys., 10(10), 4625-4641.

Ngo, D., G. Videen, and P. Chylek (1996), A FORTRAN code for the scattering of EM waves by a sphere with a nonconcentric spherical inclusion, *Comput Phys Commun*, *99*(1), 94-112.

Onasch, T. B., R. L. Siefert, S. D. Brooks, A. J. Prenni, B. Murray, M. A. Wilson, and M. A. Tolbert (1999), Infrared spectroscopic study of the deliquescence and efflorescence of ammonium sulfate aerosol as a function of temperature, J. Geophys. Res.-Atmos., 104(D17), 21317-21326.

Pankow, J. F. (2003), Gas/particle partitioning of neutral and ionizing compounds to single and multi-phase aerosol particles. 1. Unified modeling framework, Atmos. Environ., 37(24), 3323-3333.

Pant, A., M. T. Parsons, and A. K. Bertram (2006), Crystallization of aqueous ammonium sulfate particles internally mixed with soot and kaolinite: Crystallization relative humidities and nucleation rates, J. Phys. Chem. A, 110(28), 8701-8709.

Pant, A., A. Fok, M. T. Parsons, J. Mak, and A. K. Bertram (2004), Deliquescence and crystallization of ammonium sulfate-glutaric acid and sodium chloride-glutaric acid particles, Geophys. Res. Lett., 31(12), doi:10.1029/2004GL020025.

Papon, P., Leblond, J., and Meijer, P. H. E. (1999), The Physics of Phase Transitions: Concepts and Applications, Springer, New York, US.

Parsons, M. T., J. L. Riffell, and A. K. Bertram (2006), Crystallization of aqueous inorganic-malonic acid particles: Nucleation rates, dependence on size, and dependence on the ammonium-to-sulfate, J. Phys. Chem. A, 110(26), 8108-8115.

Parsons, M. T., J. Mak, S. R. Lipetz, and A. K. Bertram (2004), Deliquescence of malonic, succinic, glutaric, and adipic acid

particles, J. Geophys. Res.-Atmos., 109(D6), D06212, doi:10.1029/2003JD004075.

Pena, O., and U. Pal (2009), Scattering of electromagnetic radiation by a multilayered sphere, Comput. Phys. Commun., 180(11), 2348-2354.

Pöhlker, C., et al. (2012), Biogenic Potassium Salt Particles as Seeds for Secondary Organic Aerosol in the Amazon, Science, 337(6098), 1075-1078.

Ramanathan, V., P. J. Crutzen, J. T. Kiehl, and D. Rosenfeld (2001), Atmosphere - Aerosols, climate, and the hydrological cycle, Science, 294(5549), 2119-2124.

Reid, J. P., B. J. Dennis-Smither, N. O. A. Kwamena, R. E. H. Miles, K. L. Hanford, and C. J. Homer (2011), The morphology of aerosol particles consisting of hydrophobic and hydrophilic phases: hydrocarbons, alcohols and fatty acids as the hydrophobic component, Phys. Chem. Chem. Phys., 13(34), 15559-15572.

Riemer, N., H. Vogel, B. Vogel, T. Anttila, A. Kiendler-Scharr, and T. F. Mentel (2009), Relative importance of organic coatings for the heterogeneous hydrolysis of N2O5 during summer in Europe, J. Geophys. Res.-Atmos., 114, D17307, doi:10.1029/2008JD011369.

Robinson, A. L., N. M. Donahue, M. K. Shrivastava, E. A. Weitkamp, A. M. Sage, A. P. Grieshop, T. E. Lane, J. R. Pierce, and S. N. Pandis (2007), Rethinking organic aerosols: Semivolatile emissions and photochemical aging, Science, 315(5816), 1259-1262.

Rogge, W. F., M. A. Mazurek, L. M. Hildemann, G. R. Cass, and B. R. T. Simoneit (1993), Quantification of Urban Organic Aerosols at a Molecular-Level - Identification, Abundance and Seasonal-Variation, Atmos. Environ., 27(8), 1309-1330.

Russell, L. M., S. Takahama, S. Liu, L. N. Hawkins, D. S. Covert, P. K. Quinn, and T. S. Bates (2009), Oxygenated fraction and mass of organic aerosol from direct emission and atmospheric processing measured on the R/V Ronald Brown during TEXAQS/GoMACCS

2006, J. Geophys. Res.-Atmos., 114, D00F05, doi:10.1029/2008JD011275.

Seinfeld, J. H. and Pandis, S. N. (1998), Atmospheric Chemistry and Physics: From Air Pollution to Climate Change, J. Wiley & Sons, New York, USA.

Shelby, J., ed. (1995), Introduction to glass science and technology, The Royal Society of Chemistry, Cambridge, UK.

Shilling, J. E., et al. (2009), Loading-dependent elemental composition of alpha-pinene SOA particles, Atmos. Chem. Phys., 9(3), 771-782.

Shiraiwa, M., M. Ammann, T. Koop, and U. Poschl (2011), Gas uptake and chemical aging of semisolid organic aerosol particles, P. Natl. Acad. Sci. USA, 108(27), 11003-11008.

Shulman, M. L., M. C. Jacobson, R. J. Carlson, R. E. Synovec, and T. E. Young (1996), Dissolution behavior and surface tension effects of organic compounds in nucleating cloud droplets, Geophys. Res. Lett., 23(3), 277-280.

Sjogren, S., M. Gysel, E. Weingartner, U. Baltensperger, M. J. Cubison, H. Coe, A. A. Zardini, C. Marcolli, U. K. Krieger, and T. Peter (2007), Hygroscopic growth and water uptake kinetics of two-phase aerosol particles consisting of ammonium sulfate, adipic and humic acid mixtures, J. Aerosol. Sci., 38(2), 157-171.

Smith, M. L., M. Kuwata, and S. T. Martin (2011), Secondary Organic Material Produced by the Dark Ozonolysis of alpha-Pinene Minimally Affects the Deliquescence and Efflorescence of Ammonium Sulfate, Aerosol. Sci. Tech., 45(2), 244-261.

Smith, M. L., A. K. Bertram, and S. T. Martin (2012), Deliquescence, efflorescence, and phase miscibility of mixed particles of ammonium sulfate and isoprene-derived secondary organic material, Atmos. Chem. Phys., 12(20), 9613-9628.

Song, M., C. Marcolli, U. K. Krieger, A. Zuend, and T. Peter (2012a), Liquid-liquid phase separation and morphology of internally mixed

dicarboxylic acids/ammonium sulfate/water particles, Atmos. Chem. Phys., 12(5), 2691-2712.

Song, M., C. Marcolli, U. K. Krieger, A. Zuend, and T. Peter (2012b), Liquid-liquid phase separation in aerosol particles: Dependence on O:C, organic functionalities, and compositional complexity, Geophys. Res. Lett., 39, L19801, doi:10.1029/2012GL052807.

Song, M., M. Lee, J. H. Kim, S. S. Yum, G. Lee, and K. R. Kim (2010), New particle formation and growth in relation to vertical mixing and chemical species during ABC-EAREX2005, Atmos. Res., 97(3), 359-370.

Spyropoulos, F., P. Ding, W. J. Frith, I. T. Norton, B. Wolf, and A. W. Pacek (2008), Interfacial tension in aqueous biopolymer-surfactant mixtures, J. Colloid. Interf. Sci., 317(2), 604-610.

Swietlicki, E., et al. (2008), Hygroscopic properties of submicrometer atmospheric aerosol particles measured with H-TDMA instruments in various environments - a review, Tellus B, 60(3), 432-469.

Takahama, S., R. E. Schwartz, L. M. Russell, A. M. Macdonald, S. Sharma, and W. R. Leaitch (2011), Organic functional groups in aerosol particles from burning and non-burning forest emissions at a high-elevation mountain site, Atmos. Chem. Phys., 11(13), 6367-6386.

Tang, I. N., and H. R. Munkelwitz (1984), An Investigation of Solute Nucleation in Levitated Solution Droplets, J. Colloid. Interf. Sci., 98(2), 430-438.

Tang, I. N., and H. R. Munkelwitz (1993), Composition and Temperature-Dependence of the Deliquescence Properties of Hygroscopic Aerosols, Atmos. Environ., 27(4), 467-473.

Tang, I. N., and H. R. Munkelwitz (1994), Water Activities, Densities, and Refractive-Indexes of Aqueous Sulfates and Sodium-Nitrate Droplets of Atmospheric Importance, J. Geophys. Res.-Atmos., 99(D9), 18801-18808.

Te, Y-F. (2011), Mie resonance spectroscopy of single levitated particle, Diss. University of Zurich, Zurich, Switzerland.

Tervahattu, H., J. Juhanoja, V. Vaida, A. F. Tuck, J. V. Niemi, K. Kupiainen, M. Kulmala, and H. Vehkamaki (2005), Fatty acids on continental sulfate aerosol particles, J. Geophys. Res.-Atmos., 110(D6), D06207, doi:10.1029/2004JD005400.

Thornton, J. A., and J. P. D. Abbatt (2005), N2O5 reaction on submicron sea salt aerosol: Kinetics, products, and the effect of surface active organics, J. Phys. Chem. A, 109(44), 10004-10012.

Topping, D. O., G. B. McFiggans, G. Kiss, Z. Varga, M. C. Facchini, S. Decesari, and M. Mircea (2007), Surface tensions of multi-component mixed inorganic/organic aqueous systems of atmospheric significance: measurements, model predictions and importance for cloud activation predictions, Atmos. Chem. Phys., 7(9), 2371-2398.

Torza, S., and S. G. Mason (1970), 3-Phase Interactions in Shear and Electrical Fields, J. Colloid Interf. Sci., 33(1), 67-83.

Varga, Z., G. Kiss, and H. C. Hansson (2007), Modelling the cloud condensation nucleus activity of organic acids on the basis of surface tension and osmolality measurements, Atmos. Chem. Phys., 7(17), 4601-4611.

Virtanen, A., et al. (2010), An amorphous solid state of biogenic secondary organic aerosol particles, Nature, 467(7317), 824-827.

Weingartner, E., M. Gysel, and U. Baltensperger (2002), Hygroscopicity of aerosol particles at low temperatures. 1. New low-temperature H-TDMA instrument: Setup and first applications, Environ. Sci. Technol., 36(1), 55-62.

Winston, P. W., and D. H. Bates (1960), Saturated Solutions for the Control of Humidity in Biological-Research, Ecology, 41(1), 232-237.

Wu, Y. T., Z. Q. Zhu, and L. H. Mei (1996), Interfacial tension of poly(ethylene glycol) plus salt plus water systems, J. Chem. Eng. Data, 41(5), 1032-1035.

Xu, J., D. Imre, R. McGraw, and I. Tang (1998), Ammonium sulfate: Equilibrium and metastability phase diagrams from 40 to -50 degrees C, J. Phys. Chem. B, 102(38), 7462-7469.

Yeung, M. C., A. K. Y. Lee, and C. K. Chan (2009), Phase Transition and Hygroscopic Properties of Internally Mixed Ammonium Sulfate and Adipic Acid (AS-AA) Particles by Optical Microscopic Imaging and Raman Spectroscopy, Aerosol. Sci. Tech., 43(5), 387-399.

You, Y., et al. (2012), Images reveal that atmospheric particles can undergo liquid-liquid phase separations, P. Natl. Acad. Sci. USA, 109(33), 13188-13193.

Yu, H., et al. (2006), A review of measurement-based assessments of the aerosol direct radiative effect and forcing, Atmos. Chem. Phys., 6, 613-666.

Zardini, A. A., S. Sjogren, C. Marcolli, U. K. Krieger, M. Gysel, E. Weingartner, U. Baltensperger, and T. Peter (2008), A combined particle trap/HTDMA hygroscopicity study of mixed inorganic/organic aerosol particles, Atmos. Chem. Phys., 8(18), 5589-5601.

Zhang, Y. H., and C. K. Chan (2002), Understanding the hygroscopic properties of supersaturated droplets of metal and ammonium sulfate solutions using Raman spectroscopy, J. Phys. Chem. A, 106(2), 285-292.

Zhang, Q., et al. (2007), Ubiquity and dominance of oxygenated species in organic aerosols in anthropogenically-influenced Northern Hemisphere midlatitudes, Geophys. Res. Lett., 34(13), L13801, doi:10.1029/2007GL029979.

Zobrist, B., C. Marcolli, D. A. Pedernera, and T. Koop (2008), Do atmospheric aerosols form glasses?, Atmos. Chem. Phys., 8(17), 5221-5244.

Zuend, A., and J. H. Seinfeld (2012), Modeling the gas-particle partitioning of secondary organic aerosol: the importance of liquid-liquid phase separation, Atmos. Chem. Phys., 12(9), 3857-3882.

Zuend, A., C. Marcolli, B. P. Luo, and T. Peter (2008), A thermodynamic model of mixed organic-inorganic aerosols to predict activity coefficients, Atmos. Chem. Phys., 8(16), 4559-4593.

Zuend, A., C. Marcolli, T. Peter, and J. H. Seinfeld (2010), Computation of liquid-liquid equilibria and phase stabilities: implications for RH-dependent gas/particle partitioning of organic-inorganic aerosols, Atmos. Chem. Phys., 10(16), 7795-7820.

Zuend, A., C. Marcolli, A. M. Booth, D. M. Lienhard, V. Soonsin, U. K. Krieger, D. O. Topping, G. McFiggans, T. Peter, and J. H. Seinfeld (2011), New and extended parameterization of the thermodynamic model AIOMFAC: calculation of activity coefficients for organic-inorganic mixtures containing carboxyl, hydroxyl, carbonyl, ether, ester, alkenyl, alkyl, and aromatic functional groups, Atmos. Chem. Phys., 11(17), 9155-9206.

Acknowledgements

My PhD project during last three years and five months would not have been possible without the support and help of many colleagues and friends. Therefore, I appreciate deeply all people who participated directly and indirectly for the success of my thesis.

Dear.

Prof. Thomas Peter. Thank you very much for offering me the opportunity to join the Atmospheric Chemistry group at ETH. I greatly respect your scientific desire regarding the specific discussion and suggestion. Based on your essential questions and advices, I have learned a lot and enhanced my atmospheric knowledge during my work. You are a role model of me.

Dr. Claudia Marcolli. I have been really well supervised by my supervisor Claudia during last 3.5 years. From your excellent support, discussion, and suggestion for my PhD work, my background of atmospheric chemistry has been improved. In addition, I would like to thank you deeply for the careful proof-reading and fast feedback for the articles. The most important thing that I thank you is that you gave me a lot of encouragements when my work was not going well.

Dr. Uli Krieger. Thank you very much for the experimental support with EDB measurements and also the microscope. Moreover, thank you for the suggestion and help for my further career. I will miss your nice smile and your kind.

Dr. Thomas Mentel. I very much appreciate your efforts of being my co-examiner of my PhD thesis and also for your great interest in my work and for coming to Zurich to the PhD defence.

Uwe Weers and Edwin Hausammann. Thank you for the technical support in the laboratory. I was happy to work with you and your fun.

My office mates. Dr. Andre Welti and Dr. Ana Cirisan. Thank you for the good working atmosphere in our office for last 3 years. I will miss you guys and your joke as well. Also, special thanks to my colleagues including Gouri, Valeria, Florian, Johannes, Erika, Andy, Lukas, Dani, Jianxiong, Gabriela, Andi, and Funk for fun, lunch and coffee break.

My friends in Korea. 김채인, 송은영, 심선희, 최진희, 김인애, 홍영림, 이고은, 이정해, 황민정, 최재우, 권규상, 임세희, 김자한, 오동현, 김종환, KYPAS 식구들의 사랑과 관심 진심으로 감사드립니다.

My family. My parents, my brother and 복실이. Because of your big support and warm consideration, I could finish my PhD successfully in Switzerland. Thank you very much.

이재봉. Thank you so much for taking care of me and sharing precious time with me. Your supporting gave me full of encouragement and kept me confident. I wish your success for your PhD research as well.